Orientational Fluctuations of Liquid Water at Hydrophobic and Hydrophilic Interfaces

by

Sucheol Shin

B.S., University of California, Berkeley (2011)

Submitted to the Department of Chemistry
in Partial Fulfillment of the Requirements for the Degree of

DOCTOR OF PHILOSOPHY IN PHYSICAL CHEMISTRY

at the

MASSACHUSETTS INSTITUTE OF TECHNOLOGY

June 2018

Signature of Author: ____
Department of Chemistry
May 18, 2018

Certified by: ____
Adam P. Willard
Assistant Professor of Chemistry
Thesis Supervisor

Accepted by: ____
Robert W. Field
Haslam and Dewey Professor of Chemistry
Chairman, Departmental Committee on Graduate Students

This doctoral thesis has been examined by a Committee of the Department of Chemistry as follows:

Professor Jianshu Cao ____
Chairman, Thesis Committee
Professor of Chemistry

Professor Adam P. Willard ____
Thesis Supervisor
Assistant Professor of Chemistry

Professor Robert W. Field ____
Member, Thesis Committee
Haslam and Dewey Professor of Chemistry

Orientational Fluctuations of Liquid Water at Hydrophobic and Hydrophilic Interfaces

by

Sucheol Shin

Submitted to the Department of Chemistry
on May 18, 2018, in Partial Fulfillmen of the
Requirements for the Degree of
Doctor of Philosophy in Physical Chemistry

ABSTRACT

Being ubiquitous in nature, liquid water interfaces host many important physical and chemical processes. Most of these processes are affected by the properties of water interfaces which depend on molecular details of the interfacial environments. It is thus fundamental to understand microscopic features of a water interface for studying the interfacial phenomena. In this work, we explore structural characteristics of various water interfaces using the methods of molecular simulations and statistical mechanics. Specifically, we describe the intrinsic molecular structure of a water interface in terms of the anisotropic, depth-dependent distribution of water's molecular orientation. We also analyze the collective hydrogen bond network at the interface which determines the orientational fluctuations of interfacial water molecules.

This dissertation consists of three separate studies on related but distinct subtopics. First, we focus on the molecular structure and dielectric properties of the liquid water–vapor interface. We present a statistical mechanical model of interfacial hydrogen bonding which is capable of predicting the orientational distribution at the interface. Using this model along with the atomistic simulations, we reveal that the hydrogen bonding interactions of non-ideal geometries are responsible for the characteristics of the interfacial dielectric properties.

Then, we introduce a general computational framework that can characterize the interfacial properties of a hydrated solute from its atomistic simulation. This method utilizes the orientational structure of interfacial water molecules which reflects the microscopic informations about the solute's surface. We demonstrate that our method is applicable with both temporal and spatial resolutions to a chemically heterogenous surface as well as an irregular surface. Therefore, it is useful especially for probing the local hydration dynamics of a protein which is correlated with the conformational fluctuations.

Finally, we study the effects of surface–water interactions on water's interfacial hydrogen bonding structure using a disordered model hydrophilic surface with tunable polarity. We investigate the relationship between the surface polarity and interfacial molecular structure using the characterization method previously introduced. Based on a mean-field model of interfacial hydrogen bonding, we also quantify the energetic component of surface–water interactions that specifically contribute to modifying the interfacial hydrogen bond network. We identify this specific energetic component as a new measure for hydrophilicity.

Thesis Supervisor: Adam P. Willard
Title: Assistant Professor of Chemistry

Acknowledgments

Since September in 2013, I have owed a huge amount of beneficial interactions to many people for my graduate work and life. Thanks to their advice, support, favor, humor, friendship, and love, I could have gone through so far and finally got an honorable opportunity of expressing my gratitudes to them.

First and foremost, I am very grateful to my advisor, Adam Willard, for his guidance and support throughout my graduate career. He always provided insightful advice from which I learned the A to Z of performing a scientific research within a keen perspective. I especially much appreciate his patience, encouragement, and trust on me such that I could have successfully grown up as the first doctoral graduate from his group. I believe that his enthusiasm for science will keep inspiring me throughout my career afterwards.

I would like to thank my thesis committee, Jianshu Cao and Bob Field, for their helpful advice on this work. I thank my undergraduate research advisor, Phill Geissler, for his continuing support on my career. In addition to him, there are several people to whom I asked advice for shaping the direction of my career. For that, I specifically thank David Limmer, Todd Gingrich, Troy Van Voorhis, Bin Zhang, Rick Remsing, and Glen Hocky. I am also grateful to David Chandler for his insightful comments on the early stage of the work described in Chapter 3. It took me so many years to fully appreciate his insight that I could not share the final result with him in time, but I wish he would be still happy about what I achieved.

I am greatly indebted to my colleagues for their intellectual and social resources. Of course, the most appreciated are the Willard group people: Liang Shi, Chee Kong Lee, Liza MY Lee, Paul Teichen, Eric Alt, John Kattirtzi, Thomas Avila, Kaitlyn Dwelle, Amro Dodin, Kyaw Hpone Myint, Yizhi Shen, and Songela Chen. I thank them for all the advice, support, favor, and friendship they have provided me with. I also would like to acknowledge other theory group people who include Tianyu Zhu, Alex Kohn, Evan Piephoff, Mike Mavros, Matt Welborn, Chern Chuang, Takashi Tsuchimochi, Nadav Geva, Nathan Ricke, Helena Qi, James Shepherd, Piotr de Silva, Chang-Yu Hsieh, Valerie Vaissier, Hong-Zhou Ye, Lexie McIsaac, Zhou Lin, Tamar Goldzak, Wenjun Xie, Yifeng Qi, Tom Parsons, and Diptarka Hait. All of them are so brilliant and wonderful that it has been my big pleasure to share the workspace (so-called the "zoo") with them during my graduate study. I hope that they enjoyed interacting with me as much as I did.

I would like to thank my friends in the cohort of physical chemistry: Daniel Franke, Jessica Carr, Tim Barnum, Salima Bahri, and Percival Yang-Ting Chen. They have always been friendly and cheering whenever I came across them, and I regret that I could not have more time with them outside the work. In addition to them, I acknowledge other physical chemists including Trevor Erickson, Katie Shulenberger, Sophie Bertram, Wei Jia Chen, He Wei, and Yue Chen. I also appreciate the support and advice from Korean chemists who include Yoseob Yoon, Hyun Doug Shin, Grace Han, Youngmin Yoon, Gyunghoon Kang, Sarah Sunah Park, Hyangsoo Jeong, Minjung Son, Jason Jungwan Yoo, Seokjoon Oh, Rebecca Soyoung Kim, Hyowon Seo, Byungsu Kwon, Myungwoon Lee, Hye Won Moon, and Jaeyune Ryu.

I thank Peter Giunta and Li Miao for their assistance with many complicated administrative procedures. I also appreciate lots of support and resources provided by the Chemistry Education Office featuring Jennifer Weisman, Rebecca Teixeira, Jay Matthews, Karen Shaner, Abby Greff, Lynn Marie Guthrie-Libby, and Jared Embelton.

Outside the work, there are a number of peers and friends who have supported me through the same cultural background. I thank Donggyu Kim, Sang-won Leigh, Seongjun Park, Hoyoung Park, and Chang Sub Kim, especially for sharing the days of our graduate studies together since we arrived at MIT back in the fall, 2013. I appreciate the special friendship offered by the "Korean-born-in-1988" group including Alan Gye Hyun Kim, Donghun Kim, Doyoon Kim, Dongkwan Kim, Minjae Kim, Jaehwan Kim, Joohyun Seo, Hyung Won Chung, Han Kyul Joo, Kyel Ok, Sangjoon Lee, Sung Kwan Lee, Anna Lee, Ingon Lee, Junghyun Lee, Jongwoo Lee, Hyunkwang Lee, So Yeon Lim, Kyungyong Choi, and Siwon Choi. I enjoyed much the time when I served as the president of Korean Graduation Students Association and I would like to express my sincere gratitude to many people who supported me for doing that, especially those who worked together as the executive board members, including Moo Sun Hong, Joonwon Choi, Hyodong Lee, Yoon Ah Shin, Frederick Sangyeon Cho, Andrew Hyungsuk Song, Dogyoon Song, Young-Gyu Yoon, and Dong-Gwang Ha.

I also appreciate the long-time support from the old friends who I got to know even before I started the graduate study. Specifically, those people feature Donghyun Seo, Do Yeon Yoon, Kwonsang Lee, and Jeonyoon Lee, who are from the same class of my high school, and Seul Ki Ahn, Min Suk Kim, Shi Hang Lee, and Seawoong Lee, who are from my college and now become the best friends of my life. I also thank Chang Ho Sohn, Hong Seok Yun, Jungwoo Kim, Chung Whan Lee, Changmin Lee, Hyungmok Son, Jun Young Jung, Hyerim Chun, Sungbin Sohn, WooChan Jeong, YongJune Uhm, and many others, for their thoughtful advice and hospitality.

I should not forget the financial support from the Kwanjeong Educational Foundation which has continued since my undergraduate study. I thank the founder, Kwanjeong Lee Chong-Hwan, as well as all the administrators.

Lastly, I am greatly thankful to my family for their unconditional love and support. Without them, none of this work would have been feasible, so I would like to attribute most of my accomplishments to my parents and brother, Uicheol.

To my parents

Contents

List of Figures

Chapter 1

Introduction

Water is the most ubiquitous liquid in nature. Not only does it fill the oceans and sky, but it also constitutes and sustains every living organism. Due to its ubiquity and significance to life, water has been a popular topic to scientists and philosophers for ages [1]. Especially over the recent decades, tremendous effort has been made to understand the role of water in many important phenomena that involve chemical species or biomolecules [2–13]. The development of molecular simulations and high-performance computing resources enabled the investigation of water molecules in a variety of conditions. In this work, we investigate the fluctuations in molecular orientations at water interfaces based on the methods of atomistic simulations and statistical mechanics. This chapter provides basic informations about the hydrogen bonds in liquid water, which are fundamental to the correlations in molecular orientations at a water interface and the interfacial molecular structure.

1.1 Hydrogen Bonds in Liquid Water

The water molecule (H_2O) consists of two hydrogen and one oxygen atoms.[1] It has a bent structure with the oxygen at its center as illustrated in Fig. 1.1(a). For an isolated water molecule, the angle formed between two OH bonds and the bond length are 104.5° and 1.0 Å at equilibrium, respectively [14]. Although the oxygen and hydrogen atoms are covalently bonded, the OH bond is electronically polarized toward the oxygen because of its large electronegativity relative to that of a hydrogen. The valence electrons are thus delocalized mostly around the oxygen atom, which makes the molecular shape of an isolated water roughly spherical. The virtual boundary of those electrons in molecular orbitals determines the molecular diameter,[2] which is about 2.8 Å [15].

The electronic polarization in the OH bond gives rise to the partial charges, which are negative on the oxygen and positive on the hydrogens. As a result, a water

---

[1] Henry Cavendish discovered water's composition for the first time in 1780s and Antoine Lavoisier confirmed it in a separate way [1].

[2] It is also called the van der Waals diameter within which distinct molecules cannot share the same space by Pauli's principle.

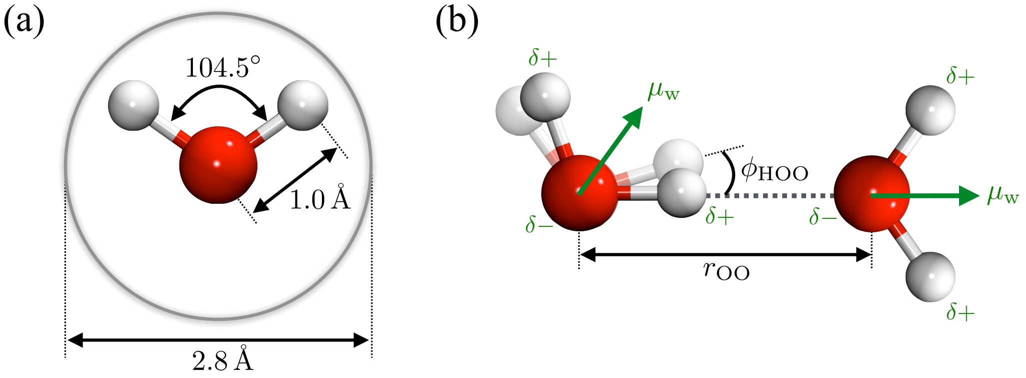

Figure 1.1 (a) Geometry of an isolated water molecule, where the oxygen and hydrogen atoms are colored in red and white, respectively, and the virtual boundary of its delocalized valance electrons is shown with the gray circle. (b) A pair of water molecules with a hydrogen bond between them, where the partial charges on atoms and the resulting dipole moments are shown in green. A possible fluctuation in the hydrogen bonding configuration is indicated by the transparent shade.

molecule has a large dipole moment[3] and thus interacts with another water molecule electrostatically. As illustrated in Fig. 1.1(b), a pair of water molecules favors a configuration in the particular geometry in which a hydrogen of one molecule is oriented toward the oxygen of the other. By doing so, the water molecule virtually forms a dimer with a strong electrostatic attraction between the partial charges of different parities. This type of favorable dipole-dipole interaction, which involves a largely polarized hydrogen, frequently arises in other chemical systems and is called a *hydrogen bond*, or *H-bond* (although it is much weaker than a covalent bond). A hydrogen bonded system involves some chemical moiety donating its polarized hydrogen to another moiety, so the water molecules on the left and right in Fig 1.1(b) are referred to as the hydrogen donor and acceptor, respectively.

Water molecules exist in a condensed phase in naturally accessible conditions owing to their strong intermolecular attractive forces. The hydrogen bond energy of a water dimer is about 20 kJ/mol ($\sim 8k_BT$ at room temperature) [17], which is much larger than the intermolecular interaction of a small nonpolar molecule (*e.g.*, ~ 6 kJ/mol for nitrogen [18]). Here the range of hydrogen bond energy is derived from the fluctuation in the hydrogen bonding configuration. As indicated in Fig. 1.1(b), the distance between the oxygen atoms, r_{OO}, and the deviation angle of the OH vector from the linear bonding direction, ϕ_{HOO}, affect the hydrogen bond energy.[4] For a solid phase of water, every molecule is hydrogen bonded with $r_{\mathrm{OO}} = 2.75$ Å and $\phi_{\mathrm{HOO}} \simeq 0°$ in its crystalline lattice to maximize the overall hydrogen bond energy. Because of the sp^3 hybridzation on oxygen atoms, the water molecules are aligned

---

[3] The dipole moment of an isolated water molecule is measured as about 1.85 D from the microwave spectroscopy on a dilute vapor [16]. In liquid phase, a water molecule is further polarized by the surrounding such that its average dipole moment is 2.95 D[14].

[4] The relative orientation between the pair also matters but a hydrogen bonded pair is usually optimized in its relative orientation to have lower energy like the one in Fig. 1.1(b). Note that it is not yet the minimum energy configuration which requires the HOH planes to be in different planes.

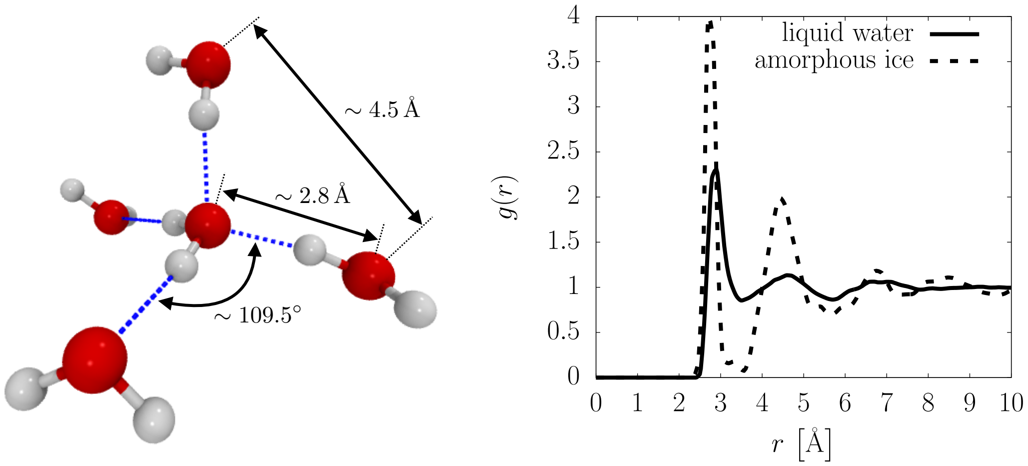

Figure 1.2 (left) Water molecules that have a hydrogen bonding structure of tetrahedral geometry. (right) Radial distribution functions of liquid water at 298 K and amorphous ice at 77 K, which are shown in solid and dashed lines respectively. The data are adapted from the X-ray diffraction experiments reported in Refs. 19 and 20.

within a tetrahedral geometry such that a homogeneous ice crystal features the tetrahedral hydrogen bond network repeating throughout the phase. Above the melting temperature, thermal fluctuations are large enough to relax the crystalline structure and rearrange the water molecules into the disordered liquid phase. Nevertheless, liquid water shares structural characteristics with ice. As illustrated in Fig. 1.2, the radial distribution function of liquid water exhibits qualitatively the same oscillation as that of amorphous ice except its amplitude and width.[5] The area under the curve up to the first minimum also indicates four neighbors around a molecule, which implies the coordination of tetrahedral geometry on average.[6]

The intermolecular structure of liquid water is much more complicated than that of simple liquids, because of the directional nature of hydrogen bonding as well as the subtle balance between energy and entropy [21]. While the water molecules tend to have a tetrahedral bonding structure like ice, each molecule keeps changing its hydrogen bond partners by reorienting itself. The bulk structure of liquid water is thus characterized by a disordered hydrogen bond network percolating throughout the phase. Further microscopic details on the anisotropic hydrogen bonding structure can be revealed by molecular simulations. For instance, we can assess the local tetrahedrality based on the order parameter that was first introduced by Errington

---

[5] The radial distribution function, or pair correlation function, is defined as

$$g(r) = \frac{V}{\rho}\left\langle \sum_{i>1} \delta(\mathbf{r}_1)\delta(\mathbf{r}_i - \mathbf{r}) \right\rangle$$

where V is the volume of the system, ρ is the number density, $\mathbf{r}_i$ is the position of the ith particle, $\delta(\mathbf{x})$ is the Dirac delta function, and $\langle \cdots \rangle$ denotes an equilibrium average. Both liquid water and amorphous ice are isotropic such that the above function depends only on the pair distance, $|\mathbf{r}| = r$ (here we consider the oxygen-oxygen pairs).

[6] The average number of particles within distance r is computed as $n(r) = 4\pi\rho \int_0^r g(r')r'^2 dr'$.

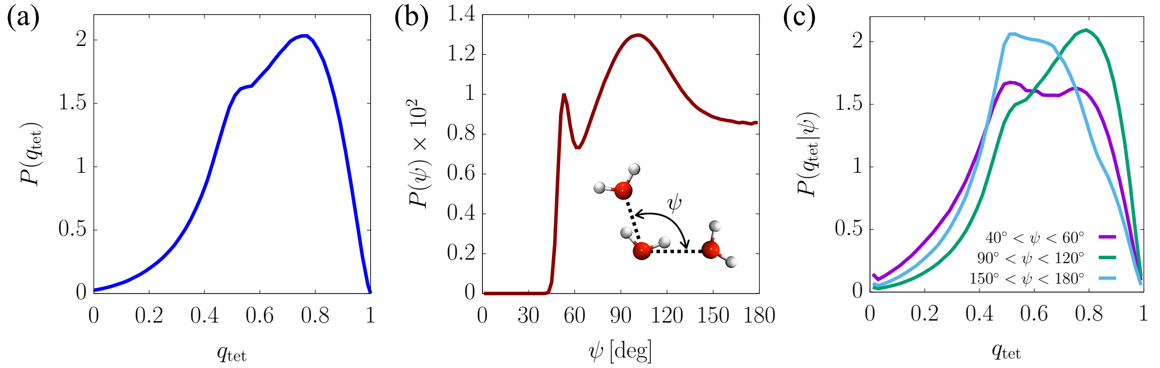

Figure 1.3 (a) Probability distribution of the tetrahedral order parameter. (b) Probability distribution of the angle between the lines joining the central molecule of a water triplet and its neighbors. A schematic depiction of the angle is given at the corner. (c) Conditional probability distribution that a specific value of q_{tet} is obtained from a water trimer within a given range of ψ. These plots are based on a molecular dynamics simulation of the TIP4P water at 298 K [24].

and Debenedetti [22]. For each individual molecule, it is computed as

$$q_{\mathrm{tet}} = 1 - \frac{3}{8} \sum_{j=1}^{3} \sum_{k=j+1}^{4} \left(\cos \psi_{jk} + \frac{1}{3} \right)^2 \tag{1.1}$$

where ψ_{jk} is the angle between the lines joining the oxygen of the probe molecule and those of its nearest neighbors j and k (see the schematic illustration in Fig. 1.3(b)). By definition, $q_{\mathrm{tet}} = 1$ for perfectly tetrahedral bonding[7] as in an ice crystal whereas $\langle q_{\mathrm{tet}} \rangle = 0$ for an ideal isotropic fluid[8], where the angle brackets represent an equilibrium average. As illustrated in Fig. 1.3(a), it is broadly distributed between 0 and 1 for liquid water, with the prominent peak around $q_{\mathrm{tet}} = 0.75$ and the shoulder around $q_{\mathrm{tet}} = 0.5$. For a complemental view on $P(q_{\mathrm{tet}})$, we can also look into the statistics of ψ, the angle from Eq. (1.1). As illustrated in Fig. 1.3(b), the probability distribution indicates that while the majority of water trimers are tetrahedral as defined by ψ, there is a significant portion of those which are beyond the ideal range. The analysis with the conditional probability, $P(q_{\mathrm{tet}}|\psi)$, as shown in Fig. 1.3(c), suggests that the former and latter groups of trimers mostly contribute to the peak and shoulder of $P(q_{\mathrm{tet}})$, respectively. Note that there is another important subpopulation of trimers with $\psi \lesssim 60°$ in Fig. 1.3(b), most of which is in an intermediate state of water's reorientation [23].

---

[7] The tetrahedral angle is defined as $\theta_{\mathrm{T}} \equiv \cos^{-1}(1/3) \approx 109.47°$ from the geometry of a tetrahedron.

[8] If the mutual arrangements among the molecules are random such that $P(\cos\psi)$ is uniform, then $\langle q_{\mathrm{tet}} \rangle = 1 - (3/8) \times 6 \int_0^{\pi} d(\cos\psi)\, (\cos\psi + 1/3)^2 = 0$.

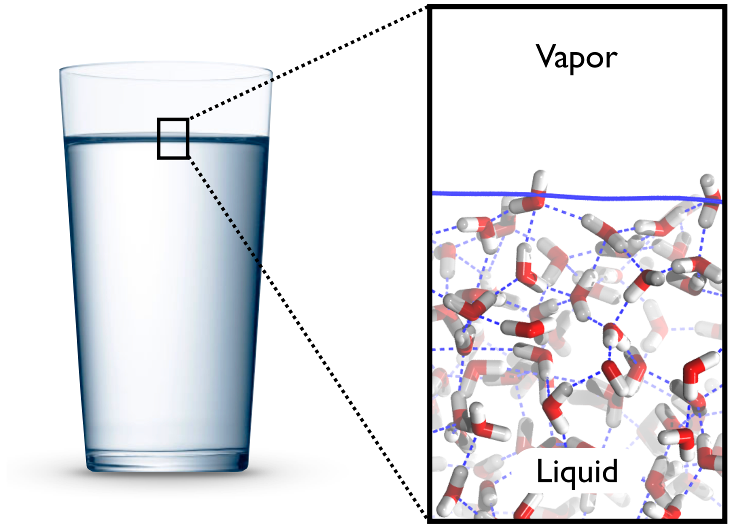

Figure 1.4 Illustration of a molecular-level view into the top surface of a cup of water, based on a snapshot from a simulation of the liquid water-vapor interface. Here the hydrogen bonds and liquid-vapor interface are shown in the blue dashed and solid lines, respectively.

1.2 Liquid Water Interface

Water interfaces are ubiquitous in nature as much as liquid water. While being in different forms and conditions, they host a variety of physicochemical processes. In the atmosphere, for example, the chemical reactions that affect air quality and climate occur at the aqueous liquid–vapor interfaces of cloud droplets and aerosols [13, 25, 26]. In a biological system, water plays a significant role in mediating the interactions between biomolecules at their interfaces and thus facilitating their folding and aggregation [7, 8]. Therefore, understanding the microscopic nature of water molecules at interfaces is fundamental to studying these phenomena.

A water interface has different physical properties than that of the bulk liquid [13, 27, 28]. By definition, there are less water molecules in the vicinity of the liquid phase boundary. This implies that the water density at the interface is anisotropic whereas the density in the bulk liquid is uniform on average. Hence, the hydrogen bonding environment at the interface differs significantly from that in the bulk. At the liquid water–vapor interface, for instance, the three-dimensional hydrogen bond network is subject to the termination along the phase boundary as illustrated in Fig. 1.4. Since many anomalous behaviors of liquid water[9] are rooted in the characteristics of hydrogen bonds [29], the disruption of the hydrogen bond network at the interface gives rise to the unique properties that are important in mediating a given interfacial phenomenon.

Given the interfacial perturbation, a water molecule at the interface prefers a particular orientation that is capable of more favorable hydrogen bonding interactions. As illustrated in Fig. 1.4, the water molecules at the very top of liquid surface tend

---

[9] A representative example of water's anomaly is that the density of liquid water is larger than that of ice whereas solid phase is more dense than liquid for most substance.

to orient one of their OH bonds to the vapor phase. With a free OH bond, they can form up to three hydrogen bonds into the liquid phase, which is the maximum number available in the given geometric constraint. Since the orientation of a water molecule is correlated through hydrogen bonds with those of nearby molecules [30–32], the orientational preference at the top layer influences the molecular orientations in the subsequent layers. Therefore, the distribution of the molecular orientation at a water interface is anisotropic and depth-dependent.

The *orientational distribution* well characterizes the molecular structure of a water interface, as it represents the spatially heterogeneous hydrogen bonding structure. However, the structural quantities introduced in the previous section are not effective in characterizing the interface; the radial distribution function does not change significantly from that in the bulk [33] and the tetrahedral order parameter is ill-defined because there are no four neighbors adjacent to a given molecule at the interface. Thus, the orientational distribution is a quantity of main concern throughout this work. We describe it in more detail along with other interfacial quantities in the following chapter.

Chapter 2

Molecular Structure of Water Interfaces

In this chapter, we describe the molecular structure of water interfaces as a preliminary to the focused studies in Chapters 3–5. We first introduce the intrinsic water interface that is adopted throughout this work as a standard frame of reference for analyzing the molecular details of a water interface. Then we characterize the molecular structure of the liquid water–vapor interface in terms of the density profile, orientational distribution, and dielectric properties. We speculate about how the interfacial molecular structure and dielectric properties are related with the interfacial hydrogen bonding. Finally, we compare hydrophilic and hydrophobic interfaces based on the surface–water interactions and interfacial molecular structure.

2.1 The Intrinsic Water Interface

A liquid water interface is dynamic at molecular level. Due to the thermal motions of interfacial molecules, the liquid phase boundary evolves over time and features a rough, irregular surface as illustrated in Fig. 2.1. The spatial fluctuations in the liquid phase boundary contribute to the interfacial properties, but they also serve to blur out the molecular details of the interface. These details contain the useful information about the structural response of interfacial molecules to the anisotropic environment imposed by the phase boundary. In this work, we will focus on the *intrinsic structure of a water interface* which is independent of its complex undulation. Specifically, we first identify the time-varying position of the liquid phase boundary, so-called the *intrinsic interface*, and then describe the interfacial structure in terms of the coordinates of individual water molecules relative to the interface (see Fig. 2.1). The construction of the intrinsic water interface is based on the procedure described in Ref. 34, and here we provide its detail as below.

To locate the instantaneous liquid phase boundary, we compute the coarse-grained density field at given position $\mathbf{r}$ and time t,

$$\bar{\rho}(\mathbf{r}, t) = \sum_i \phi(|\mathbf{r} - \mathbf{r}_i(t)|; \xi) \tag{2.1}$$

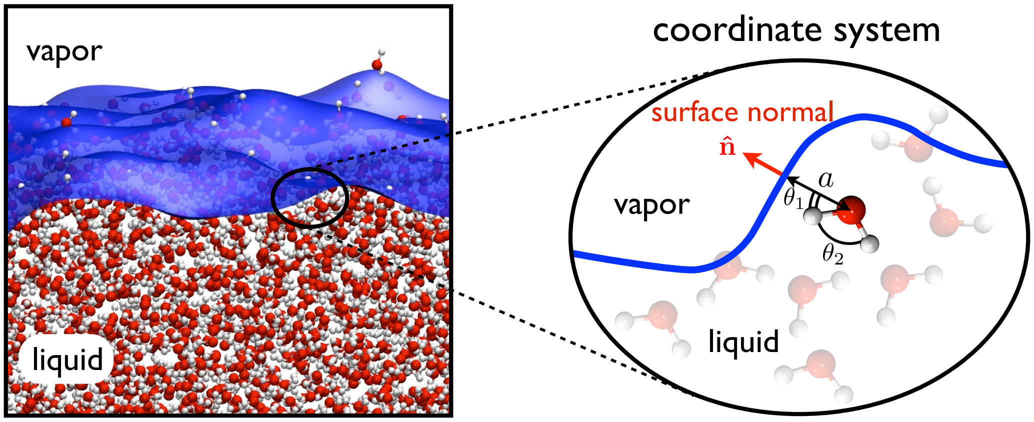

Figure 2.1 (left) Snapshot from a simulation of the water liquid–vapor interface, where the instantaneous interface is shown in blue surface. (right) Schematic illustration of the molecular coordinates specified relative to the instantaneous interface.

where $\mathbf{r}_i(t)$ is the position of the ith water molecule at time t and the sum is over all water molecules in the liquid phase. Here $\phi(x;\xi)$ is the truncated and shifted Gaussian function with the coarse-graining length ξ, given by

$$\phi(x;\xi) = \begin{cases} \mathcal{N}_c \left(e^{-x^2/2\xi^2} - e^{-9/2}\right), & \text{if } x \leq 3\xi, \\ 0\,, & \text{if } x > 3\xi, \end{cases} \tag{2.2}$$

where $\mathcal{N}_c$ is the normalization constant. Given the coarse-graining length, the interface is defined as the two-dimensional manifold $\mathbf{r} = \mathbf{s}$ that satisfies

$$\bar{\rho}(\mathbf{s}, t) = \rho_\mathrm{b}/2 \tag{2.3}$$

where $\rho_\mathrm{b} \approx 0.033\,\text{Å}^{-3}$ is the bulk density of water. In other words, we define the instantaneous interface to be points in space where the coarse-grained density field is equal to the half of the bulk density. Note that $\mathbf{s}$ is a dynamic quantity depending on the molecular configuration at given time, *i.e.*, $\mathbf{s} = \mathbf{s}(t) = \mathbf{s}(\{\mathbf{r}_i(t)\})$. To solve Eq. (2.3) for $\mathbf{s}(t)$, we interpolate the coarse-grained densities, $\bar{\rho}(\mathbf{r}, t)$, computed on a spatial grid for a given molecular configuration, $\{\mathbf{r}_i(t)\}$. Specifically we used a cubic lattice with a lattice spacing of 1 Å throughout this work. For the coarse-graining length, we used $\xi = 2.4\,\text{Å}$ that is large enough to avoid the occurrence of voids within the liquid phase [34]. For the normalization constant, we used $\mathcal{N}_c \approx 0.0051\,\text{Å}^{-3}$ that gives $\langle\bar{\rho}\rangle \approx \rho_\mathrm{b}$ in the bulk.

Once the instantaneous interface is located, we quantify the molecular coordinates with respect to the dynamic frame of reference. Specifically, we describe the position of each molecule in terms of its proximity from the interface, which is given by

$$a_i(t) = \{[\mathbf{s}(t) - \mathbf{r}_i(t)] \cdot \hat{\mathbf{n}}(t)\}\big|_{\mathbf{s}(t)=\mathbf{s}_i^*(t)} \tag{2.4}$$

where $\mathbf{s}_i^*(t)$ is the interfacial point nearest to $\mathbf{r}_i(t)$ and $\hat{\mathbf{n}}(t)$ is the unit vector normal to the interface at $\mathbf{s}(t)$, *i.e.*, the unit vector in the direction of $\nabla\bar{\rho}(\mathbf{r}, t)|_{\mathbf{r}=\mathbf{s}(t)}$. By definition, $a_i(t)$ is positive if the ith molecule is on the liquid side of the interface and it is negative otherwise. We also describe the molecular orientation in terms of the angles of OH bonds from the instantaneous surface normal, *i.e.*,

$$\theta_i^{(k)}(t) = \cos^{-1}\left(\frac{\mathbf{v}_i^{(k)}}{\left|\mathbf{v}_i^{(k)}\right|} \cdot \hat{\mathbf{n}}(t)\Big|_{\mathbf{s}(t)=\mathbf{s}_i^*(t)}\right) \tag{2.5}$$

where $\mathbf{v}_i^{(k)}$ is the kth OH bond vector of the i molecule starting from its oxygen and ending at its kth hydrogen ($k = 1, 2$). In the following sections, we demonstrate that the intrinsic coordinates of Eqs. (2.4) and (2.5) are useful for characterizing the interfacial molecular structure.

2.2 Liquid Water–Vapor Interface

The liquid water–vapor interface is the simplest form of a water interface. Here we analyze the atomistic simulation of an extended liquid water–vapor interface for its molecular structure. Specifically we consider three different classical force fields for simulating water molecules, SPC/E [35], TIP4P/2005 [24], and TIP5P [36]. In these force fields, a water molecule is modeled as a set of point charges within a rigid geometry which has the Coulomb interactions with the point charges of other molecules. As illustrated in Fig. 2.2, these force fields are widely dissimilar in the geometry and magnitudes of the point charges.[1] In this section, we examine how much the interfacial structures and properties depend on the details of the force fields. Also, we briefly discuss their relation to the hydrogen bonds at the interface.

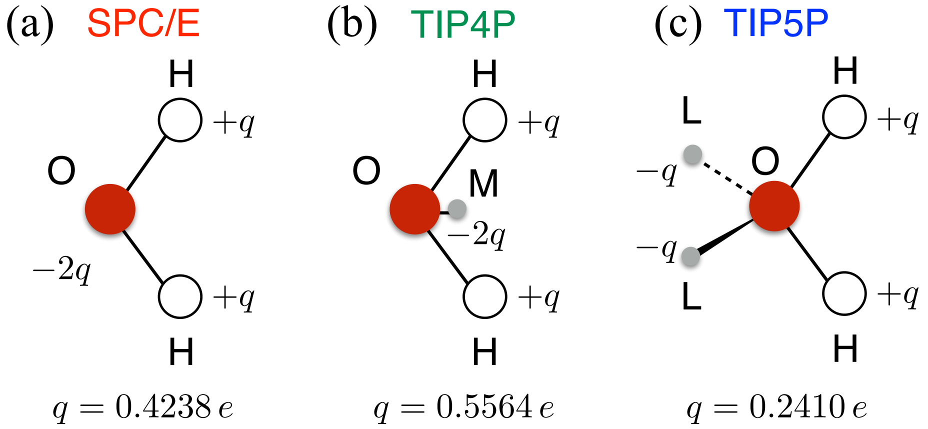

Figure 2.2 Geometries and magnitudes of the point charges in the (a) SPC/E, (b) TIP4P, and (c) TIP5P water models. Although not being indicated above, other geometric parameters such as r_{OH} and θ_{HOH} are also distinct among these force fields.

---

[1] In addition to the electrostatic interactions, water molecules are subject to the dispersive and repulsive forces based on the Lennard-Jones potential but the difference in the parameters for these interactions is not significant.

The details of our simulation methods are as follows. We simulated the liquid-vapor interfaces of SPC/E, TIP4P/2005, and TIP5P waters in NVT ensembles. Each system has 1944 water molecules in a slab geometry with dimensions of 5.0 nm × 5.0 nm × 3.0 nm, *i.e.*, the interface is extended along x and y directions. The system was equilibrated at $T = 298\,\mathrm{K}$ and Particle Mesh Ewald was used to handle the long-range part of electrostatic interactions with the periodic boundary conditions in all directions. The SHAKE and SETTLE algorithms were used to constrain the geometry of water. The molecular dynamics simulations were performed using the LAMMPS package [37] for the SPC/E and TIP4P force fields and the GROMACS package [38] for the TIP5P force field. Molecular configurations were sampled every 0.1 ps from six independently equilibrated simulations of 1 ns for the statistics. For each sampled configuration, the molecular coordinates relative to the intrinsic interface, $(a_i, \cos\theta_i^{(1)}, \cos\theta_i^{(2)})$, were identified according to the procedure in Sec. 2.1.

2.2.1 Density Profile and Orientational Distribution

Once we have the statistics of the intrinsic coordinates, $(a_i, \cos\theta_i^{(1)}, \cos\theta_i^{(2)})$, we can characterize the interfacial structure using their distribution functions. First, the distribution of the molecular proximity to the interface is connected to the quantity known as the *density profile*, $\rho(a)$, such that

$$\rho(a) = \frac{1}{L^2}\left\langle \sum_i \delta(a_i - a) \right\rangle \tag{2.6}$$

where $\delta(x)$ is the Dirac delta function and L is the length of the simulation cell parallel to the interface. Thus, $\rho(a)$ has the units of number density, Å^{-3}, and $\rho(\infty) = \rho_\mathrm{b}$. Figure 2.3(a) show the plots of the density profiles for the liquid–vapor interfaces of the three different water force fields. They have the same oscillatory structures with respect to their phases,[2] although there exists the quantitative difference in their amplitudes. In particular, TIP5P water exhibits the smaller amplitude in its density profile than others.

Since the angular coordinates, $(\cos\theta_i^{(1)}, \cos\theta_i^{(2)})$, specifies the molecular orientation, we can describe the *orientational distribution* at given interfacial proximity using the probability distribution given by

$$P(\vec{\kappa}|a) = \frac{\left\langle \sum_i \delta\big(\cos\theta_i^{(1)} - \cos\theta_{\mathrm{OH}}^{(1)}\big)\delta\big(\cos\theta_i^{(2)} - \cos\theta_{\mathrm{OH}}^{(2)}\big)\delta(a_i - a) \right\rangle}{\left\langle \sum_i \delta(a_i - a) \right\rangle}\,. \tag{2.7}$$

Here $\vec{\kappa}$ is a more general notation for the molecular orientation but is equivalent to the angular coordinates in the laterally isotropic environment like the liquid–vapor

---

[2] As the period of the oscillation is about the molecular diameter of water, the structure is mostly derived from the packing effect of the repulsive cores.

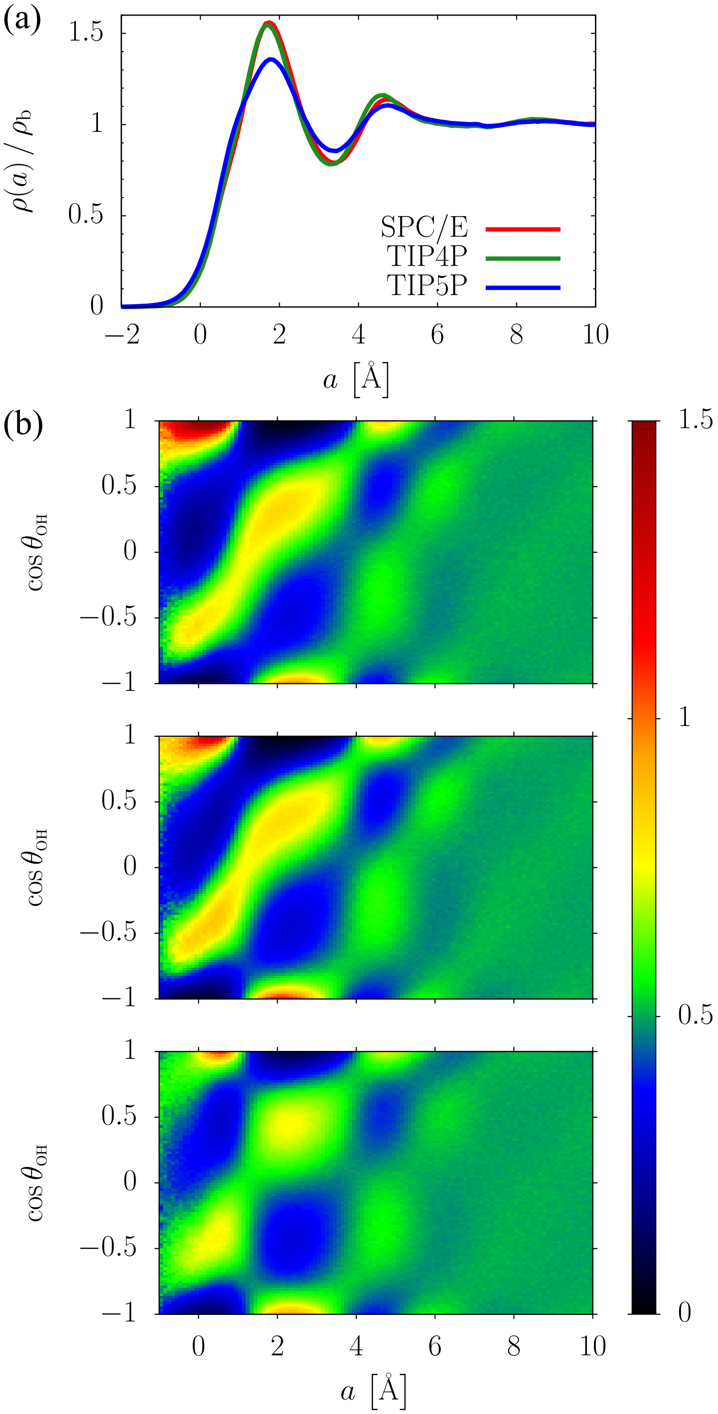

Figure 2.3 (a) Density profiles computed from the atomistic simulations of SPC/E, TIP4P, and TIP5P. They are normalized by the bulk density, ρ_{b}. (b) Orientational distributions, $P(\cos\theta_{\mathrm{OH}}|a)$, for SPC/E (top), TIP4P (middle), and TIP5P (bottom). Color shading indicates the probability density.

interface, *i.e.*, $P(\vec{\kappa}|a) = P\big(\cos\theta_{\mathrm{OH}}^{(1)}, \cos\theta_{\mathrm{OH}}^{(2)}|a\big)$. This high-dimensional distribution can be reduced into the lower-dimensional quantity such that

$$P(\cos\theta_{\mathrm{OH}}|a) = \int d\vec{\kappa} P(\vec{\kappa}|a) \left[\frac{1}{2}\sum_{i=1}^{2} \delta\big(\cos\theta_{\mathrm{OH}}^{(i)} - \cos\theta_{\mathrm{OH}}\big)\right] , \tag{2.8}$$

where $\int d\vec{\kappa}(\cdots)$ denotes the integration over all possible molecular orientations, and it is more convenient to visualize the depth-dependent feature of the orientational distribution. As illustrated in Fig. 2.3(b), $P(\cos\theta_{\mathrm{OH}}|a)$ exhibits qualitatively the same structural characteristics for the three different force fields of water. It shows the oscillation in the preference of a specific orientation depending on the interfacial proximity. While the water molecules in the topmost layer prefer to having a free or *dangling* OH bond ($\cos\theta_{\mathrm{OH}} \sim 1$), those in the next layer are more likely to orient one of its OH bonds toward the bulk ($\cos\theta_{\mathrm{OH}} \sim -1$). Like in the density profiles, there also exists the quantitative difference that the TIP5P water shows the smaller amplitude in the oscillatory structure of the orientational distribution than the SPC/E and TIP4P. These differences are mainly due to the fact that the TIP5P water is based on a tetrahedral scaffold with four charges while the SPC/E and TIP4P waters have three charges on triangular scaffolds.

As illustrated in Fig. 2.3, both density profile and orientational distribution suggest that the molecular structure of the liquid water–vapor interface is the most anisotropic for about 5–7 Å from the intrinsic interface which corresponds to 2–3 molecular diameters. It is remarkable that the characteristics of the interfacial molecular structure are qualitatively the same for the three classical force fields of water which have distinct geometries for the point charges. Since these structural characteristics are also preserved in the first-principles simulations [39], we suppose that the statistical nature of hydrogen bonds at the interface primarily accounts for the anisotropic structure in the orientational distribution. We further elaborate the relationship between the interfacial molecular structure and hydrogen bonding in the next chapter.

2.2.2 Interfacial Polarization and Polarizability

The liquid water–vapor interface exhibits the dielectric properties different from that of the bulk liquid. There exists net polarization or surface charge at an air–water interface [40–42] and the dielectric constant becomes much smaller than in the bulk [43–46]. These phenomena are mostly originated from the anisotropic orientational fluctuations at the interface, so here we demonstrate their effects on interfacial polarization and polarizability. Specifically, we quantify interfacial polarization in terms of the average dipole moment along the surface normal direction, which is given by

$$\langle \mu_{\hat{\mathbf{n}}}(a)\rangle = \mu_{\mathrm{w}} \frac{\left\langle \sum_i (\hat{\boldsymbol{\mu}}_i \cdot \hat{\mathbf{n}})\, \delta(a_i - a)\right\rangle}{\left\langle \sum_i \delta(a_i - a)\right\rangle}, \tag{2.9}$$

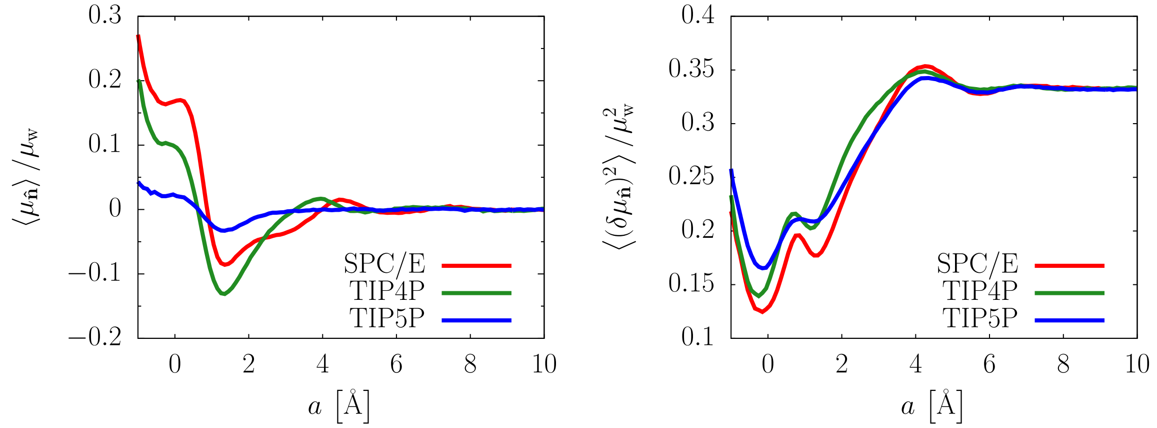

Figure 2.4 Interfacial (left) polarization, $\langle \mu_{\hat{\mathbf{n}}}(a) \rangle$, and (right) polarizability, $\langle (\delta\mu_{\hat{\mathbf{n}}}(a))^2 \rangle$, computed from the atomistic simulations with the SPC/E, TIP4P, and TIP5P waters.

where $\hat{\boldsymbol{\mu}}_i$ is the unit dipole vector of the ith molecule, *i.e.*, $\hat{\boldsymbol{\mu}}_i = \big(\mathbf{v}_i^{(1)} + \mathbf{v}_i^{(2)}\big) / \big|\mathbf{v}_i^{(1)} + \mathbf{v}_i^{(2)}\big|$, and μ_w is the dipole moment of an individual water molecule.[3]. Similarly, we compute the interfacial polarizability based on the mean square fluctuation of the dipole moment, which is given by

$$\langle (\delta\mu_{\hat{\mathbf{n}}}(a))^2 \rangle = \mu_\mathrm{w}^2 \frac{\left\langle \sum_i \left(\hat{\boldsymbol{\mu}}_i \cdot \hat{\mathbf{n}}\right)^2 \delta(a_i - a) \right\rangle}{\left\langle \sum_i \delta(a_i - a) \right\rangle} - \langle \mu_{\hat{\mathbf{n}}}(a) \rangle^2. \tag{2.10}$$

Although Eqs. (2.9) and (2.10) are straightforward expressions for computing the corresponding quantities from simulations, they depend on the orientational distribution, $P(\vec{\kappa}|a)$, explicitly as the orientation of each molecule determines its dipole moment (see Eqs. (3.8) and (3.9) in Chapter 3).

From the atomistic simulations, the orientational polarization and polarizability were computed according to the above expressions, and their interfacial profiles scaled in units of μ_w are plotted in Fig. 2.4. The plots show that these interfacial properties also share the qualitatively same feature among the three different force fields of water. The polarizations exhibit the quantitative difference in their scales, which should be related with the different amplitudes in the alternations of $P(\cos\theta_\mathrm{OH}|a)$. On the other hand, the polarizabilities have the almost identical trend across the force fields, where the decrease in the fluctuations by about a half at the interface is consistent with the interfacial behavior of the dielectric constant.

As the anisotropic orientational fluctuations are derived from hydrogen bonding in the anisotropic interfacial environment, the interfacial dielectric properties can be also related to the fluctuations of interfacial hydrogen bonds. If we look into the statistics of hydrogen bonds near the interface, the average number of donated hydrogens per

---

[3] μ_w, which is constant for the classical force fields, has slightly different value depending on the water model: 2.35 D for SPC/E, 2.305 D for TIP4P/2005, and 2.29 D for TIP5P.

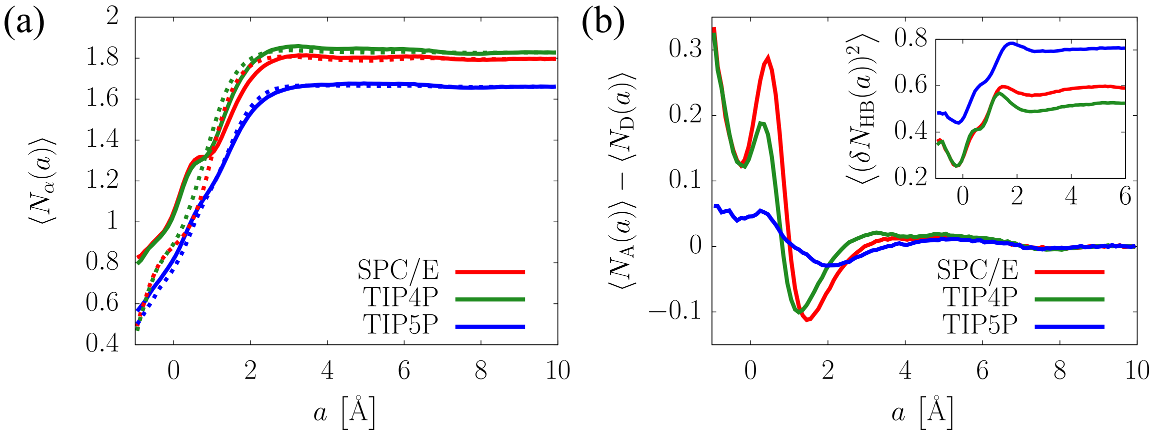

Figure 2.5 (a) Average number of hydrogen bonds through donor ($\alpha = \mathrm{D}$) and acceptor ($\alpha = \mathrm{A}$) sites per molecule, shown in dotted and solid lines, respectively. (b) Average excess number of accepting hydrogen bonds over donating hydrogen bonds, compared with the mean square fluctuation of the overall hydrogen bond number, $N_{\mathrm{HB}} = N_{\mathrm{D}} + N_{\mathrm{A}}$ (inset).

molecule is not balanced by that of accepted hydrogens as illustrated in Fig. 2.5(a).[4] Again, the statistics for the SPC/E and TIP4P waters are similar to each other while the TIP5P water gives the quantitatively different one. If we plot the unbalance between the hydrogen bond numbers as shown in the Fig. 2.5(b), it becomes clear that the three classical force fields share the qualitatively same trend which is indeed very similar to that of $\langle \mu_{\hat{\mathbf{n}}}(a)\rangle$. This similarity implies that the net polarization or surface charge at an air–water interface is derived from the asymmetric nature of water's hydrogen bonding within the anisotropic environment.[5] On the other hand, if we compute the mean square fluctuation of the overall hydrogen bond number, the results from the three classical water models exhibit the same feature that the fluctuations decrease by about a half at the interface compared to the bulk (see the inset of Fig. 2.5(b)). This behavior is consistent with that of $\langle(\delta\mu_{\hat{\mathbf{n}}}(a))^2\rangle$. In Chapter 3, we investigate more rigorously these interfacial variations in dielectric properties based on a statistical mechanical model of interfacial hydrogen bonds.

2.3 Hydrophobic Interface vs. Hydrophilic Interface

The interfacial behavior of liquid water is determined largely by the interaction between water and surface (or solute) in contact with. For instance, the macroscopic wetting behavior of a surface represents how much the surface–water interaction is favorable [28, 47]. A chemically nonpolar surface, which has negligible interactions with water, is not likely to be wet such that a water droplet forms large contact angle

---

[4] Here we specify the hydrogen bond statistics based on the number of hydrogens donated and accepted by a single molecule at given interfacial proximity, dented by $N_{\mathrm{D}}(a)$ and $N_{\mathrm{A}}(a)$, respectively. For the details about computing these quantities, refer to Eq. (3.25) and/or Ref. 41.

[5] More precisely, there occurs the charge transfer through a hydrogen-bonded pair such that the excess hydrogen bonds represent the charge cumulation [41].

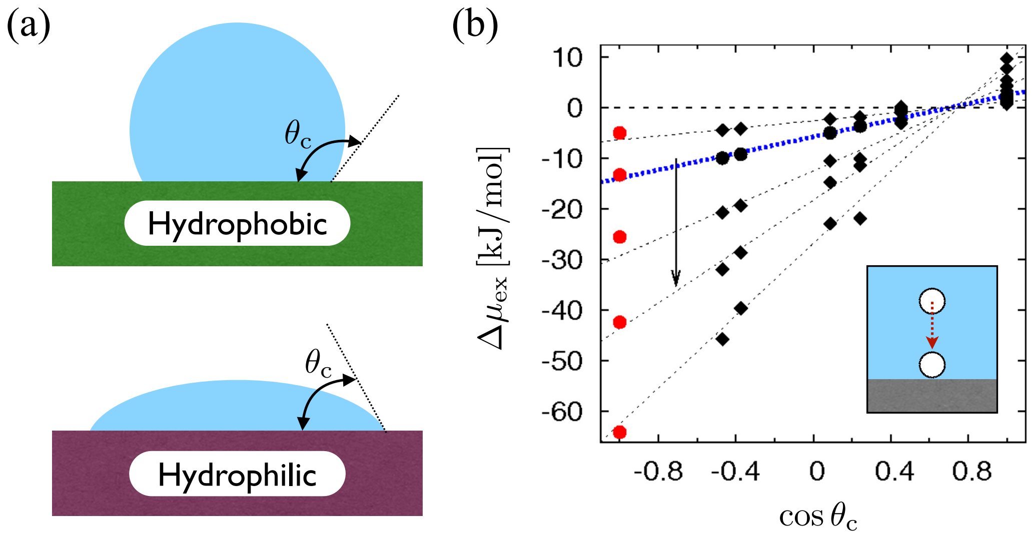

Figure 2.6 (a) Schematic illustration of the contact angle of a water droplet on hydrophobic (top) and hydrophilic (bottom) surfaces. (b) $\Delta\mu_{ex}$ for hard sphere solutes of different sizes, plotted with respect to $\cos\theta_c$ measured from a set of surfaces with different hydrophobicity, where the inset schematically illustrates the meaning of $\Delta\mu_{ex}$. Filled circles fit with the blue dotted line are for methane-sized solutes ($\sigma = 3.73$ Å) while the arrow indicates increasing solute size. This plot is adapted from Ref. 48.

against the surface. On the contrary, a polar surface prefers to be wet due to the favorable interactions with water such that it gives small contact angle. As illustrated in Fig. 2.6(a), we can thus estimate the *hydropathy scale* for a given surface based on the water contact angle, θ_c.[6]

The macroscopic wettability of a surface can be related with the microscopic density fluctuation near the surface [48, 49]. If the solvent density fluctuation is large near a given surface, the solvation of a small hydrophobe is favorable near the surface, which indicates that the surface is hydrophobic. Specifically, this effect is quantified by the solvation free energy or excess chemical potential at the interface relative to the bulk, which is denoted by $\Delta\mu_{ex}$ (its computational detail is given in Sec. **??**). As illustrated in Fig. 2.6(b), $\Delta\mu_{ex}$ is remarkably correlated with the macroscopic measure of hydrophobicity. Hence, $\Delta\mu_{ex}$ can be used to measure the microscopic hydropathy scale especially for a chemical heterogeneous surface such as a protein surface [50]. This method, however, is not so effective for probing the largely hydrophilic regime (*i.e.*, $\cos\theta_c > 0.4$) due to the sampling issue.[7]

In this work, we consider the interfacial molecular structure as a new basis for characterizing the microscopic hydropathy scale. Specifically, we focus on how the interfacial molecular structure is perturbed by a given surface. For a hydrophobic sur-

---

[6] If the water contact angle for a given surface is larger than 90°, it is typically considered to be hydrophobic.

[7] The density fluctuation facilitating a finite-size cavity becomes exponentially rare as the polarity of a given surface region increases. The precise measurement of $\Delta\mu_{ex}$ therefore needs exhaustive sampling which makes it difficult to characterize a dynamic surface of a protein.

face, the surface–water interaction is so weak that it cannot modulate the interfacial hydrogen bond arrangement imposed by the geometric constraint. Hence, the liquid water interface adjacent to a hydrophobic surface has essentially the same molecular structure as the liquid water–vapor interface [51]. In this context, we refer to the liquid water–vapor interface as an ideal hydrophobic interface since there is no external entity interacting with the interfacial water molecules.

The interfacial circumstance is quite different for the hydrophilic case. A typical hydrophilic surface has polar chemical groups capable of dipolar interactions with the adjacent water molecules. These interactions are directional and strong enough to modulate the hydrogen bonding structure between the interfacial water molecules as illustrated in Fig. 2.7(a). The molecular structure of a hydrophilic interface thus exhibits different features than that of a hydrophobic one. For its illustration, $P(\cos\theta_{\mathrm{OH}}|a)$ of the water interface at a disordered hydrophilic surface (see Sec. 5.2.1 for its detailed description) is contrasted with that of an ideal hydrophobic interface in Figure 2.7(b). They are disparate largely within a molecular diameter from the intrinsic interface as an effect of the hydrophilic interaction on water's interfacial hydrogen bonding structure.

As the interfacial molecular structure reflects the microscopic informations on the solute's surface, we can therefore utilize these informations to characterize the solute's hydration properties including the hydropathy scale. Based on this idea, we develop a novel theoretical framework that can characterize the solute's hydration property in Chapter 4. In Chapter 5, we investigate the relationship between surface–water interactions and water's interfacial hydrogen bonding structure in further detail.

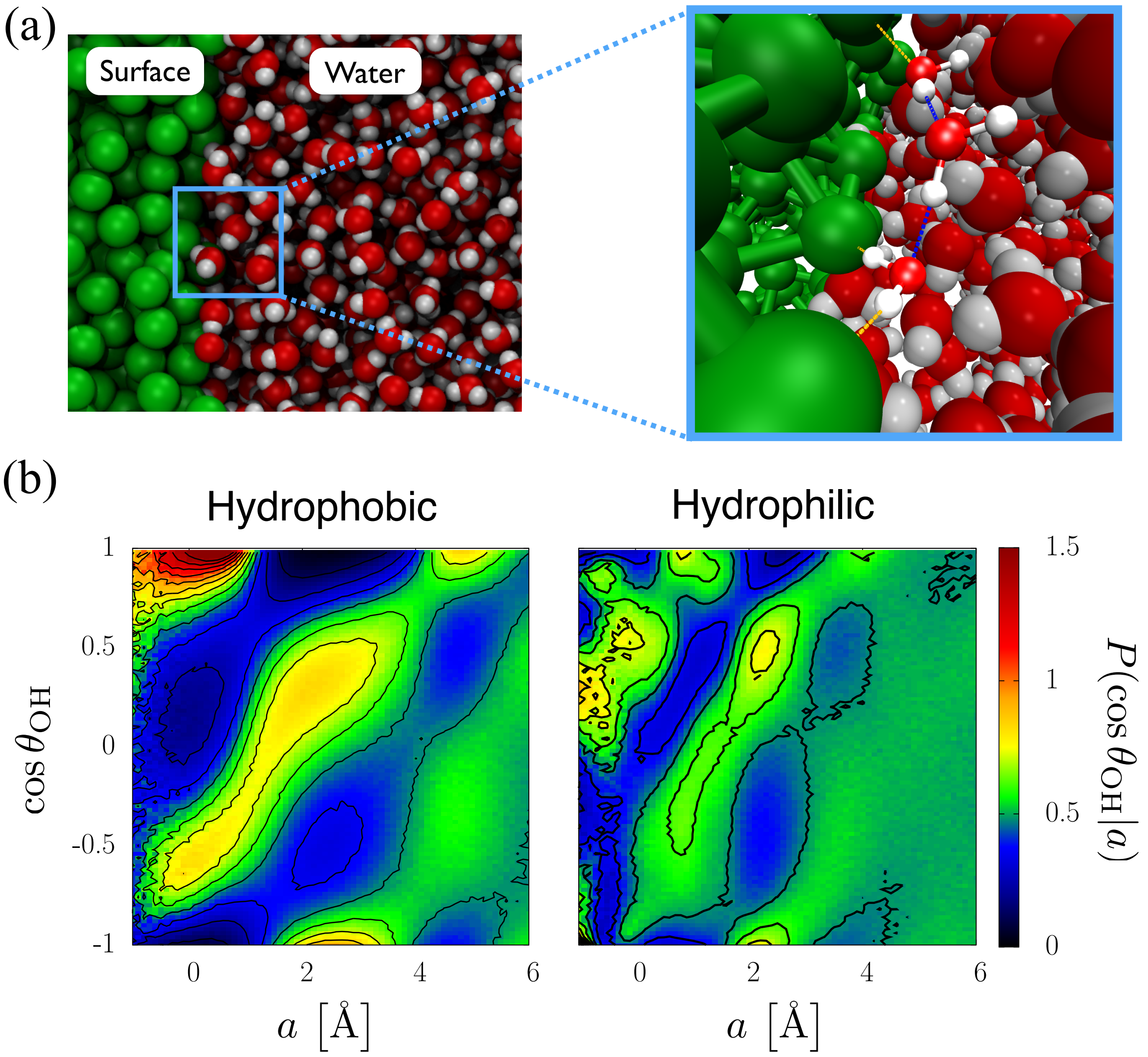

Figure 2.7 (a) Simulation snapshot of the interface between a model hydrophilic surface and liquid water. The magnified view on the right illustrates that the dipolar interactions between the surface and water, shown in yellow dashed line, affect the hydrogen bonding structure between the interfacial water molecules, shown in blue dashed lines. (b) Reduced orientational distributions, $P(\cos\theta_{\mathrm{OH}}|a)$, for a hydrophobic and hydrophilic interface, shown with color shading and contour lines.

Chapter 3

Three-Body Hydrogen Bond Defects Contribute Significantly to the Dielectric Properties of the Liquid Water-Vapor Interface

In this chapter,[1] we present a simple model of aqueous interfacial molecular structure and we use this model to isolate the effects of hydrogen bonding on the dielectric properties of the liquid water-vapor interface. We show that water's interfacial molecular structure can be understood by considering the orientational preferences of a single molecule immersed in the environment of the average interfacial density field. We illustrate that depth dependent orientational anisotropy is determined by the geometric constraints of hydrogen bonding and we show that the primary features of atomistic simulation data can be reproduced by assuming an idealized, perfectly tetrahedral hydrogen bonding geometry. We demonstrate that non-ideal hydrogen bond geometries are required to account for variations in the orientational polarization and polarizability of the interface. Finally, we highlight that these properties contain significant contributions from a specific type of geometrically distorted three-body hydrogen bond defect that is preferentially stabilized at the interface.

3.1 Introduction

The dielectric properties of liquid water are determined in large part by the orientational fluctuations of dipolar water molecules [52–55]. Near a liquid water-vapor interface these orientational fluctuations are anisotropic, leading to dielectric properties that differ significantly from their bulk values [41, 46, 56]. These differences are fundamental to interface-selective chemical and physical processes [25, 40, 57, 58], but they are generally difficult to access experimentally. In this chapter, we study these differences with a statistical mechanical model of interfacial hydrogen bonding. This

---

[1] This chapter borrows largely from the previously published work, *J. Phys. Chem. Lett.* **9**, 1649–1654 (2018).

model provides the ability to relate the microscopic characteristics of hydrogen bonding to the emergent properties of the liquid water interface. By comparing this model to the results of atomistic simulation we isolate the specific role of hydrogen bonding in determining interfacial molecular structure. We demonstrate that water's interfacial molecular structure is determined by the interplay between the anisotropic features of the interfacial density field and the molecular geometry of hydrogen bonding interactions. While many details of interfacial molecular structure reflect an idealized tetrahedral hydrogen bonding geometry, we show that only distorted non-tetrahedral hydrogen bond structures can contribute to changes in interfacial dielectric properties. We identify a specific type of non-tetrahedral hydrogen bond defect that is preferentially stabilized at the interface and show that it contributes significantly to the unique dielectric properties of the interfacial environment.

Our microscopic understanding of interfacial molecular structure derives primarily from a combination of surface-sensitive experiments, such as vibrational sum frequency generation [59–62], and atomistic simulation [34, 63–65]. This combination has revealed that the interfacial environment contains depth dependent molecular populations that vary in their orientational alignments. The details of this depth-dependent orientational molecular structure cannot be determined from existing experimental data alone and thus we rely on molecular simulation to supplement our molecular level understanding. The molecular structure predicted through the use of standard classical force fields, such as SPC/E [35] and TIP5P [36], are widely used in the study of water interfaces because they are both computationally efficient and have been shown to be consistent with available experimental data [66, 67].

Even at microscopic length scales the position of a liquid-vapor interface exhibits capillary wave-like spatial undulations [68, 69]. These undulations contribute to the properties of the interface but they also serve to blur out molecular scale details. The microscopic details of the actual phase boundary, *i.e.*, the *intrinsic interface* is difficult to isolate experimentally. In theoretical studies, however, the intrinsic interface and its spatial deformations can be treated separately. This chapter focuses on the intrinsic interface, defining all molecular coordinates relative to the time varying position of the instantaneous liquid phase boundary [34]. We identify the position of the phase boundary following the procedure described in Sec. 2.1. Our model is thus most valid over microscopic length scales, where the effects of surface roughening are negligible, however, since the deformations in the liquid-vapor phase boundary are well characterized by capillary wave theory [70–73], their effects are trivial to reincorporate to enable comparison to experiment.

Atomistic simulations have revealed that the molecular structure of the intrinsic water-vapor interface is anisotropic extending about 1 nm into the bulk liquid [34, 51]. This anisotropic molecular structure can be decomposed into two separate components: (1) an interfacial density field, $\rho(\mathbf{r})$, where $\mathbf{r}$ denotes the position measured relative to the instantaneous interface, and (2) a position-dependent probability distribution for molecular orientations, $P(\vec{\kappa}|\mathbf{r})$, where $\vec{\kappa}$ uniquely specifies the rotational configuration of a water molecule. The interplay between these two components is mediated by a combination of molecular packing effects and collective hydrogen bonding interactions. Classical density functional theory can be used to compute $\rho(\mathbf{r})$, but it does not provide explicit information about $P(\vec{\kappa}|\mathbf{r})$ [72, 74]. Here we present a theoretical model for computing $P(\vec{\kappa}|\mathbf{r})$ from $\rho(\mathbf{r})$, noting that the complete intrinsic interfacial molecular structure can therefore be derived by combining this model with an existing approach for computing $\rho(\mathbf{r})$.

3.2 A Mean-Field Model of Interfacial Hydrogen Bonding: The Rigid Tetrahedral Model

3.2.1 Formalism

Our model utilizes a mean field approach by computing $P(\vec{\kappa}|\mathbf{r})$ based on the orientational preferences of a single probe molecule immersed in the anisotropic mean density field of the intrinsic interface, $\rho(\mathbf{r})$. As illustrated in Fig. 3.1, the probe molecule is modeled as a point particle with four tetrahedrally coordinated hydrogen bond vectors, denoted $\mathbf{b}_1$, $\mathbf{b}_2$, $\mathbf{b}_3$, and $\mathbf{b}_4$. The length of these vectors are chosen to correspond to that of a hydrogen bond, so that each vector indicates the preferred position of a hydrogen bond partner. To mimic the hydrogen bonding properties of water, each bond vector is assigned a directionality, with $\mathbf{b}_1$ and $\mathbf{b}_2$ acting as hydrogen bond donors and $\mathbf{b}_3$ and $\mathbf{b}_4$ acting as hydrogen bond acceptors. The absolute orientations of these tetrahedral hydrogen bond vectors are specified by $\vec{\kappa}$.

The probe molecule interacts with the interfacial density field via an empirical hydrogen bonding potential, $E(\vec{\kappa}, \mathbf{r}, \{n_k\})$, which specifies the potential energy of a probe molecule with position $\mathbf{r}$, orientation $\vec{\kappa}$, and hydrogen bonding configuration $\{n_k\}$. We define $\{n_k\} \equiv (n_1, n_2, n_3, n_4)$, where n_i is a binary variable that indicates the hydrogen bonding state of the ith bond vector. Specifically, $n_i = 1$ if the probe molecule has formed a hydrogen bond along $\mathbf{b}_i$, and $n_i = 0$ if it has not. There are many possible ways to define this empirical hydrogen bonding potential. We begin by considering the simple form,

$$E(\vec{\kappa}, \mathbf{r}, \{n_k\}) = \sum_{i=1}^{4} \epsilon_{\mathrm{w}} n_i(\mathbf{r}, \mathbf{b}_i) \ , \tag{3.1}$$

where ϵ_{w} is the energy associated with forming a hydrogen bond. We treat the n_i's as independent random variables that are distributed according to,

$$n_i(\mathbf{r}, \mathbf{b}_i) = \begin{cases} 1, & \text{with probability } P_{\mathrm{HB}}(\mathbf{r}_i), \\ 0, & \text{with probability } 1 - P_{\mathrm{HB}}(\mathbf{r}_i), \end{cases} \tag{3.2}$$

where $\mathbf{r}_i = \mathbf{r} + \mathbf{b}_i$ denotes the terminal position of the ith bond vector and $P_{\mathrm{HB}}(\mathbf{r}_i)$ specifies the probability for successful hydrogen bonding at position $\mathbf{r}_i$.

In the context of this model, the probability for a molecule at position $\mathbf{r}$ to adopt an orientation, $\vec{\kappa}$, can thus be expressed as,

$$P(\vec{\kappa}|\mathbf{r}) = \left\langle e^{-\beta E(\vec{\kappa}, \mathbf{r}, \{n_k\})} \right\rangle_{\mathrm{b}} / Z(\mathbf{r}), \tag{3.3}$$

where $\langle \cdots \rangle_{\mathrm{b}}$ denotes an average over all possible hydrogen bonding states (*i.e.*, variations in the n_i's), $1/\beta$ is the Boltzmann constant, k_B, times temperature T, and $Z(\mathbf{r}) = \int d\vec{\kappa} \left\langle e^{-\beta E(\vec{\kappa},\mathbf{r},\{n_k\})} \right\rangle_{\mathrm{b}}$ is the orientational partition function for the probe molecule at position $\mathbf{r}$. By evaluating the average explicitly, the numerator of Eq. (3.3) can be written as,

$$\left\langle e^{-\beta E(\vec{\kappa},\mathbf{r},\{n_k\})} \right\rangle_{\mathrm{b}} = \prod_{i=1}^{4} \left[1 + P_{\mathrm{HB}}\left(\mathbf{r}_i\right)(e^{-\beta\epsilon_{\mathrm{w}}} - 1)\right], \tag{3.4}$$

and this equation, when combined with Eq. (3.3) provides a general analytical framework for computing the orientational molecular structure of an interface with a given density profile, $\rho(\mathbf{r})$.

We simplify this general theoretical model by assuming that $P_{\mathrm{HB}}(\mathbf{r}_i) \propto \rho(\mathbf{r}_i)$, where the value of the proportionality constant is chosen to match bulk hydrogen bonding statistics. Furthermore, we assume that the intrinsic interface is laterally isotropic and planar over molecular length scales. According to this assumptions, functions that depend on $\mathbf{r}$ to be expressed in terms of a, which denotes the

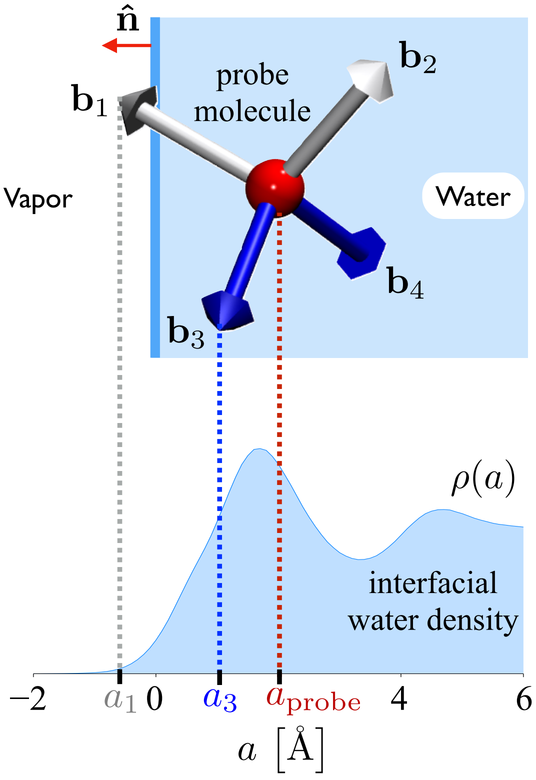

Figure 3.1 (a) Schematic depiction of the mean-field model showing a probe molecule with tetrahedrally coordinated bond vectors (white for donor, blue for acceptor) within the liquid (blue shaded region) at a distance a_{probe} from the position of the instantaneous interface (solid blue line). A plot of the interfacial density profile, $\rho(a)$, obtained from the atomistic simulation with TIP5P water, is shown with dotted lines indicating the termination points of bond vectors $\mathbf{b}_1$ and $\mathbf{b}_3$.

scalar distance from the instantaneous interface measured perpendicular to the interfacial plane. For instance, with this assumption the function $P_{\mathrm{HB}}(\mathbf{r})$ is simplified to $P_{\mathrm{HB}}(a_i) \propto \rho(a_i)$, where a_i is given by $a_i = a - \mathbf{b}_i \cdot \hat{\mathbf{n}}$, and $\hat{\mathbf{n}}$ is the unit vector normal to the plane of the interface (see Fig. 3.1).

In this section, we consider an idealized variation of our model in which the hydrogen bond vectors are of fixed length, $d_{\mathrm{HB}} = 2.8\,\text{Å}$ (*i.e.*, the equilibrium hydrogen bond distance [75]), and rigidly arranged with an ideal tetrahedral geometry (*i.e.*, $\mathbf{b}_i \cdot \mathbf{b}_j = \cos\theta_{\mathrm{T}} = -1/3$ for $i \neq j$). We refer to this model as the *rigid tetrahedral model.* Here we derive physical insight into the role of hydrogen bonding in water's interfacial molecular structure by comparing the interfacial quantities predicted by our model to the those computed from the atomistic simulations.

3.2.2 Optimization for Hydrogen Bond Energy Parameter

We parameterize our model by comparing to the results of atomistic simulations (refer to Sec. 2.2 for the details of simulations). We perform this comparison using the reduced orientational distribution function,

$$P(\cos\theta_{\mathrm{OH}}|a) = \int d\vec{\kappa} P(\vec{\kappa}|a) \left[\frac{1}{2} \sum_{i=1}^{2} \delta(\cos\theta_i - \cos\theta_{\mathrm{OH}}) \right], \tag{3.5}$$

where the summation is taken over the two donor bond vectors, $\cos\theta_i = \mathbf{b}_i \cdot \hat{\mathbf{n}}/|\mathbf{b}_i|$, and $\delta(x)$ is the Dirac delta function. Specifically, we determine free parameter, ϵ_{w}, by minimizing the Kullback-Leibler divergence [76] for $P(\cos\theta_{\mathrm{OH}}|a)$ computed from our model with respect to that from atomistic simulation, which is given by

$$\Gamma(\epsilon_{\mathrm{w}}) = \int da \int d(\cos\theta_{\mathrm{OH}})\, P_{\mathrm{ref}}(\cos\theta_{\mathrm{OH}}|a) \ln \left[\frac{P_{\mathrm{ref}}(\cos\theta_{\mathrm{OH}}|a)}{P_{\mathrm{MF}}(\cos\theta_{\mathrm{OH}}|a, \epsilon_{\mathrm{w}})} \right], \tag{3.6}$$

where $P_{\mathrm{ref}}(\cos\theta_{\mathrm{OH}}|a)$ and $P_{\mathrm{MF}}(\cos\theta_{\mathrm{OH}}|a, \epsilon_{\mathrm{w}})$ are the reduced orientational distributions obtained from atomistic simulation and our mean-field model, respectively. This quantity measures how far the probability distribution of our model deviates from the reference distribution given ϵ_{w}, and thus we refer to $\Gamma(\epsilon_{\mathrm{w}})$ as a *fitness* function. We choose the parameter that minimizes the fitness function,

$$\epsilon_{\mathrm{w}}^{*} = \arg\min_{\epsilon_{\mathrm{w}}} \{\Gamma(\epsilon_{\mathrm{w}})\}, \tag{3.7}$$

as the effective hydrogen bond energy. Figure 3.2 illustrates this optimization graphically.

For the TIP5P force field [36], this parameterization yields $\epsilon_{\mathrm{w}}^{*} = -1.4 k_B T = -3.47\,\mathrm{kJ/mol}$ at $T = 298\,\mathrm{K}$.[2] We find that different water models yield similar value of $\epsilon_{\mathrm{w}}^{*}$ (see Sec. 3.4.2). We note that this value includes the effects of environmental stabilization on broken hydrogen bonds and is therefore significantly lower in magnitude

---

[2] For the comparison to the simulation results, we mainly consider the TIP5P force field as a reference because our model is built upon the tetrahedral scaffold with four bonding sites.

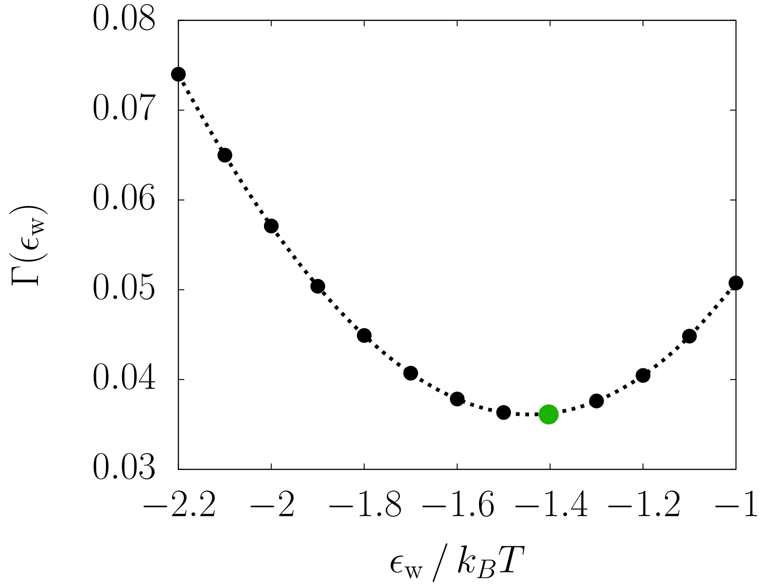

Figure 3.2 Plot of the fitness function, $\Gamma(\epsilon_{\mathrm{w}})$, showing that the hydrogen bond energy parameter of the rigid tetrahedral model is optimized near the green circle with respect to the atomistic simulation of the TIP5P water.

than absolute hydrogen bond energies [75, 77]. This demonstrates that our parameterized hydrogen bond strength is similar to estimates based on X-ray absorption measurements [78, 79], which highlights that this effective bonding energy determines the relevant energy scale for fluctuations in the structure of aqueous hydrogen bond networks.

In Fig. 3.3, $P_{\mathrm{MF}}(\cos\theta_{\mathrm{OH}}|a, \epsilon_{\mathrm{w}}^{*})$ is plotted along with $P_{\mathrm{ref}}(\cos\theta_{\mathrm{OH}}|a)$ that is computed from simulations with the TIP5P water. The orientational distribution obtained from the rigid tetrahedral model is remarkably similar to that from the atomistic simulation. This similarity illustrates that the seemingly complicated depth dependent orientational patterns in $P(\cos\theta_{\mathrm{OH}}|a)$ have simple physical origins. Namely, these patterns are determined by the constraints imposed on tetrahedral coordination by the anisotropic interfacial density field.

3.2.3 Conservation of Polarization and Polarizability

The effect of molecular dipole orientations on interfacial polarization and polarizability can be computed from $P(\vec{\kappa}|a)$. We specify orientational polarization in terms of the average dipole field,

$$\langle \mu_{\hat{\mathbf{n}}}(a) \rangle = \mu_{\mathrm{w}} \int d\vec{\kappa} P(\vec{\kappa}|a) \left[\hat{\boldsymbol{\mu}}(\vec{\kappa}) \cdot \hat{\mathbf{n}} \right], \tag{3.8}$$

where $\hat{\boldsymbol{\mu}}(\vec{\kappa})$ is the unit dipole vector of tagged molecule in particular orientation (*i.e.*, $\hat{\boldsymbol{\mu}} = (\mathbf{b}_1 + \mathbf{b}_2)/|\mathbf{b}_1 + \mathbf{b}_2|$) and μ_{w} is the dipole moment of an individual water molecule. Similarly, the orientational polarizability can be related to the fluctuations

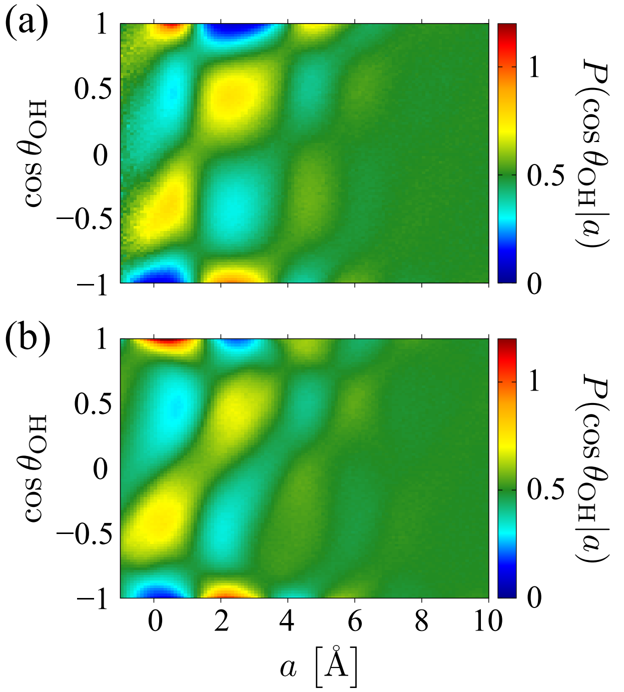

Figure 3.3 (a) contain plots of the orientational distribution function, $P(\cos\theta_{\mathrm{OH}}|a)$ (see Eq. (5.11)), as indicated by shading, computed from atomistic simulation and from the rigid tetrahedral model respectively.

in the dipole field [53],

$$\langle(\delta\mu_{\hat{\mathbf{n}}}(a))^2\rangle = \mu_{\mathrm{w}}^2 \int d\vec{\kappa} P(\vec{\kappa}|a) \left[\hat{\boldsymbol{\mu}}(\vec{\kappa}) \cdot \hat{\mathbf{n}}\right]^2 - \langle\mu_{\hat{\mathbf{n}}}(a)\rangle^2. \tag{3.9}$$

In Fig. 3.4, we compare the functions in Eqs. (3.8) and (3.9) that are computed from our model with those obtained from the atomistic simulations of the TIP5P force fields. As the atomistic simulation data illustrates, both $\langle\mu_{\hat{\mathbf{n}}}(a)\rangle$ and $\langle(\delta\mu_{\hat{\mathbf{n}}}(a))^2\rangle$ vary significantly from their bulk values at the liquid vapor interface. However, these variations are not captured by the rigid tetrahedral model, despite the ability of this model to capture the primary features of $P(\cos\theta_{\mathrm{OH}}|a)$. In fact, the rigid tetrahedral model predicts that $\langle\mu_{\hat{\mathbf{n}}}(a)\rangle$ and $\langle(\delta\mu_{\hat{\mathbf{n}}}(a))^2\rangle$ are independent of the interfacial depth (dashed lines in Fig. 3.4).

The depth-independent behavior of the rigid tetrahedral model in its polarization and polarizability is a mathematical consequence of modeling hydrogen bonds as perfectly tetrahedral and energetically symmetric for donor and acceptor bonds. The perfectly tetrahedral coordination gives $\sum_{i=1}^{4} \mathbf{b}_i = 0$ for any $\vec{\kappa}$. Because of the symmetry, any pair of distinct i and j can represent the donor bonds such that $\langle\boldsymbol{\mu}\rangle = \mu_{\mathrm{w}}\langle\hat{\boldsymbol{\mu}}\rangle \propto \langle\mathbf{b}_i + \mathbf{b}_j\rangle = 0$ for any orientational distribution. The dipole vector also can be decomposed such that $\boldsymbol{\mu} = \sum_{k=1}^{3} \mu_{\hat{\mathbf{e}}_k} \hat{\mathbf{e}}_k$ where $\hat{\mathbf{e}}_k$'s are orthonormal vectors in three dimensions. Choosing $\hat{\mathbf{e}}_1 = \hat{\mathbf{n}}$, we have $\langle\mu_{\hat{\mathbf{n}}}\rangle = \langle\boldsymbol{\mu} \cdot \hat{\mathbf{n}}\rangle = \langle\boldsymbol{\mu}\rangle \cdot \hat{\mathbf{n}} = 0$. Here $\hat{\mathbf{n}}$ could be other two unit vectors and there is no preference along specific direction. That is, since $|\boldsymbol{\mu}|^2 = \sum_{k=1}^{3} \mu_{\hat{\mathbf{e}}_k}^2 = \mu_{\mathrm{w}}^2$, we expect $\langle\mu_{\hat{\mathbf{n}}}^2\rangle = \mu_{\mathrm{w}}^2/3$.

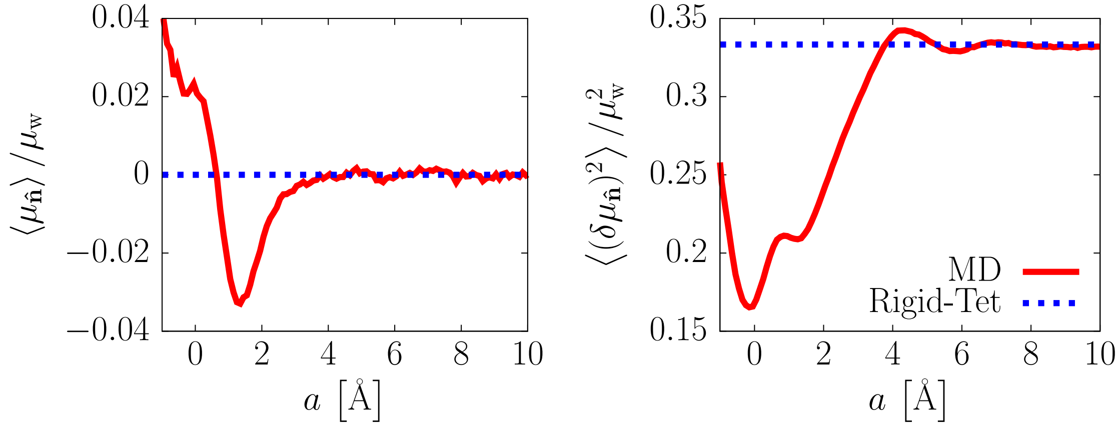

Figure 3.4 Interfacial mean dipole orientation, $\langle \mu_{\hat{\mathbf{n}}}(a) \rangle$, and dipole fluctuations, $\langle (\delta \mu_{\hat{\mathbf{n}}}(a))^2 \rangle$, computed from the molecular dynamics simulation (MD, solid red lines) and the rigid tetrahedral model (Rigid-Tet, blue dashed lines).

Therefore, interfacial variations in orientational polarization and polarizability must arise through a combination of (1) distortions in tetrahedral coordination geometry and (2) asymmetry in donor/acceptor hydrogen bond energies. We can study the specific influence of these effects on $\langle \mu_{\hat{\mathbf{n}}}(a) \rangle$ and $\langle (\delta \mu_{\hat{\mathbf{n}}}(a))^2 \rangle$ by explicitly including their effects in the empirical hydrogen bonding interaction of our mean field model. As demonstrated in the following section, three-body interactions are the significant components that modulate the hydrogen bonding fluctuations at the interface.

3.3 Effects of Three-Body Interactions at the Interface

3.3.1 Fluctuations in Hydrogen Bond Geometry and the Three-Body Hydrogen Bond Defects

In this section, we analyze the microscopic hydrogen bonding properties from atomistic simulations for the insight into modifying our empirical hydrogen bonding description. We quantify the hydrogen bond geometry of individual molecules by specifying the *inter-bond* angle, ψ, between pairs of hydrogen bonds. As Fig. 3.5(a) illustrates, there are six such angles for a molecule with four unique hydrogen bond partners. The probability distribution for ψ, $P(\psi)$, computed from atomistic simulation is plotted in Fig. 3.5(b). This plot highlights that the interfacial environment features highly distorted non-ideal hydrogen bond geometries that depend on the directionality (*i.e.*, donor or acceptor) of the two adjacent hydrogen bonds. Specifically interfacial inter-bond angles are narrowed relative to that of the bulk, and this narrowing is especially significant between bonds with like directionality. Furthermore, as illustrated in Fig. 3.6(a), we observe a significant increase in the relative fraction of highly distorted hydrogen bond configurations within the first 2 Å of the interfacial region.

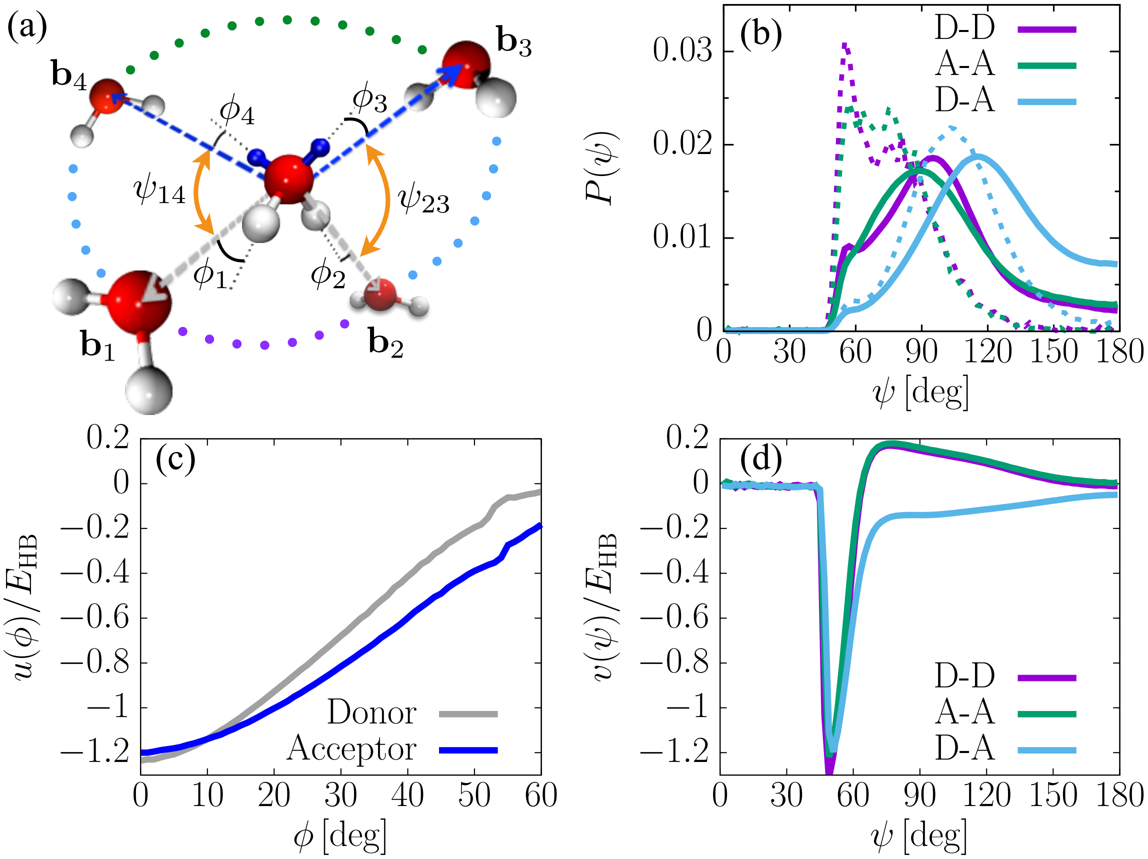

Figure 3.5 (a) A schematic illustration of the angles used to quantify hydrogen bond geometries. (b) Probability distributions for inter-bond angles, ψ, generated from atomistic simulation, computed separately for donor-donor (D-D), acceptor-acceptor (A-A), and donor-acceptor (D-A) pairs of bonds. Solid and dashed lines correspond to statistics generated within the bulk liquid and at the interface (*i.e.*, $|a| < .1\,\text{Å}$) respectively. (c) Average direct interaction energy, $u(\phi)$, expressed in units of the average bulk hydrogen bond energy, $E_{\mathrm{HB}} = 20.9\,\mathrm{kJ/mol}$, between a tagged molecule and individual hydrogen bond partners, computed separately for donor and acceptor bonds. (d) Average direct interaction energy, $v(\psi)$, between two hydrogen bond partners of a tagged molecule, as indicated by the dotted arcs in panel (a), computed separately for the case of two donor partners, two acceptor partners, and one acceptor and one donor.

We quantify the energetic properties of these highly distorted hydrogen bonds by analyzing atomistic simulation data. As Fig. 3.5(c) illustrates, the average direct interaction energy between a tagged molecule and one of its hydrogen bond partners is significantly weakened when the bond is distorted away from its preferred tetrahedral geometry. Despite this weakening, however, we observe that highly distorted hydrogen bond configurations can be stabilized by favorable interactions between hydrogen bond partners. As Fig. 3.5(d) illustrates, these interactions become particularly favorable when $\psi \approx 60$ deg, where the hydrogen bond partners are separated by approximately d_{HB}, and thus well situated to form a hydrogen bond. The resulting structure, a triangular three-body hydrogen bond defect, is unfavorable in the bulk

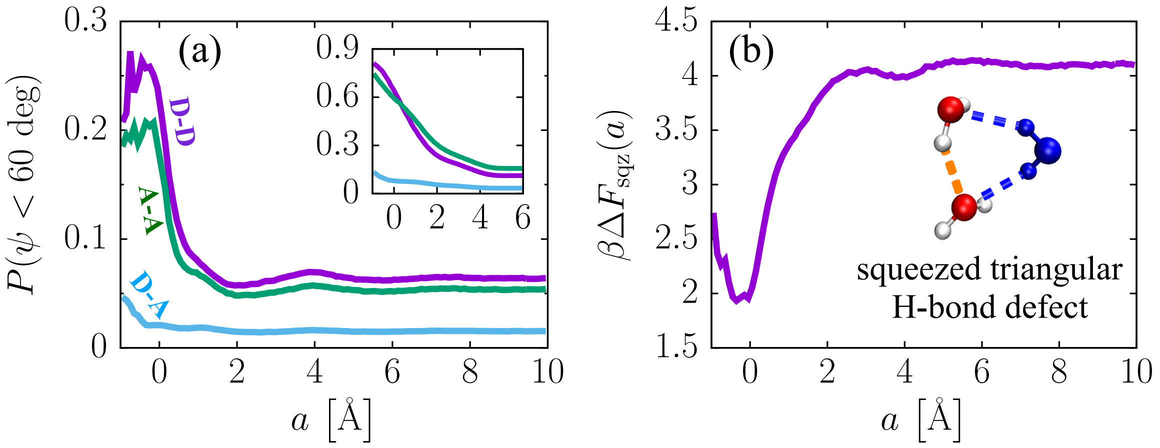

Figure 3.6 (a) Probability of observing $\psi < 60$ deg at varied interfacial depth from the atomistic simulation and our model (inset). Labels indicating the types of bond pairs are given in the same colors of lines. (b) Interfacial profile of free energy change associated with the distortion into a squeezed triangular hydrogen bond defect. Plot shown above is for the case including two donor bonds.

liquid, however, at the interface this defect structure is stabilized by an increased availability of broken hydrogen bonds [80], which due to the presence of the liquid phase boundary, cannot all be satisfied without significant distortions in hydrogen bond geometries.

Three-body interactions have been found to be an important element of water's molecular structure both in the bulk and at the interface [81–84]. The three-body defects that we have identified here are structurally different from those that have been found to facilitate the orientational relaxation dynamics within the bulk liquid [23] and are uniquely stabilized at the interface. We quantify the stabilizing effect of the interface by computing the relative free energy for squeezed triangular hydrogen bond defects, $\beta\Delta F_{\mathrm{sqz}}(a) = -\ln\left[P_{\mathrm{sqz}}(a)/(1 - P_{\mathrm{sqz}}(a))\right]$, where $P_{\mathrm{sqz}}(a)$ denotes the probability to observe a molecule with position a that is part of such a defect (see Eq. (3.18) and the following subsection for computational details). As Fig. 3.6(b) illustrates, these defects are more stable at the interface than in the bulk liquid by about $2\,k_B T$.

3.3.2 Computational Details

We quantify the distortions in hydrogen bond geometry and the associated energetics by analyzing the atomistic simulation results as follows. Notably, here relatively simple algorithms for quantifying various aspects of molecular geometry translate into complicated mathematical expressions. Let $\mathbf{v}_k^{(i)} = \mathbf{r}_k^{(i)} - \mathbf{r}_{\mathrm{O}}^{(i)}$, where $\mathbf{r}_{\mathrm{O}}^{(i)}$ is the position of the oxygen of the ith water molecule and $\mathbf{r}_k^{(i)}$ is the position of the kth bonding site on it ($k = 1, 2$ indicate the hydrogens and $k = 3, 4$ indicate the lone pairs for the TIP5P water). Then $\mathbf{v}_k^{(i)}$ represents the direction of ideal hydrogen bonding coordination through the kth site of the ith molecule. For the jth molecule neighboring the ith, its deviation angle from the ideal coordination to the ith molecule is given by

$$\phi_j^{(i)} = \min_k \left\{ \cos^{-1}\left(\frac{\mathbf{v}_k^{(i)} \cdot \mathbf{b}_j^{(i)}}{\left|\mathbf{v}_k^{(i)}\right| \left|\mathbf{b}_j^{(i)}\right|} \right) \right\}, \tag{3.10}$$

where $\mathbf{b}_j^{(i)} = \mathbf{r}_{\mathrm{O}}^{(j)} - \mathbf{r}_{\mathrm{O}}^{(i)}$ represents the hydrogen bond vector of the ith molecule to the jth. The corresponding index,

$$y_j^{(i)} = \arg\min_k \left\{ \cos^{-1}\left(\frac{\mathbf{v}_k^{(i)} \cdot \mathbf{b}_j^{(i)}}{\left|\mathbf{v}_k^{(i)}\right| \left|\mathbf{b}_j^{(i)}\right|} \right) \right\}, \tag{3.11}$$

indicates which ideal boding direction $\mathbf{b}_j^{(i)}$ is distorted from and thus whether it belongs to donor or acceptor hydrogen bond. The inter-bond angle between the jth and kth molecules with respect to the ith is given by

$$\psi_{jk}^{(i)} = \cos^{-1}\left(\frac{\mathbf{b}_j^{(i)} \cdot \mathbf{b}_k^{(i)}}{\left|\mathbf{b}_j^{(i)}\right| \left|\mathbf{b}_k^{(i)}\right|} \right). \tag{3.12}$$

Then the probability distribution of inter-bond angle at given distance a is computed as,

$$P_{\alpha\gamma}(\psi|a) = \frac{\left\langle \sum_i \sum_{j\neq i} \sum_{k\neq i>j} \delta(\psi_{jk}^{(i)} - \psi)\delta(a^{(i)} - a)\Theta_{\mathrm{hyd}}\left(\mathbf{b}_j^{(i)}\right)\Theta_{\mathrm{hyd}}\left(\mathbf{b}_k^{(i)}\right)\Phi_\alpha\left(y_j^{(i)}\right)\Phi_\gamma\left(y_k^{(i)}\right) \right\rangle}{\sin\psi \left\langle \sum_i \sum_{j\neq i} \sum_{k\neq i>j} \delta(a^{(i)} - a)\Theta_{\mathrm{hyd}}\left(\mathbf{b}_j^{(i)}\right)\Theta_{\mathrm{hyd}}\left(\mathbf{b}_k^{(i)}\right)\Phi_\alpha\left(y_j^{(i)}\right)\Phi_\gamma\left(y_k^{(i)}\right) \right\rangle}, \tag{3.13}$$

where $a^{(i)}$ is the interfacial depth of the ith molecule specified by Eq. (2.4),

$$\Theta_{\mathrm{hyd}}(\mathbf{r}) = H(|\mathbf{r}| - 2.4\,\text{Å})H(3.2\,\text{Å} - |\mathbf{r}|) \tag{3.14}$$

selects the molecules only in the first hydration shell of the ith molecule using the Heaviside step function, $H(x)$, and

$$\Phi_\alpha(x) = \begin{cases} H(2.5 - x), & \text{if } \alpha \text{ is Donor,} \\ H(x - 2.5), & \text{if } \alpha \text{ is Acceptor,} \end{cases} \tag{3.15}$$

selects the neighboring molecule of specific bond type, α. Here the geometric factor, $\sin\psi$, corrects the bias coming from the variation of solid angle. Fig. 3.5(b) shows the plots of $P_{\alpha\gamma}(\psi|a)$ with $a = 10\,\text{Å}$ and $a = 0\,\text{Å}$ for the bulk and interface respectively ($0.1\,\text{Å}$ was used for the binning width of histogram). For the plots in Fig. 3.6(a), the distribution is integrated such that $P_{\alpha\gamma}(\psi < 60°|a) = \int_0^{60°} P_{\alpha\gamma}(\psi|a)\sin\psi d\psi$.

The average direct interaction energy for a hydrogen bond pair is computed in the bulk phase as a function of the deviation angle, ϕ, such that

$$u_\alpha(\phi) = \frac{\left\langle \sum_i \sum_{j\neq i} U_{ij}\, \delta(\phi_j^{(i)} - \phi) H(a^{(i)} - a_b) \Theta_{\mathrm{hyd}}\left(\mathbf{b}_j^{(i)}\right) \Phi_\alpha\left(y_j^{(i)}\right) \right\rangle}{\left\langle \sum_i \sum_{j\neq i} \delta(\phi_j^{(i)} - \phi) H(a^{(i)} - a_b) \Theta_{\mathrm{hyd}}\left(\mathbf{b}_j^{(i)}\right) \Phi_\alpha\left(y_j^{(i)}\right) \right\rangle}, \tag{3.16}$$

where U_{ij} is the pair potential energy between the ith and jth molecules and $a_b = 10\,\text{Å}$. The plots are given in Fig. 3.5(c), normalized by the average bulk hydrogen bond energy where we used $E_{\mathrm{HB}} = 9.0\,k_BT$ (see the next section below for more details on this). Similarly, the average direct interaction energy between two neighbors of a tagged molecule is computed as,

$$v_{\alpha\gamma}(\psi) = \frac{\left\langle \sum_i \sum_{j\neq i} \sum_{k\neq i>j} U_{jk}\, \delta(\psi_{jk}^{(i)} - \psi) H(a^{(i)} - a_b) \Theta_{\mathrm{hyd}}\left(\mathbf{b}_j^{(i)}\right) \Theta_{\mathrm{hyd}}\left(\mathbf{b}_k^{(i)}\right) \Phi_\alpha\left(y_j^{(i)}\right) \Phi_\gamma\left(y_k^{(i)}\right) \right\rangle}{\left\langle \sum_i \sum_{j\neq i} \sum_{k\neq i>j} \delta(\psi_{jk}^{(i)} - \psi) H(a^{(i)} - a_b) \Theta_{\mathrm{hyd}}\left(\mathbf{b}_j^{(i)}\right) \Theta_{\mathrm{hyd}}\left(\mathbf{b}_k^{(i)}\right) \Phi_\alpha\left(y_j^{(i)}\right) \Phi_\gamma\left(y_k^{(i)}\right) \right\rangle}. \tag{3.17}$$

Computing $P_{\mathrm{sqz}}(a)$ needs to specify the certain type of defect among the configurations of $\psi < 60°$. There is the other type of defect than the squeezed triangular one, which is known as the intermediate of the water reorientation [23]. This type of defect has bifurcated hydrogen bonds through one site of the molecule such that $y_j^{(i)} = y_k^{(i)}$. By excluding such cases, we can compute the probability to observe a squeezed configuration of two donor bonds as,

$$P_{\mathrm{sqz,DD}}(a) = \frac{\left\langle \sum_i \sum_{j\neq i} \sum_{k\neq i>j} H(\psi_{jk}^{(i)} - 60°) \delta(a^{(i)} - a) \Theta_{\mathrm{hyd}}\left(\mathbf{b}_j^{(i)}\right) \Theta_{\mathrm{hyd}}\left(\mathbf{b}_k^{(i)}\right) \delta\left(y_j^{(i)} y_k^{(i)} - 2\right) \right\rangle}{\left\langle \sum_i \sum_{j\neq i} \sum_{k\neq i>j} \delta(a^{(i)} - a) \Theta_{\mathrm{hyd}}\left(\mathbf{b}_j^{(i)}\right) \Theta_{\mathrm{hyd}}\left(\mathbf{b}_k^{(i)}\right) \Phi_{\mathrm{D}}\left(y_j^{(i)}\right) \Phi_{\mathrm{D}}\left(y_k^{(i)}\right) \right\rangle}. \tag{3.18}$$

3.4 The Three-Body Fluctuation Model

We incorporate the effects of these three-body interactions into our model by including angle dependence in the empirical hydrogen bond potential. We accomplish this by allowing the angles of the hydrogen bonds to fluctuate, subject to the following expression,

$$E(\vec{\kappa}, a, \{n_k\}) = \sum_{i=1}^{4} \tilde{u}_\alpha(\phi_i) n_i + \sum_{i=1}^{3} \sum_{j>i}^{4} \left[\tilde{v}_{\alpha\gamma}(\psi_{ij}) - \lambda_{\alpha\gamma}(a_i, a_j, \psi_{ij})\right] n_i n_j, \tag{3.19}$$

where ϕ_i denotes the angle of deviation of $\mathbf{b}_i$ from its ideal tetrahedral orientation and ψ_{ij} is the angle between $\mathbf{b}_i$ and $\mathbf{b}_j$ (see Fig. 3.5(a)). In this expression the direct hydrogen bond energy, $\tilde{u}_\alpha(\phi)$, is described separately for donor and acceptor bonds, as denoted by the subscript α. Similarly, the effects of three-body interactions are described by $\tilde{v}_{\alpha\gamma}(\psi)$, which depends on the directionality of the bonds involved in ψ, denoted by α and γ. The function $\lambda_{\alpha\gamma}(a_i, a_j, \psi_{ij})$ is designed to attenuate the effects of three-body interactions based on the availability of broken hydrogen bonds at a_i or a_j. Here, we assign $\tilde{u}_\alpha$ and $\tilde{v}_{\alpha\gamma}$ to reflect the atomistic simulation data plotted in Fig. 3.5(c) and Fig. 3.5(d), respectively. We refer to this variation of our model as the *three-body fluctuation model*. The details about implementing this model variation are described in the following subsection.

The three-body fluctuation model exhibits interface-specific non-ideal hydrogen bond structure that is similar to that observed in atomistic simulation. As the inset of Fig. 3.6(a) illustrates, this includes an interfacial enhancement of donor-donor and acceptor-acceptor angles of $\psi < 60$ deg, similar to that observed in atomistic simulation. We find that including the effects of three-body hydrogen bond defects significantly improves the ability of the model to accurately describe interfacial polarization and polarizability, as illustrated in Fig. 3.7. These effects do not, however, completely account for the interfacial variations in $\langle(\delta\mu_{\hat{\mathbf{n}}}(a))^2\rangle$, which suggests that interfacial polarizability also includes contributions from other microscopic effects, such as higher-order many-body effects.

3.4.1 Details of the Model Implementation

Following the notations used in the previous section, let $\{\hat{\mathbf{v}}_1, \hat{\mathbf{v}}_2, \hat{\mathbf{v}}_3, \hat{\mathbf{v}}_4\}$ be the unit vectors of ideal hydrogen bonding directions through the hydrogens and lone pairs of a probe water molecule of given orientation $\vec{\kappa}$. We sample the hydrogen bond

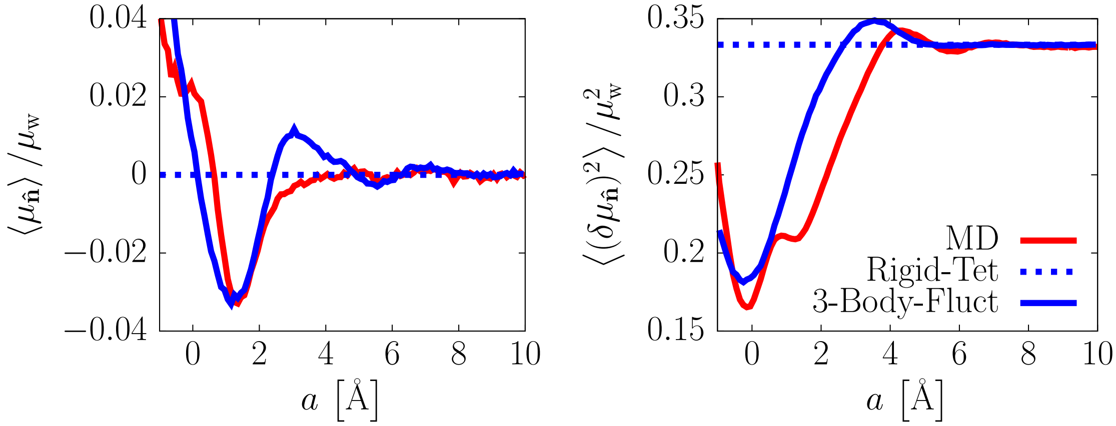

Figure 3.7 Interfacial mean dipole orientation, $\langle\mu_{\hat{\mathbf{n}}}(a)\rangle$, and dipole fluctuations, $\langle(\delta\mu_{\hat{\mathbf{n}}}(a))^2\rangle$, computed from the atomistic simulation and different variations of our mean field model. Solid red lines (MD) correspond to atomistic simulation data. Dashed (Rigid-Tet) and solid (3-Body-Fluct) blue lines correspond to the rigid tetrahedral model and the three-body fluctuation model, respectively.

vectors, $\{\mathbf{b}_1, \mathbf{b}_2, \mathbf{b}_3, \mathbf{b}_4\}$, each of which is within a certain solid angle around $\hat{\mathbf{v}}_i$ such that $\mathbf{b}_i \cdot \hat{\mathbf{v}}_i = |\mathbf{b}_i| \cos\phi_i$ where the value for $\cos\phi_i$ is drawn from the uniform random distribution of $[\cos 70°, 1]$. Each hydrogen bond vector is assigned a directionality of either donor or acceptor based on the proximity to the bonding sites (see Eq. (3.11)). The six inter-bond angles, ψ_{ij}, are calculated based on Eq. (3.12). If the bond vectors are too close with one another, *i.e.* $\psi_{ij} < 44°$, they are not taken into account for computing $P(\vec{\kappa}|a)$ since there is almost no statistics below that in the atomistic simulation. Hence $P(\vec{\kappa}|a)$ is computed as,

$$P(\vec{\kappa}|a) = \int \prod_{i=1}^{4} \left[d\mathbf{b}_i \delta(|\mathbf{b}_i| - d_{\mathrm{HB}}) H\left(\frac{\mathbf{b}_i}{|\mathbf{b}_i|} \cdot \hat{\mathbf{v}}_i - \cos 70° \right) \right. \\ \left. \times \prod_{j>i} H\left(\cos 44° - \frac{\mathbf{b}_i \cdot \mathbf{b}_j}{|\mathbf{b}_i||\mathbf{b}_j|} \right) \right] \frac{\left\langle e^{-\beta E(\vec{\kappa}, a, \{n_k\})} \right\rangle_{\mathrm{b}}}{Z(a)}, \tag{3.20}$$

where $E(\vec{\kappa}, a, \{n_k\})$ follows the Eq. (3.19). Here we impose the same constraint on the length of hydrogen bond vectors as that in the rigid tetrahedral model. Implementing the fluctuations in $|\mathbf{b}_i|$ provokes more details about the energetics, $\tilde{u}_\alpha$ and $\tilde{v}_{\alpha\gamma}$, such as their dependence on both lengths and angles of the hydrogen bond vectors, which we have not detailed so far in this model.

The energy functions, $\tilde{u}_\alpha(\phi)$ and $\tilde{v}_{\alpha\gamma}(\psi)$, are rescaled from the atomistic simulation data of $u_\alpha(\phi)$ and $v_{\alpha\gamma}(\psi)$. Additionally, we parametrize $\tilde{u}_\alpha(\phi)$ by tuning the maximum value of $u_\alpha(\phi)$ such that

$$\tilde{u}_\alpha(\phi) = \begin{cases} \left[\big(u_\alpha(\phi) - u_\alpha(0)\big) \dfrac{u_\alpha^* - u_\alpha(0)}{u_{\alpha,\max} - u_\alpha(0)} + u_\alpha(0) \right] \dfrac{|\epsilon_{\mathrm{w}}|}{E_{\mathrm{HB}}}, & \text{if } \phi \le \phi_c, \\ 0, & \text{if } \phi > \phi_c, \end{cases} \tag{3.21}$$

where $\phi_c = 72°$, $u_{\alpha,\max} = \max_{\phi<\phi_c}\{u_\alpha(\phi)\}$, and u_α^* is the parameter that sets the new maximum (in the original scale of u_α). Here the factor of $|\epsilon_{\mathrm{w}}|/E_{\mathrm{HB}}$ rescales the functions in units of the effective hydrogen bond energy of our model. We observed that the behavior of $\langle \mu_{\hat{\mathbf{n}}}(a) \rangle$ is largely sensitive to $\tilde{u}_\alpha(\phi)$, and thus we optimized the parameters, u_α^* and ϵ_{w}, for the result expected from atomistic simulations. For the results presented in Fig. 3.7, we used $\epsilon_{\mathrm{w}} = -5.0\, k_B T$, $u_{\mathrm{D}}^* = +0.2\, k_B T$, and $u_{\mathrm{A}}^* = -3.7\, k_B T$. We found that the optimized $\tilde{u}_{\mathrm{A}}(\phi)$ is quite different from $u_{\mathrm{A}}(\phi)$ but more like the corresponding energy computed near the interface (see Fig. 3.8). For $\tilde{v}_{\alpha\gamma}(\psi)$, we simply take the values from the atomistic simulation data and rescale them in units of ϵ_{w}, that is,

$$\tilde{v}_{\alpha\gamma}(\psi) = v_{\alpha\gamma}(\psi) \frac{|\epsilon_{\mathrm{w}}|}{E_{\mathrm{HB}}} \,. \tag{3.22}$$

As given in Eq. (3.19), $\tilde{v}_{\alpha\gamma}(\psi)$ is combined with the auxiliary function, $\lambda(a_i, a_j, \psi_{ij})$, in order to accounts for the interface-specific stability of hydrogen bond defects. This

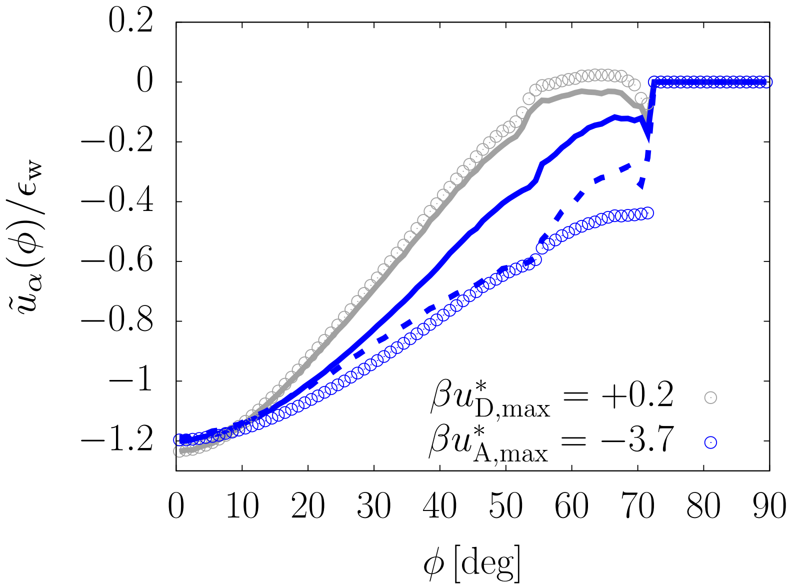

Figure 3.8 $\tilde{u}_\alpha(\phi)$ compared with $u_\alpha(\phi)$ in the same scale. Solid lines are the simulation data of $u_\alpha(\phi)/E_\mathrm{HB}$, as originally shown in Fig. 3.5(c), and circles indicate the rescaled energy functions that are optimized for the accurate trend of $\langle\mu_{\hat{\mathbf{n}}}(a)\rangle$. Gray and blue color correspond to $\alpha = \mathrm{D}$ and $\alpha = \mathrm{A}$, respectively. The blue dashed line corresponds to $u_\mathrm{A}(\phi|a = 1\,\text{Å})$, *i.e.*, the average direct interaction energy for a hydrogen bond pair at $a = 1\,\text{Å}$.

auxiliary function represents the energetic cost for the defects to pay based on the hydrogen bonding status of the ith or jth hydrogen bond partner. Assuming that this penalty is imposed on the one that donates hydrogen, we describe this function in terms of the average number and energy of hydrogen bonds through donor sites, denoted by $N_\mathrm{D}(a)$ and $E_\mathrm{D}(a)$ respectively. Specifically it is given by,

$$\lambda_{\alpha\gamma}(a_i, a_j, \psi) = \begin{cases} \dfrac{N_\mathrm{D}(\bar{a}_{\alpha\gamma})}{2} E_\mathrm{D}(\bar{a}_{\alpha\gamma}) \dfrac{|\epsilon_\mathrm{w}|}{E_\mathrm{HB}}, & \text{if } \psi \le \psi_{\alpha\gamma}, \\ \left[1 - \dfrac{v_{\alpha\gamma}(\psi) - v_{\alpha\gamma}(\psi_{\alpha\gamma})}{v_{\alpha\gamma}(\psi_c) - v_{\alpha\gamma}(\psi_{\alpha\gamma})}\right] \lambda_{\alpha\gamma}(a_i, a_j, \psi_{\alpha\gamma}), & \text{if } \psi_{\alpha\gamma} < \psi < \psi_c, \\ 0, & \text{if } \psi \ge \psi_c, \end{cases} \tag{3.23}$$

where $\psi_{\alpha\gamma} = \arg\min_\psi \{v_{\alpha\gamma}(\psi)\}$, $\psi_c = \arg\max_\psi \{v_\mathrm{AA}(\psi)\}$, and

$$\bar{a}_{\alpha\gamma}(a_i, a_j) = \begin{cases} \min\{a_i, a_j\}, & \text{if } \alpha = \gamma, \\ \Phi_\mathrm{D}(y_i)\, a_i + \Phi_\mathrm{D}(y_j)\, a_j, & \text{if } \alpha \ne \gamma. \end{cases} \tag{3.24}$$

Here we let the penalty taken by the hydrogen bond partner located closer to the interface, but we make the exception for donor-acceptor bond pairs based on the typical structure of cyclic water trimer [85]. $N_\mathrm{D}(a)$ and $E_\mathrm{D}(a)$ are computed from

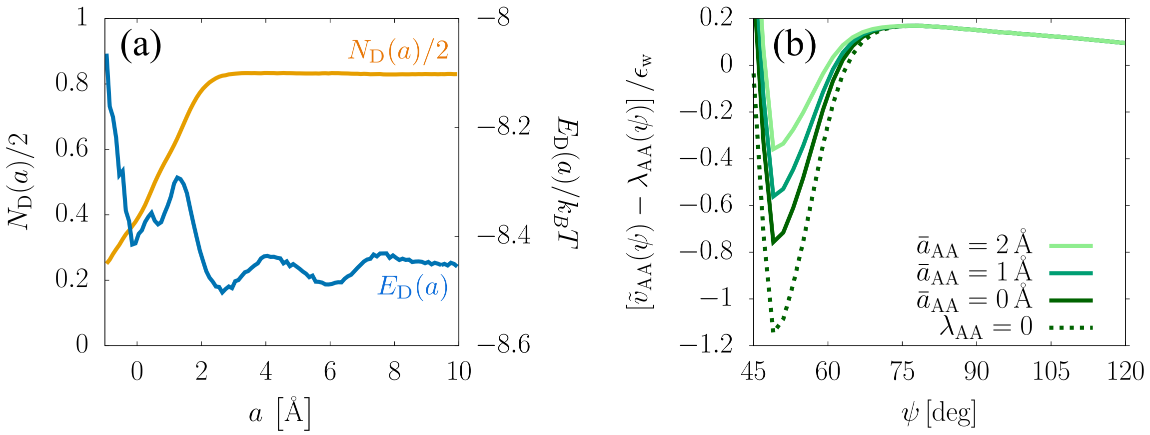

Figure 3.9 (a) Interfacial profiles of average number and energy of hydrogen bonds through donor sites, rendered in orange and blue lines respectively. (b) Illustration of a three-body interaction term implemented in our model. Solid lines show the different energetic preferences for highly distorted configurations depending on the interfacial depth of hydrogen bond partner. Dashed line corresponds to $\tilde{v}_{\rm AA}$ without the attenuation by $\lambda_{\rm AA}$.

atomistic simulation as,

$$N_{\rm D}(a) = \frac{\left\langle \sum_i \sum_{j\neq i} \delta(a^{(i)} - a) H\left(30^\circ - \phi_j^{(i)}\right) H\left(3.5\,\text{Å} - \left|\mathbf{b}_j^{(i)}\right|\right) \Phi_{\rm D}\left(y_j^{(i)}\right) \right\rangle}{\left\langle \sum_i \delta\left(a^{(i)} - a\right) \right\rangle}, \quad (3.25)$$

and

$$E_{\rm D}(a) = \frac{\left\langle \sum_i \sum_{j\neq i} U_{ij}\, \delta(a^{(i)} - a) H\left(30^\circ - \phi_j^{(i)}\right) H\left(3.5\,\text{Å} - \left|\mathbf{b}_j^{(i)}\right|\right) \Phi_{\rm D}\left(y_j^{(i)}\right) \right\rangle}{\left\langle \sum_i \sum_{j\neq i} \delta(a^{(i)} - a) H\left(30^\circ - \phi_j^{(i)}\right) H\left(3.5\,\text{Å} - \left|\mathbf{b}_j^{(i)}\right|\right) \Phi_{\rm D}\left(y_j^{(i)}\right) \right\rangle}, \quad (3.26)$$

where the definition of a good hydrogen bond follows the one by Luzar and Chandler [86]. As illustrated in Fig. 3.9, they change dramatically within the first 2 Å of the interfacial region such that the effect of three-body interaction also becomes significant in that region. Here we take the value of $E_{\rm HB}$ from $E_{\rm D}(a)$ by setting $E_{\rm HB} = |E_{\rm D}(a_b)| = 8.45\,k_BT = 20.9\,\text{kJ/mol}$ at $T = 298$ K.

In order to evaluate $P(\vec{\kappa}|a)$, we obtain an approximate analytic expression for $\left\langle e^{-\beta E(\vec{\kappa},a,\{n_k\})} \right\rangle_{\rm b}$ in Eq. (5.9). Here we made the same assumption as that of the rigid tetrahedral model, such that $\langle n_i n_j \rangle \approx \langle n_i \rangle \langle n_j \rangle$ for $i \neq j$.[3] Within this approximation,

---

[3] This is definitely a rough approximation since it neglects the density correlation between hydrogen bond partners even in the squeezed configurations. However, more accurate treatment for the density correlation provokes again the distance dependence of the energy functions which we have not detailed so far in this model.

we can write

$$\begin{aligned}\left\langle e^{-\beta E(\vec{\kappa},a,\{n_k\})}\right\rangle_{\rm b} &= \prod_{i=1}^{4}\langle n_i\rangle_{\rm b} e^{-\beta\tilde{u}_\alpha(\phi_i)}\prod_{j>i}^{4} e^{-\beta\tilde{v}_{\alpha\gamma}(\psi_{ij})} \\ &+\sum_{k=1}^{4}\left[1-\langle n_k\rangle_{\rm b}\right]\prod_{i\neq k}^{4}\langle n_i\rangle_{\rm b} e^{-\beta\tilde{u}_\alpha(\phi_i)}\prod_{j\neq k>i}^{4} e^{-\beta\tilde{v}_{\alpha\gamma}(\psi_{ij})} \\ &+\sum_{i=1}^{4}\sum_{j>i}^{4}\langle n_i\rangle_{\rm b}\langle n_j\rangle_{\rm b}\left[1-\langle n_k\rangle_{\rm b}\right]\left[1-\langle n_l\rangle_{\rm b}\right] e^{-\beta[\tilde{u}_\alpha(\phi_i)+\tilde{u}_\alpha(\phi_j)+\tilde{v}_{\alpha\gamma}(\psi_{ij})]} \\ &+\sum_{k=1}^{4}\langle n_k\rangle_{\rm b} e^{-\beta\tilde{u}_\alpha(\phi_k)}\prod_{i\neq k}^{4}\left[1-\langle n_i\rangle_{\rm b}\right]+\prod_{i=1}^{4}\left[1-\langle n_i\rangle_{\rm b}\right] \ , \end{aligned} \tag{3.27}$$

where $\langle n_i\rangle_{\rm b} = P_{\rm HB}(a_i) = \rho(a_i)/2\rho_b$ and the dummy indices, k and l, in the third term are the numbers among $\{1,2,3,4\}$ such that $i \neq j \neq k \neq l$. The resulting reduced probability distribution, $P(\cos\theta_{\rm OH}|a)$, is given in Fig. 3.10, where the cosines are computed as $\cos\theta_i = \hat{\mathbf{v}}_i \cdot \hat{\mathbf{n}}$. Although its qualitative feature is still the same as the result from the rigid tetrahedral model, its details are closer to that from the atomistic simulation of TIP5P water (especially at $a < 3$ Å).

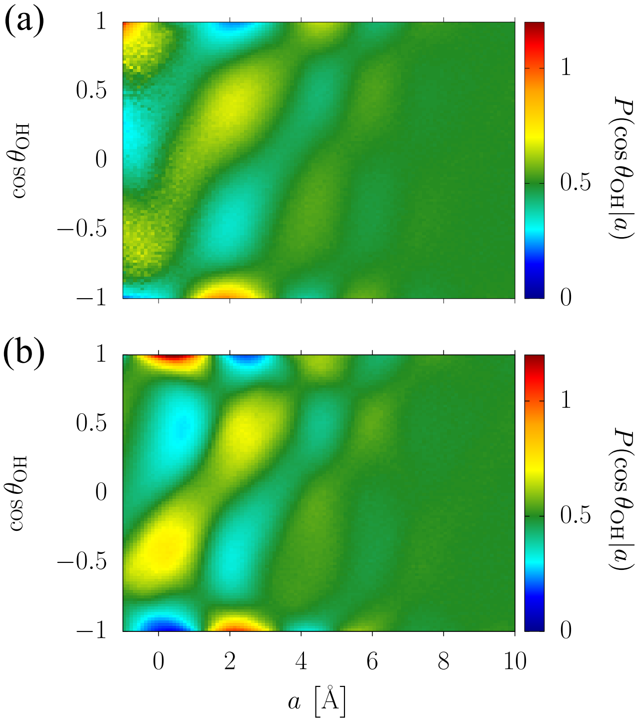

Figure 3.10 Orientational distributions, $P(\cos\theta_{\rm OH}|a)$, computed from (a) the three-body fluctuation model and (b) the rigid tetrahedral model for the TIP5P force field. Color shading indicates the probability density.

3.4.2 Application of the Mean-Field Model to the SPC/E Force Field

The characteristics of interfacial molecular structure as derived from molecular dynamics simulations depend somewhat on the identity of the water force field. Despite sharing similar bulk hydrogen bonding structures, different classical water models can yield non-trivial differences in interfacial structure. Some of these differences are highlighted in Figs. 2.3 and 2.4. We observe that different force fields exhibit similar trends in dipolar polarization and polarizability, but that they vary in their quantitative characteristics. To evaluate the ability of our mean field model to capture these differences we also apply the model to the SPC/E force field. Specifically we follow the same procedure described in the previous subsection except for using the data from molecular dynamics simulations of the SPC/E water rather than the TIP5P. For the SPC/E-parameterized mean field model, we find similarly good agreement in reproducing $P(\cos\theta_{\mathrm{OH}}|a)$ as illustrated in Fig. 3.11, but as Fig. 3.12 illustrates, the agreement to $\langle\mu_{\hat{\mathbf{n}}}(a)\rangle$ and $\langle(\delta\mu_{\hat{\mathbf{n}}}(a))^2\rangle$, is not so good for SPC/E as for TIP5P.

We understand that the difference in the ability of our model to reproduce dipolar polarization/polarizability between SPC/E and TIP5P arises due to the differences in the geometric tendencies inherent to these force fields. The TIP5P force field is built upon a tetrahedral charge scaffold, so non-ideal hydrogen bond structures are more naturally described in terms of their deviations from this scaffold. On the other

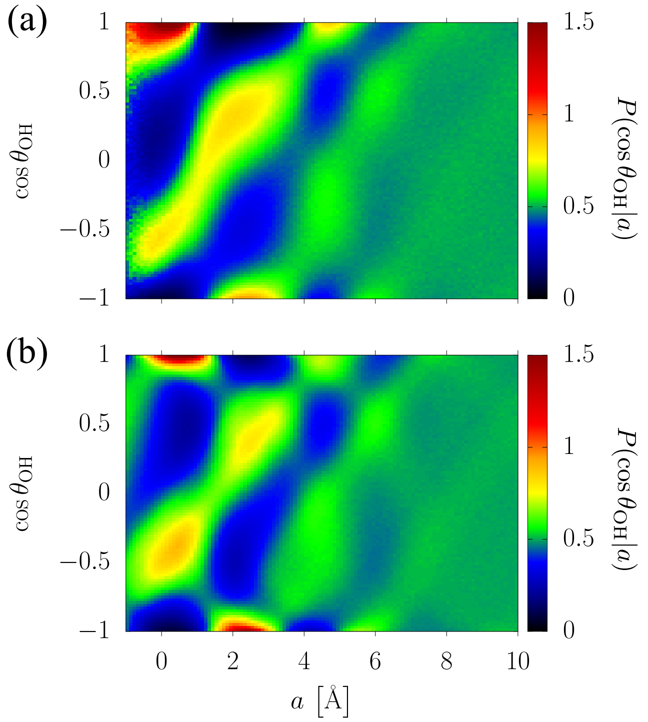

Figure 3.11 $P(\cos\theta_{\mathrm{OH}}|a)$ computed from (a) the atomistic simulation with SPC/E water and (b) the rigid tetrahedral model optimized for the SPC/E force field ($\epsilon_{\mathrm{w}}^{*} = -1.8\, k_B T = -4.46$ kJ/mol).

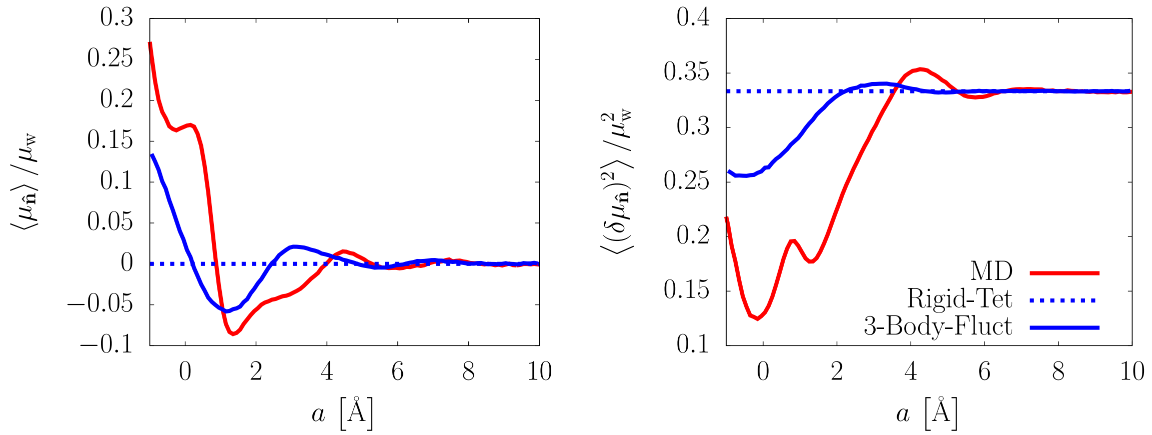

Figure 3.12 Interfacial polarization, $\langle\mu_{\hat{\mathbf{n}}}(a)\rangle$, and polarizability, $\langle(\delta\mu_{\hat{\mathbf{n}}}(a))^2\rangle$, computed from the three-body fluctuation model parametrized for the SPC/E force field (blue solid lines), in comparison to the MD simulation results (red lines).

hand, SPC/E is built upon a triangular charge scaffold (albeit with a tetrahedral bond angle) so non-ideal hydrogen bond structures are less well represented in term of deviation from a tetrahedral scaffold. These differences in model geometry influence molecular correlations in the interfacial region [87]. This influence is illustrated to some extent in Fig. 3.13. To accurately capture this influence in our model would require modifying the geometric framework that is built upon in order to reflect that of the atomistic force field.

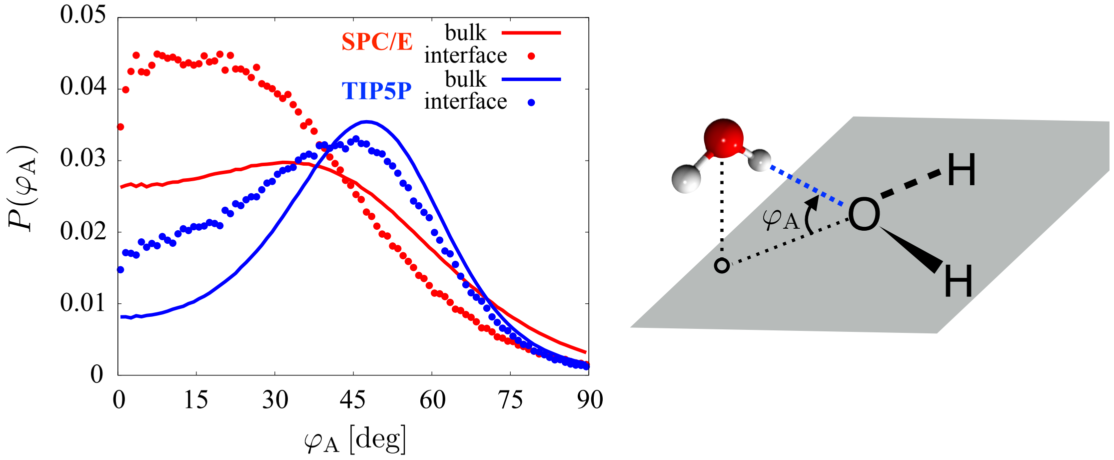

Figure 3.13 Probability distributions of φ_{A} computed from the simulations of the SPC/E and TIP5P force fields, shown in red and blue colors respectively. As illustrated on the right, φ_{A} is the angle of the bond vector accepting a hydrogen relative to the plane including the probe molecule. Here the probability distributions for the SPC/E and TIP5P force fields exhibit quite different trends even in the bulk. φ_{A} is mostly probable around 50° for the TIP5P, whereas there are significant populations near $\varphi_{\mathrm{A}} = 0°$ for the SPC/E. This difference, which becomes more pronounced at the interface, reflects the distinct geometric characteristics of the charge scaffolds of the two water force fields.

3.5 Conclusion

To conclude, we summarize two fundamental aspects of interfacial molecular structure that have been revealed by our mean field model of the liquid water-vapor interface. First, we observed that the depth dependent variations in molecular orientations at the interface are determined by the molecular geometry of hydrogen bonding and how it conforms to the anisotropic features of the interfacial density field. We demonstrated that ideal bulk- like hydrogen bond geometry was sufficient to explain most of the interfacial variations in molecular orientations. Second, our model revealed that interfacial variations in molecular orientational polarization and polarizability arise due to distorted non-tetrahedral hydrogen bond structures. We showed that the interface features squeezed triangular hydrogen bond defects that contribute significantly to determining interfacial dielectric properties.

Chapter 4

Characterizing Hydration Properties Based on the Orientational Structure of Interfacial Water Molecules

In this chapter,[1] we present a general computational method for characterizing the molecular structure of liquid water interfaces as sampled from atomistic simulations. With this method, the interfacial structure is quantified based on the statistical analysis of the orientational configurations of interfacial water molecules. The method can be applied to generate position dependent maps of the hydration properties of heterogeneous surfaces. We present an application to the characterization of surface hydrophobicity, which we use to analyze simulations of a hydrated protein. We demonstrate that this approach is capable of revealing microscopic details of the collective dynamics of a protein hydration shell.

4.1 Introduction

In the vicinity of a hydrated surface the properties of water can differ significantly from those of the bulk liquid [27]. These differences are determined by the details of the interfacial environment and they are thus sensitive to the specific chemical and topological features of the hydrated surface [88]. The details of water's interfacial molecular structure, therefore, contain information about these surface features and how they affect their local aqueous environment [28]. This information is valuable because it provides insight into the collective molecular effects that control the solvation properties of complex solutes, but it is also difficult to access due to limitations in our ability to measure and characterize water's interfacial molecular structure.

Our current understanding of the interfacial molecular structure of liquid water is derived primarily from the results of interface sensitive experimental techniques such as vibrational sum frequency generation spectroscopy [89–93], THz absorption spectroscopy [94, 95], dynamic nuclear polarization [96], NMR [97, 98], and X-ray

---

[1] This chapter borrows largely from the previously published work, *J. Chem. Theory Comput.* **14**, 461–465 (2018).

and neutron scattering [99–101]. Unfortunately, these experiments are typically more difficult to interpret than their bulk phase counterparts due to the constraints associated with achieving interface selectivity. This has driven an increased demand for theoretical developments that can facilitate the analysis and interpretation of these interface-sensitive experiments. Resulting efforts have relied heavily on the use of atomistic simulation to provide the molecular details of water's interfacial structure.

Classical molecular dynamics (MD) simulations are a particularly efficient theoretical framework for modeling the microscopic properties of aqueous interfacial systems. These simulations provide a molecular-level basis for understanding the microscopic structure of liquid water and how it responds to the anisotropic environment of the liquid phase boundary. This response is mediated by the properties of water's hydrogen bonding network and therefore involves the correlated arrangements of many individual water molecules. Characterizing this high-dimensional molecular structure in simple and intuitive terms can be a significant challenge, especially for solutes such as proteins that exhibit irregular or heterogeneous surface properties.

Here we address this challenge by characterizing water's interfacial molecular structure in terms of a low dimensional parameter that quantifies its similarity to the structure of various interfacial reference systems. We introduce a theoretical framework for quantifying this similarity based on the statistical analysis of molecular orientations at the interface. In this analysis, reference systems serve to designate the unique orientational signatures of water interfaces at surfaces with specific well-defined chemical or topographical properties. The properties of these reference surfaces can be systematically chosen in order to analyze specific interfacial features that may be relevant to a particular system of study. This framework provides a physically insightful measure of interfacial structure that eliminates the need to formulate high-dimensional collective variables. Furthermore, by applying this framework across a variety of different reference systems, it can be adapted to report simultaneously on multiple specific interfacial properties.

4.2 The Theoretical Framework

4.2.1 Formalism

The general formalism for our framework begins with the definition of the reference system(s) that will serve as a basis for interfacial characterization. Prior to applying this framework, each reference system must be thoroughly sampled in order to establish its unique orientational molecular signature. We quantify this signature in terms of the molecular orientational distribution function,

$$f(\vec{\gamma}|\mathrm{ref}) = -\ln\left[\frac{P(\vec{\gamma}|\mathrm{ref})}{P(\vec{\gamma}|\mathrm{iso})}\right] , \tag{4.1}$$

where $P(\vec{\gamma}|\mathrm{ref})$ denotes the equilibrium probability for observing a molecule with a specific molecular configuration, $\vec{\gamma}$, within the given reference system, and $P(\vec{\gamma}|\mathrm{iso})$ is the probability for $\vec{\gamma}$ when molecular orientations have an isotropic distribution.

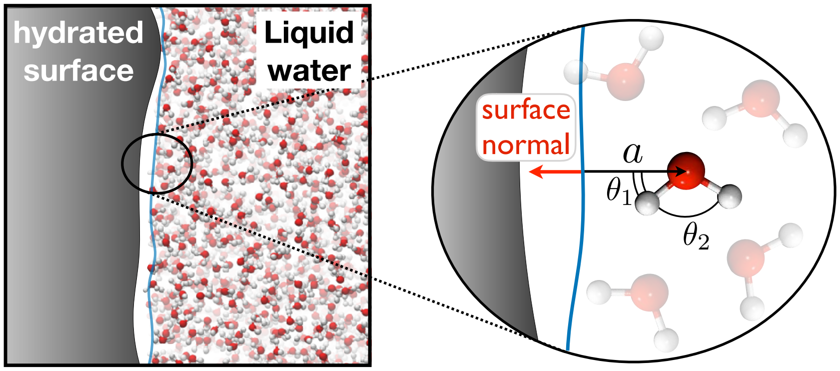

Figure 4.1 Schematic illustration of the molecular coordinates that are used to specify the orientational state, $\vec{\gamma}$, of molecules at the liquid water interface.

Defined in this way, $f(\vec{\gamma}|\text{ref})$ specifies the relative free energy, in units of k_BT, associated with the orientational anisotropy of the interfacial reference system. We specify molecular configuration in terms of a three-dimensional vector, $\vec{\gamma} = (\cos\theta_1, \cos\theta_2, a)$, where θ_1 and θ_2 denote the angles made between the local surface normal and each of a water molecule's OH bond vectors, and a denotes the distance of the water molecule from the instantaneous position of the water interface. We define the instantaneous water interface following the procedure given in Sec. 2.1. This system of molecular coordinates is illustrated schematically in Fig. 4.1.

We characterize the interfacial molecular structure of of a particular interfacial system by sampling values of $\vec{\gamma}$ and comparing them to the distribution function, $f(\vec{\gamma}|\text{ref})$. Specifically, we compute the quantity,

$$\lambda_{\text{ref}} = \frac{1}{N}\sum_{i=1}^{N} f(\vec{\gamma}|\text{ref}) \ , \tag{4.2}$$

where the summation is taken over a set of N molecular configurations sampled from the system of interest. This quantity reflects the likelihood for the sampled set of configurations to occur spontaneously within the environment of the reference system. This likelihood is relatively large (corresponding to lower values of λ_{ref}) when interfacial molecular structure is similar to that of the reference system and relatively small (corresponding to higher values of λ_{ref}) when interfacial molecular structure differs from that of the reference system. In this way, λ_{ref} can be used to distinguish hydrated surfaces based on how they influence their hydration environments, irrespective of their specific chemical or topographical properties.

The general expression in Eq. (4.2) can be adapted to serve various purposes. For instance, if the summation in Eq. (4.2) is defined to include an ensemble of interfacial molecules sampled over many positions and across many independent snapshots, then the resulting value of λ_{ref} can be used to characterize the average properties of the interface. For heterogeneous surfaces, the summation in Eq. (4.2) can be defined in such a way as to generate spatially resolved maps of λ_{ref}. To accomplish this, we adapt Eq. (4.2) so that it can be applied to compute λ_{ref} at a specific position along the surface, $\mathbf{r}_{\text{surf}}$, and point in time, t. Specifically, we utilize the expression,

$$\lambda_{\text{ref}}(\mathbf{r}_{\text{surf}}, t) = \frac{1}{N_\tau} \sum_{t'=t}^{t+\tau} f(\vec{\gamma}(\mathbf{r}_{\text{surf}}, t')|\text{ref}) \ , \tag{4.3}$$

where $\vec{\gamma}(\mathbf{r}_{\text{surf}}, t')$ is the orientational configuration of the water molecule that is closest to position $\mathbf{r}_{\text{surf}}$ at time t' and the summation is taken over a series of N_τ discrete time steps along the interval τ. In practice we evaluate $\lambda_{\text{ref}}(\mathbf{r}_{\text{surf}}, t; \tau)$ separately for a discrete set of positions located on the two-dimensional manifold of the hydrated surface. For a planar surface these points lie on the vertices of a square lattice with lattice spacing that can be varied arbitrarily to achieve any desired spatial resolution.

Since we define $\vec{\gamma}(\mathbf{r}_{\text{surf}}, t')$ to include only the single nearest water molecule (see Sec. 4.3.2 for more details), the number of sampled configurations for each surface point is equal to the number of snapshots evaluated in the time interval τ. For a given position along the surface, the set of molecular configurations that are averaged over to compute $\lambda_{\text{ref}}(\mathbf{r}_{\text{surf}}, t; \tau)$ thus include a variety of different orientations and values of a. We find that approximately 10^2 individual snapshots (*e.g.*, about 20 ps of simulation data) are required to distinguish between hydrophobic and hydrophilic regions of a surface and approximately 10^3 snapshots (*e.g.*, about 0.2 ns of simulation data) are required to converge a spatial map of $\lambda_{\text{ref}}(\mathbf{r}_{\text{surf}}, t; \tau)$ of a static hydrated surface. The value of τ in Eq. (4.3) can be varied to highlight average interfacial response to a heterogeneous surface (*i.e.*, large τ) or to highlight transient fluctuations in interfacial molecular structure (*i.e.*, small τ).

4.2.2 Reference System for Characterizing Hydrophobicity

Early approaches to mapping the hydration properties of heterogeneous solutes, most notably those developed by Kyte and Doolittle, were based on a spatial decomposition of surface chemistry [102], and have since been extended to provide higher resolution [103]. These approaches often fail to accurately predict solvation properties due to their neglect of transverse correlations within the water interface. More recent approaches have focused on water-based mapping methods. This includes approaches based on local density fluctuations [104, 105], single water chemical potentials [106], and local electrostatic fields [107]. Our method is complementary to these previous approaches and can be adapted, via the selection of different reference systems, to map a wide variety of interfacial properties.

We illustrate the performance of our method by applying it to characterize the hydrophobicity of heterogeneous surfaces. To do this we use a single reference system as a basis for interfacial characterization—the liquid water interface at an ideal hydrophobic surface. We represent this reference system using the intrinsic molecular structure of a liquid water–vapor interface, which has been shown to reflect the microscopic characteristics of an ideal hydrophobic surface [51]. The collective molecular arrangements that are common to this reference system are thus specified by $f(\vec{\gamma}|\text{phob})$. As we demonstrate in the following section, λ_{phob} is capable of distinguishing between the interfacial molecular structure of hydrophobic and hydrophilic surfaces and can thus be treated as an order parameter for hydrophobicity. As such, we use λ_{phob}, computed according to Eq. (4.3), to analyze water's interfacial response to heterogeneous surfaces. Since λ_{phob} is based only on water's interfacial molecular structure, it can be used to generate hydrophobicity maps that reveal the effective solvation characteristics of surfaces with complex or unknown properties.

To quantify $f(\vec{\gamma}|\mathrm{phob})$, we utilize pre-tabulated values of $P(\vec{\gamma}|\mathrm{phob})$ that are analyzed from the instantaneous liquid–vapor interface [34]. Specifically, $P(\vec{\gamma}|\mathrm{phob})$ was computed from a MD simulation of a slab of 4913 SPC/E water molecules [35] in a simulation cell measuring approximately $6 \times 6 \times 10\ \mathrm{nm}^3$. At 298 K, this simulation spontaneously forms a free liquid–vapor interface, which serves to buffer the pressure of the liquid region of the slab. Other simulation details are the same as those given in Sec. 2.2. $P(\vec{\gamma}|\mathrm{iso})$ was computed from the random sampling of orientational configurations based on molecular rotations. Figure 4.2 shows the value of $\exp[-f(\vec{\gamma}|\mathrm{phob})] = P(\vec{\gamma}|\mathrm{phob})/P(\vec{\gamma}|\mathrm{iso})$ for several different values of a, *i.e.*, the molecular distance from the instantaneous liquid interface.

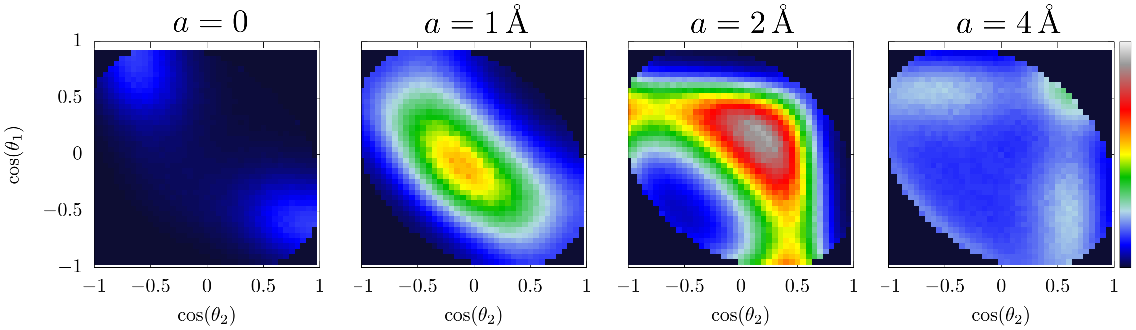

Figure 4.2 Plots showing the value of $\exp[-f(\vec{\gamma}|\mathrm{phob})] = P(\vec{\gamma}|\mathrm{phob})/P(\vec{\gamma}|\mathrm{iso})$, as indicated by shading. Each plot is scaled to the same color bar as given on the right.

4.3 Application to Model Surfaces

4.3.1 Results and Discussions

As a proof of concept, we apply our framework for interfacial characterization to a model silica surface with a patterned composition of hydrophobic and hydrophilic surface sites [108]. As illustrated in Fig. 4.3, the surface sites of this model can be either nonpolar (*i.e.*, hydrophobic), if they are terminated with a neutral silicon atom, or polar (*i.e.*, hydrophilic), if they are terminated with a charged hydroxyl group. Artificial surfaces with well-defined surface patterns can be created by specifying the hydroxylation state of the surface sites. We then use λ_{phob} to analyze water's response to various surface patterns. We quantify this response by computing $\delta\lambda_{\mathrm{ref}} = \lambda_{\mathrm{ref}} - \langle\lambda_{\mathrm{ref}}\rangle_0$, where $\langle\cdots\rangle_0$ denotes an equilibrium average taken within the ensemble of configurations sampled directly from the reference system. In this way, values of $\delta\lambda_{\mathrm{ref}} \approx 0$ correspond to interfacial environments that resemble those of the

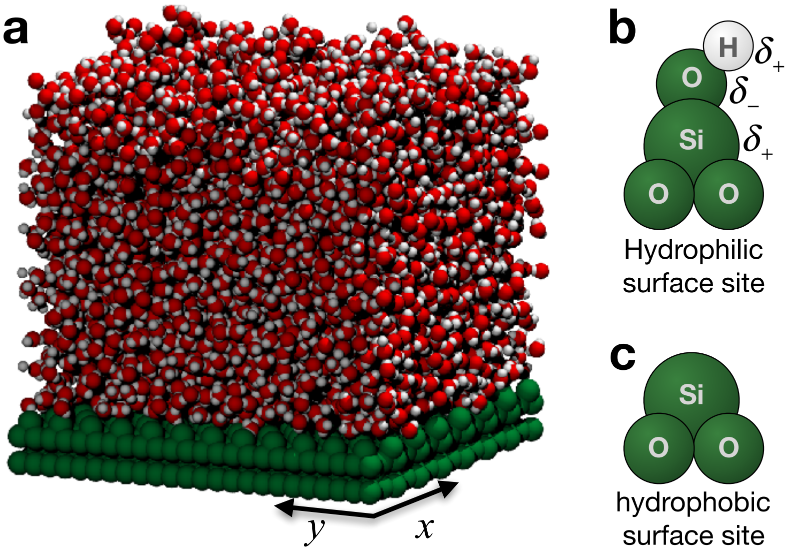

Figure 4.3 (a) Snapshot of a simulation of a periodically replicated slab of liquid water in contact with a 6×6 nm^2 model silica surface. (b and c) Chemical termination of the surface sites that determines whether they are hydrophilic or hydrophobic, respectively.

reference system. Further details about the simulations are described in the following subsection.

Figure 4.4 highlights the ability of λ_{phob} to distinguish between water's interfacial molecular response to hydrophobic and hydrophilic regions of a spatially heterogeneous surface. Specifically, we have computed λ_{phob}, using Eq. (4.3), for points along an extended hydrophobic surface with a larger rectangular hydrophilic patch, as shown in Fig. 4.4(a). For the data plotted in Fig. 4.4(b), λ_{phob} has been averaged over a long observation time of $\tau = 4$ ns (20000 individual configurations). We observe that water's average interfacial molecular structure exhibits spatial variations that mimic the chemical patterning of the underlying silica surface. Over nonpolar regions of the surface $\delta\lambda_{\text{phob}} \approx 0$ (*i.e.*, $\lambda_{\text{phob}} \approx \langle\lambda_{\text{phob}}\rangle_0$), indicating that interfacial molecular structure is similar to that of the hydrophobic reference system. Over polar regions of the surface $\delta\lambda_{\text{phob}} > 0$ (*i.e.*, $\lambda_{\text{phob}} > \langle\lambda_{\text{phob}}\rangle_0$), indicating that water's interfacial response differs significantly from that of the reference system. Low-amplitude spatial modulations in λ_{phob} can be observed over both the polar and the nonpolar regions of the surface. These modulations reflect the corrugation of the atomic surface and thus indicate that this order parameter is sensitive to the subtle influence of surface topography on water's interfacial molecular structure.

Transient fluctuations in local interfacial structure can be analyzed by computing $\delta\lambda_{\text{phob}}$ with a smaller value of τ. For instance, Fig. 4.4(d) shows $\delta\lambda_{\text{phob}}$ computed for the surface in Fig. 4.4(a) using a value of $\tau = 20$ ps (100 individual configurations). The use of a shorter observation time highlights the transient details of water's interfacial molecular structure. Thus, by comparing local values of $\delta\lambda_{\text{phob}}$ over multiple consecutive snapshots it is possible to observe the transient fluctuations of interfacial molecular structure and investigate how they depend on the details of local surface

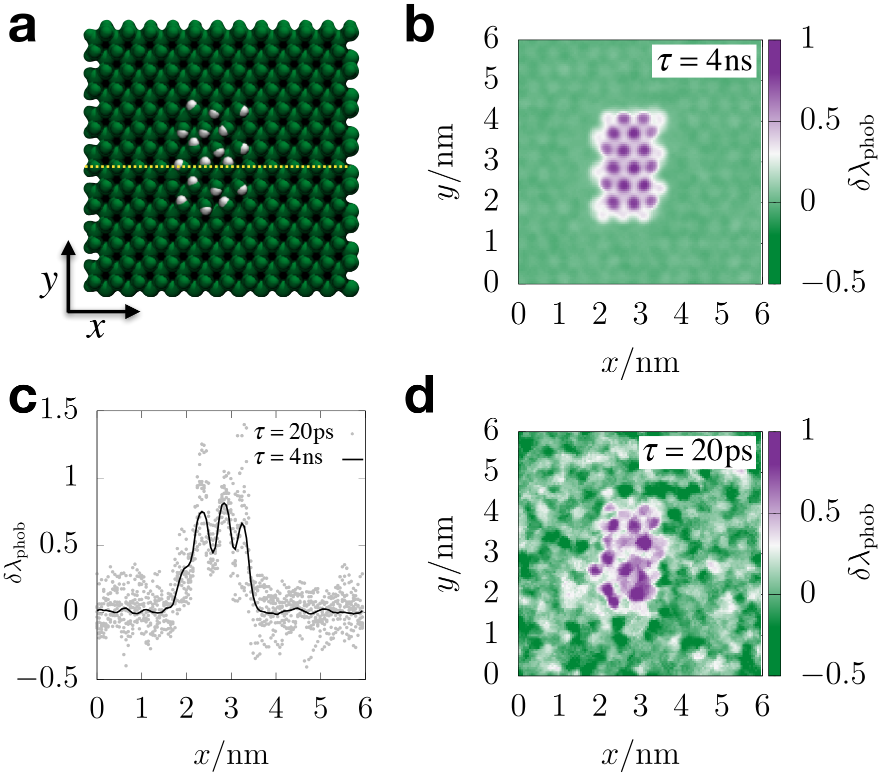

Figure 4.4 (a) Snapshot of the water exposed face of a model silica surface featuring a hydrophilic patch against a hydrophobic background. (b and d) Plot of $\delta\lambda_{\mathrm{phob}}$, indicated by shading, computed for points along the surface of the structure shown in Panel (a). The data in Panels (b) and (d) reflect averages over observation times of $\tau = 4$ ns and $\tau = 20$ ps, respectively. (c) Plot of the values of $\delta\lambda_{\mathrm{phob}}$ computed along a line at $y = 3$ nm (the yellow dotted line in Panel (a)) that highlights how interfacial molecular structure is affected by the patch boundary. Grey points are values of $\delta\lambda_{\mathrm{phob}}$, computed with $\tau = 20$ ps, sampled at different points in time and the solid line is $\delta\lambda_{\mathrm{phob}}$ computed with $\tau = 4$ ns.

chemistry and topology. The dynamic range of $\delta\lambda_{\mathrm{phob}}$ within the hydrophobic reference system is described in the following subsection.

Water molecules that reside over the boundaries between polar and nonpolar regions of the surface experience a laterally anisotropic aqueous environment. In these regions, such as along the edge of the polar patch of the surface illustrated in Fig. 4.4(a), $\delta\lambda_{\mathrm{phob}}$ takes on values that are intermediate between that of the extended polar and nonpolar surfaces. The characteristics of $\delta\lambda_{\mathrm{phob}}$ in these boundary regions reveal details about the molecular correlations that mediate interactions along liquid water interfaces, and how these correlations are influenced by the details of surface-water interactions.

In the case of the model silica surface, we observe that the effect of the polar/nonpolar surface boundary on the interfacial molecular structure is local, limited to the region directly above the surface boundary. A cross section of $\delta\lambda_{\mathrm{phob}}$ that cuts through the center of the hydrophilic surface patch is plotted in Fig. 4.4(c). This plot reveals that the influence of a large hydrophilic surface patch on water's interfacial molecular structure only extends about one molecular diameter beyond the edge of the patch. The observation that water's interfacial molecular structure exhibits a very narrow boundary between hydrophobic and hydrophilic surface domains is somewhat surprising given the strong orientational correlations that are present in liquid water [31, 32]. We expect that this near absence of surface-induced transverse correlations is not a universal feature of liquid water interfaces. Rather, we hypothesize that the specific water configurations that arise over hydroxylated surface sites tend to orient in such a way as to be commensurate with the hydrogen bonding structure of a hydrophobic interface. This would minimize strain in the interfacial hydrogen bonding network that would otherwise lead to extended lateral correlations. We anticipate that different hydrophilic surface chemistries likely exhibit a range of variations in the type of lateral interfacial correlations that they support.

We also carried out simulations on model silica surfaces with a variety of different surface patterns. These patterns are illustrated in Fig. 4.5 along with corresponding maps of $\delta\lambda_{\mathrm{phob}}$ computed for $\tau = 20$ ps and $\tau = 4$ ns. We found that each spatial map shows the microscopic features consistent with what we discussed above. Note that there are lots of fluctuations toward the hydrophobic interfacial structures even over the polar regions of the extended hydrophilic surfaces at the bottom panel. These fluctuations are more vivid than those toward the hydrophilic interfacial structures over the extended hydrophobic surfaces. We speculate that this may imply the preference of water's collective arrangements at interfaces, which is revisited in Chap. 5 for the hydration of a disordered hydrophilic surface.

4.3.2 Computational Details

Simulations consisted of a slab of 4913 water molecules, modeled with the SPC/E force field, in a periodically replicated cell with x, y, and z dimensions of 5.932 nm, 5.982 nm, and 10.00 nm respectively. At the lower z boundary of the simulation cell is a model silica substrate. The details of the substrate and its interactions with SPC/E water molecules is described in Ref. 108. Simulations were carried out using LAMMPS [37] with a NVT ensemble, and $T = 298$ K, enforced via a Langevin thermostat. From an equilibrium trajectory, configurations were sampled every 0.2 ps for computing $\delta\lambda_{\mathrm{phob}}$. The volume of the liquid water slab is much less than that of the simulation cell. This results in the formation of a liquid–vapor like phase boundary that serves to effectively buffer the pressure of the liquid slab.

Surface maps of $\delta\lambda_{\mathrm{phob}}$ were generated via the following procedure. The surface was divided into a square lattice of surface points. The lattice spacing for this division is arbitrary. Following Eq. (4.3), we computed $\delta\lambda_{\mathrm{phob}}$ by assigning exactly one water molecule to each surface point for every output simulation snapshot (each water molecule can be assigned to multiple surface points). This ensures that $\delta\lambda_{\mathrm{phob}}$ for each surface point is averaged over an identical number of molecular configurations, $\vec{\gamma}$. In particular, we project the silhouette of each water molecule, taken to be a sphere of radius 1 Å, onto the solute surface. The water molecule assigned to a given surface point is the closest molecule to the surface that has a silhouette covering the

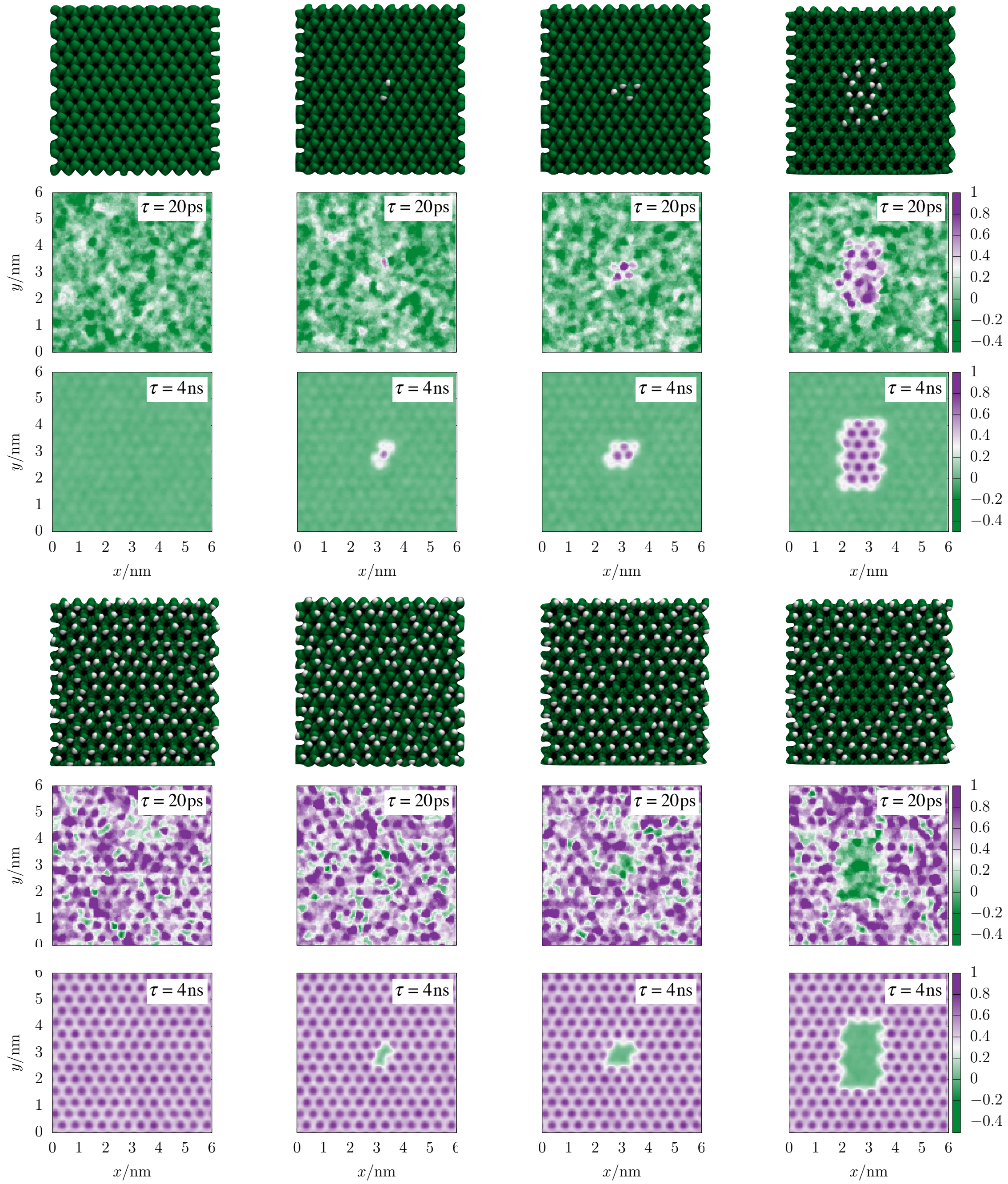

Figure 4.5 The interfacial structure of liquid water in contact with a series of different patterns of the model silica surface. Each different surface pattern is represented with an atomistic rendering of the model silica surface. Below each of these renderings are plot of the $\delta\lambda_{\mathrm{phob}}$, computed according to Eq. (4.3), with $\tau = 20$ ps and $\tau = 4$ ns.

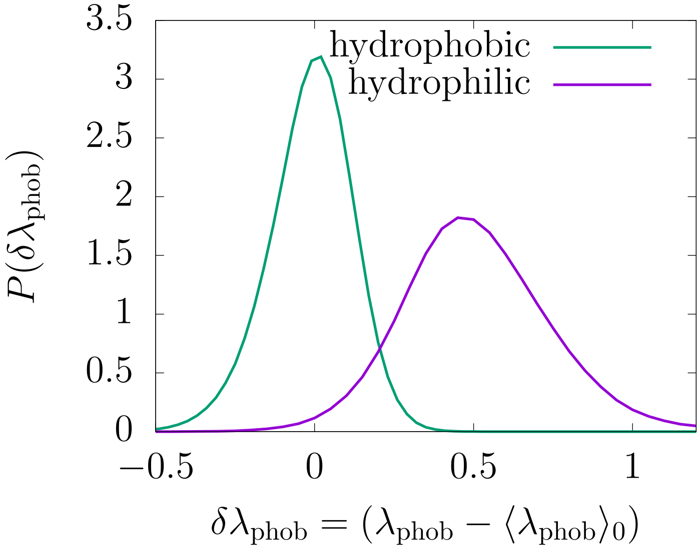

Figure 4.6 Probability distributions for $\delta\lambda_{\text{phob}}$ computed using $\tau = 20$ ps for an ideal hydrophobic reference system ("hydrophobic") and for a fully hydroxylated model silica surface ("hydrophilic") with SPC/E water.

given surface point.

The color scale of the spatial maps in Figs. 4.4 and 4.5 was selected based on the statistics of $\delta\lambda_{\text{phob}}$ computed within the reference system using $\tau = 20$ ps. Figure 4.6 shows the probability distribution, $P(\delta\lambda_{\text{phob}})$, computed within environment of the hydrophobic reference system (labeled "hydrophobic") and the environment of a fully hydroxylated silica surface (labeled "hydrophilic"). This figure illustrates two important points: (1) the hydrophobic and hydrophilic distributions are well separate, which makes $\delta\lambda_{\text{phob}}$ a good order parameter for hydrophobicity, and (2) the equilibrium fluctuations of $\delta\lambda_{\text{phob}}$ for an ideal hydrophobic interface extend over a range of about $-0.3 \leq \delta\lambda_{\text{phob}} \leq 0.3$. We thus interpret values of $\delta\lambda_{\text{phob}} \geq 0.3$ to indicate the presence of hydrophilic surfaces.

An alternate definition of $f(\vec{\gamma}|\text{ref})$

For computing $\delta\lambda_{\text{phob}}$ above, we used the definition of $f(\vec{\gamma}|\text{ref})$ that includes a normalizing probability, $P(\vec{\gamma}|\text{iso})$, as given in Eq. (4.1). $f(\vec{\gamma}|\text{ref})$ can be alternately defined without this normalizing probability, as $f(\vec{\gamma}|\text{ref}) = -\ln[P(\vec{\gamma}|\text{ref})]$. Results generated with this alternate, un-normalized definition are qualitatively identical. We illustrate this in Fig. 4.7, which contains data generated using the un-normalized value of $f(\vec{\gamma}|\text{ref})$. Specifically, Fig. 4.7(a) shows the associated spatial distribution of $\delta\lambda_{\text{phob}}$ computed on four of the model surfaces. These maps can be compared to the results in Fig. 4.7, which are computed using our standard (normalized) definition of $f(\vec{\gamma}|\text{ref})$. Figure 4.7(b) contains the probability distribution function for $\delta\lambda_{\text{phob}}$, using an averaging time of $\tau = 20$ ps, computed using a normalized (lines) and un-normalized (points) definition of $f(\vec{\gamma}|\text{ref})$. Here we observe that the distributions that

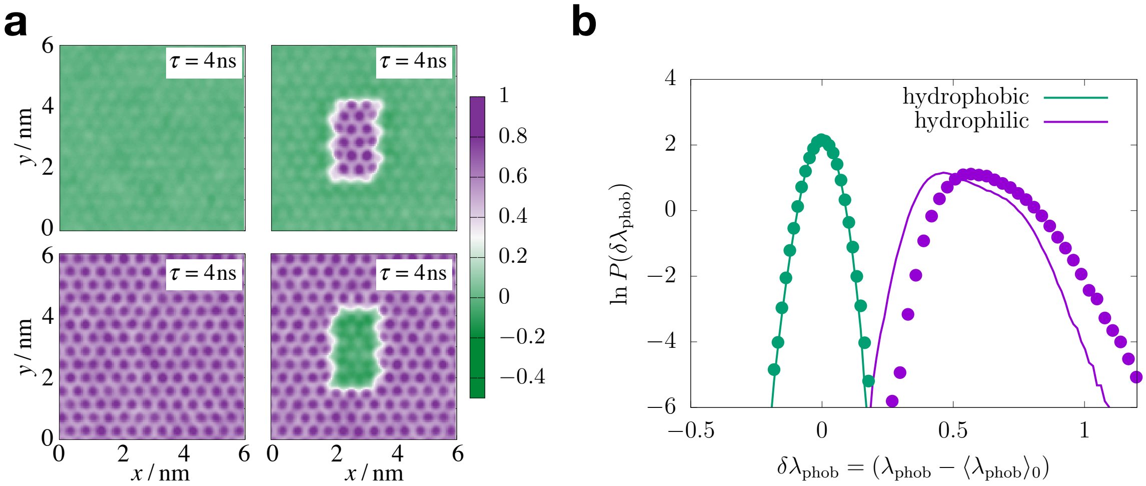

Figure 4.7 (a) Maps of $\delta\lambda_{\mathrm{phob}}$ computed using $f(\vec{\gamma}|\mathrm{ref}) = -\ln[P(\vec{\gamma}|\mathrm{ref})]$ for four of the patterned surfaces presented in Fig. 4.6. (b) Probability distributions for $\delta\lambda_{\mathrm{phob}}$ computed over the purely hydrophobic (green) and purely hydrophilic (purple) surfaces. Solid lines were computed using the definition of $f(\vec{\gamma}|\mathrm{ref})$ provided in Eq. (4.1) and filled circles were computed using $f(\vec{\gamma}|\mathrm{ref}) = -\ln[P(\vec{\gamma}|\mathrm{ref})]$.

use the un-normalized definition of $f(\vec{\gamma}|\mathrm{ref})$ are similar to those using the standard version. In fact, the distributions for the alternate definition are slightly more discriminating between the hydrophobic and hydrophilic surfaces. This suggests that the un-normalized definition may be more desirable for applications that rely on binary surface distinctions.

4.4 Application to Protein Surfaces

The results presented in the previous section verify that $\delta\lambda_{\mathrm{phob}}$ is effective as a local order parameter for surface hydrophobicity. This order parameter can thus be used to infer the effective hydration properties of an unknown aqueous surface. For the model silica surfaces, the heterogeneity in surface chemistry is mirrored by the spatial dependence of $\delta\lambda_{\mathrm{phob}}$. However, for more complex surfaces, the relationship between surface structure and $\delta\lambda_{\mathrm{phob}}$ is not so straightforward. When this is the case, $\delta\lambda_{\mathrm{phob}}$ can provide valuable physical insight into the relationship between surface heterogeneity and local hydration properties. In this section, we apply the method to the irregular surface of a protein which is both heterogeneous and dynamic.

4.4.1 Results and Discussions

The complex heterogeneous surface properties of hydrated proteins are reflected in the water's spatial dependence on interfacial molecular structure. Figure 4.8 illustrates that this spatial dependence can be revealed with $\delta\lambda_{\mathrm{phob}}$. Specifically, Fig. 4.8 illustrates the value of $\delta\lambda_{\mathrm{phob}}$ computed along the surface of the inactive CheY

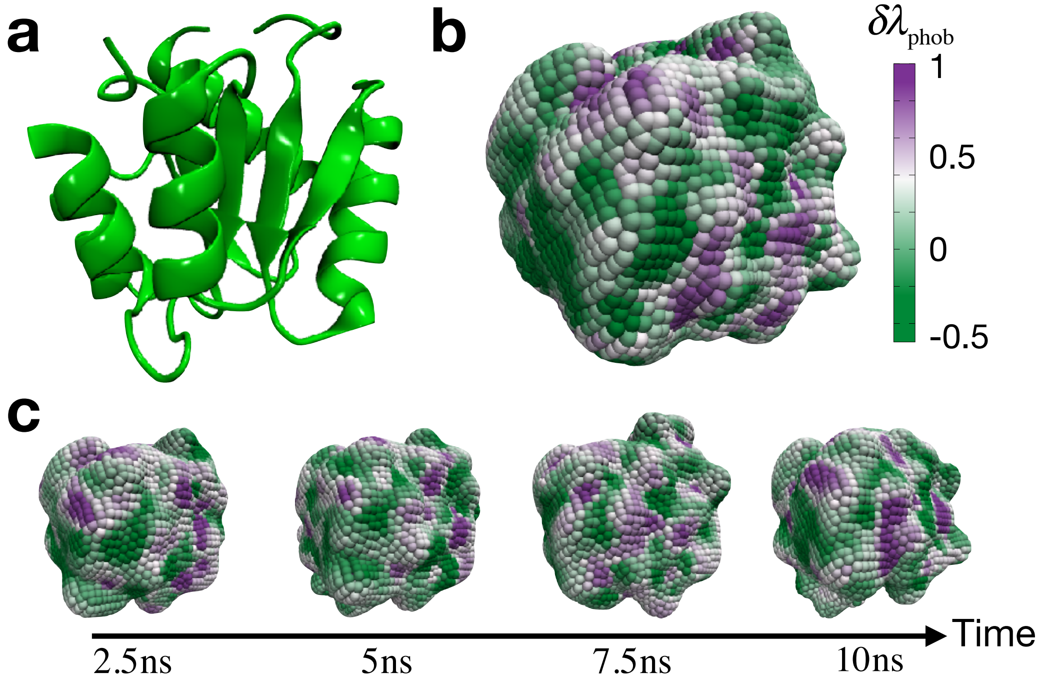

Figure 4.8 (a) Simulation snapshot of the CheY protein. Water molecules are omitted for clarity. (b) Map of $\delta\lambda_{\rm phob}$ computed for points along the surface of the protein using $\tau = 10$ ps. (c) Spatial maps of $\delta\lambda_{\rm phob}$ for a series of protein conformations spaced out along a 10 ns trajectory.

protein (PDB code: 1JBE) [109] using Eq. (4.3) and a value of $\tau = 10$ ps. This map of $\delta\lambda_{\rm phob}$ indicates regions of the protein surface whose interactions with water result in hydrophobic (*i.e.*, green shaded regions) or hydrophilic (*i.e.*, purple shaded regions) interfacial molecular structure.

Details of these protein surface maps, such as the positions and shapes of the hydrophilic domains, are sensitive to the conformational fluctuations of the protein. This is illustrated in Fig. 4.8(c), which shows the map of $\delta\lambda_{\rm phob}$ computed for the CheY protein for a consecutive sequence of conformations. The dynamics of interfacial structure can be further analyzed by considering the time dependence of $\delta\lambda_{\rm phob}$ for individual surface residues. Figure 4.9 shows the result of such a calculation performed along a 10 ns trajectory of the CheY protein. We observe that the interfacial structure in some regions of the protein remains relatively static, as indicated by persistent green or purple bands in Fig. 4.9(a), while other regions of the protein exhibit interfacial structure that fluctuates significantly in response to protein conformational dynamics. These differences in the dynamics of local interfacial molecular structure highlight an important feature of protein hydration. Namely, the folded structure of a protein can promote significant heterogeneity in the fluctuations of interfacial molecular structure. That is, the aqueous properties that mediate solvation and chemical reactivity are static along some region of the proteins yet highly variable in others. This heterogeneity may play an important role in controlling water-mediated processes such as protein aggregation and protein-ligand binding.

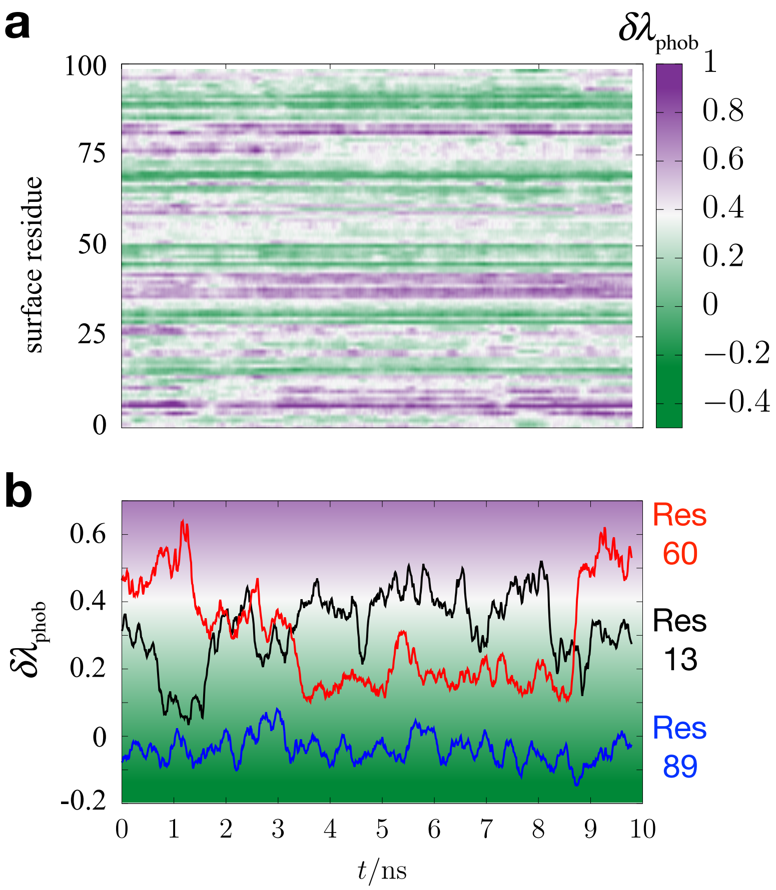

Figure 4.9 (a) A time series plot of $\delta\lambda_{\text{phob}}$, indicated by shading, as computed for individual surface residues of the CheY protein. In this plot, each row corresponds to a unique surface residue. (b) A plot highlighting the dynamics of $\delta\lambda_{\text{phob}}$ for three specific surface residues.

4.4.2 Computational Details

The crystal structure of inactive CheY (PDB code: 1JBE) [109] was taken for the simulation. The protein were added with hydrogen atoms and then immersed in a bath of explicit water through the AutoPSF and Solvate plugins of VMD [110]. The protein atoms are described by the all-atom CHARMM22 force field [111]. Water molecules follow the TIP3P potential [75] adapted for the CHARMM. Molecular dynamics simulation was performed in an NVT ensemble, enforced via a Langevin thermostat, with the LAMMPS package [37]. There are 8059 water molecules in the simulation cell with dimensions of 6.0 × 6.0 × 12.0 nm, and the system is of slab geometry. The slab is about 7 nm thick and the protein was ensured to be in the bulk liquid phase during the simulation. The system was equilibrated at $T = 298$ K for 1 ns and then run for 10 ns. From the equilibrium trajectory, configurations were sampled every 0.1 ps for computing $\delta\lambda_{\text{phob}}$. Particle Mesh Ewald was used to handle the long-range part of electrostatic interactions. The SHAKE algorithm was used to constrain the geometry of water.

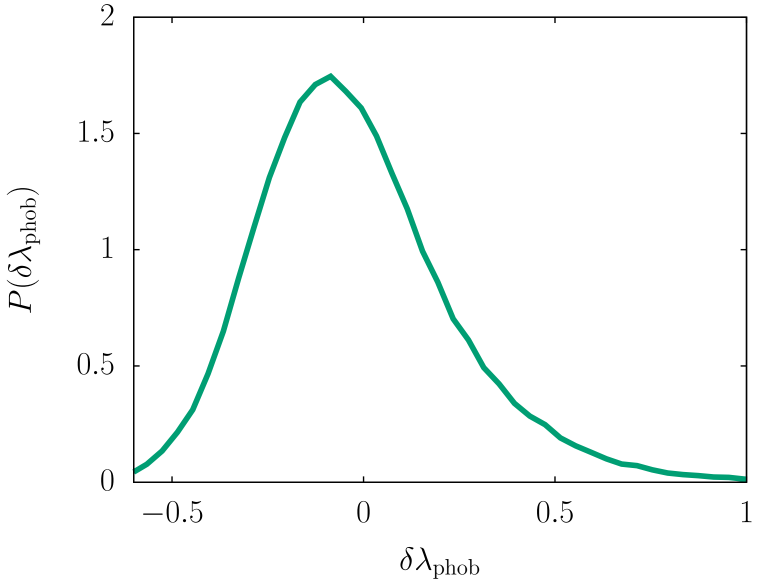

Figure 4.10 Probability distribution for $\delta\lambda_{\mathrm{phob}}$ computed using $\tau = 10$ ps for an ideal hydrophobic reference system with the TIP3P water.

As shown in Figure 4.8, $\delta\lambda_{\mathrm{phob}}$ was computed along the protein surface with temporal resolution. For the characterization, the coordinates of protein atoms were averaged over $\tau = 10$ ps and a Willard-Chandler surface was constructed, which encloses the protein, following the procedure given in Ref. 34. In the construction, the coarse-grained density was calculated on a cubic lattice with the spacing of $1.0\,\text{Å}$, using the Gaussian coarse-graining length of $2.0\,\text{Å}$ (for all atoms of protein). The half of bulk water density was used for the criterion of locating the surface. Each surface point is assigned with the nearest water from the first hydration shell (*i.e.*, $-1\,\text{Å} < a < 3\,\text{Å}$), and $\delta\lambda_{\mathrm{phob}}(\mathbf{r}_{\mathrm{surf}}, t)$ was computed along the surface points and time frames (spaced by τ). The corresponding reference system is the liquid–vapor interface of TIP3P water. Although its $f(\vec{\gamma}|\mathrm{phob})$ is qualitatively similar to that of SPC/E water, the probability distribution of $\delta\lambda_{\mathrm{phob}}$ is slightly different upon the given method of assigning water to surface points. We adapted the color scale such that we interpret values of $\delta\lambda_{\mathrm{phob}} \geq 0.375$ to indicate the presence of hydrophilic surfaces, where 0.375 is about 1.5 standard deviation of $P(\delta\lambda_{\mathrm{phob}})$ (see Fig. 4.10).

For the residue-based characterization, the orientational information of water molecules can be repartitioned with respect to specific residue. Per each time step, 10 water molecules in the first hydration shell, which are the closest to specific residue, were adopted for computing $\delta\lambda_{\mathrm{phob}}$. This analysis was applied to the surface residues that are exposed to sufficient number of water molecules. The surface residues were identified by counting the water molecules observed near individual residue and the cutoff criterion was more than 15 water molecules per time step (in average).

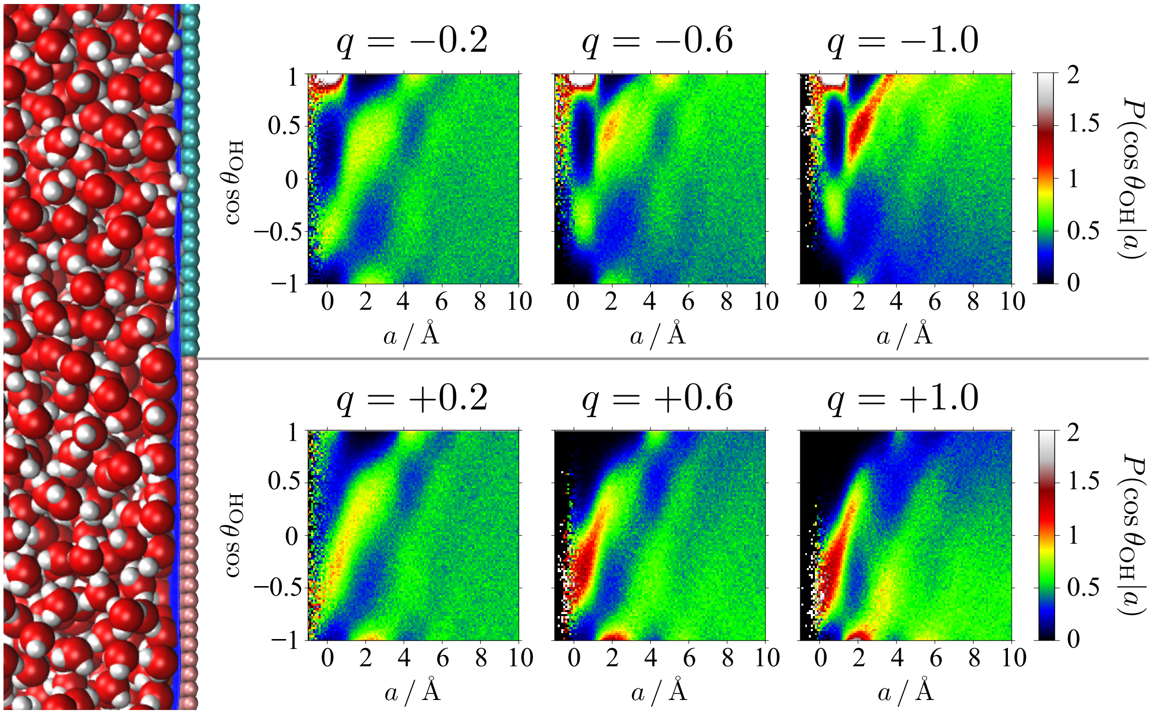

Figure 4.11 (left) Simulation snapshot of the water interface over a uniformly charged surface. (right) Plots of the orientational distribution, $P(\cos\theta_{\mathrm{OH}}|a)$, for the surfaces with different charges, where color shading indicates probability density. The top and bottom panels show the plots for the surfaces with negative and positive charges, respectively. The magnitudes of the surface charges are given in arbitrary units.

4.5 Application for Predicting Surface Charge

The ability to map the hydration dynamics of fluctuating irregular solutes is a unique feature of our interfacial characterization method. Of course, this method is not limited to the applications presented above. For instance, the approach can be easily extended to report on additional hydration properties with the use of different reference systems, such as systematically charged surfaces or those with specific curvature, or by expanding the definition of $\vec{\gamma}$, for example to include dynamical information. In this section, we briefly introduce the application of our theoretical framework for predicting the effective surface charge.

Again, we utilize the fact that water's interfacial molecular structure reflects the surface–water interactions. Specifically, the orientational structure of interfacial water molecules is influenced by the Coulomb interactions from the surface and thus sensitive to the surface charge. We demonstrate this by analyzing a molecular dynamics simulation for a slab of liquid water in contact with a uniformly charged surface.[2]

---

[2] In particular, we consider a surface that consists of point charges located along a square lattice with the spacing of 1 Å. As illustrated in Fig. 4.11, a half of the surface is positively charged and the other half is negatively charged in order to make the entire system electrically neutral. For the surface with dimensions of $5 \times 5\,\mathrm{nm}^2$, the orientational configurations of interfacial water molecules were sampled from the middle 1.5 nm of each half to compute $P(\vec{\gamma}|q)$.

As illustrated in Fig. 4.11, the orientational distribution differs depending on the scale and sign of charges on the surface. We can thus infer the local surface charge from the orientational configurations observed over a specific location of a chemically heterogeneous surface.

The procedure to determine the local surface charge is as follows. First, based on the formalism of Eq. (4.3), we quantify the local interfacial structure by considering the water interface over a uniformly charged surface as the reference system. That is, we compute

$$\lambda_q(\mathbf{r}_{\mathrm{surf}}, t) = -\frac{1}{N_\tau} \sum_{t'=t}^{t+\tau} \ln \frac{P(\vec{\gamma}(\mathbf{r}_{\mathrm{surf}}, t')|q)}{P(\vec{\gamma}(\mathbf{r}_{\mathrm{surf}}, t')|\mathrm{iso})} \ , \tag{4.4}$$

where $P(\vec{\gamma}|q)$ is the equilibrium probability for observing a water molecule with a specific configuration, $\vec{\gamma}$, over the surface of particular charge, q. As noted in Sec. 4.2.1, this quantity contains the likelihood function,

$$\mathcal{L}\big(q|\{\vec{\gamma}\}_{\mathbf{r}_{\mathrm{surf}},t}\big) = \prod_{t'=t}^{t+\tau} P(\vec{\gamma}(\mathbf{r}_{\mathrm{surf}}, t')|q) \ , \tag{4.5}$$

which measures how likely the given configurations are observed in the reference system. In other words, if the likelihood function is larger, the given interfacial configurations are more consistent with the equilibrium distribution for the water interface over the surface with charge q. Thus, we define the charge corresponding to the maximum likelihood as the effective charge at given time and surface position. In terms of λ_q, it is given by

$$q_{\mathrm{ML}}(\mathbf{r}_{\mathrm{surf}}, t) = \arg\min_q \lambda_q(\mathbf{r}_{\mathrm{surf}}, t) \ . \tag{4.6}$$

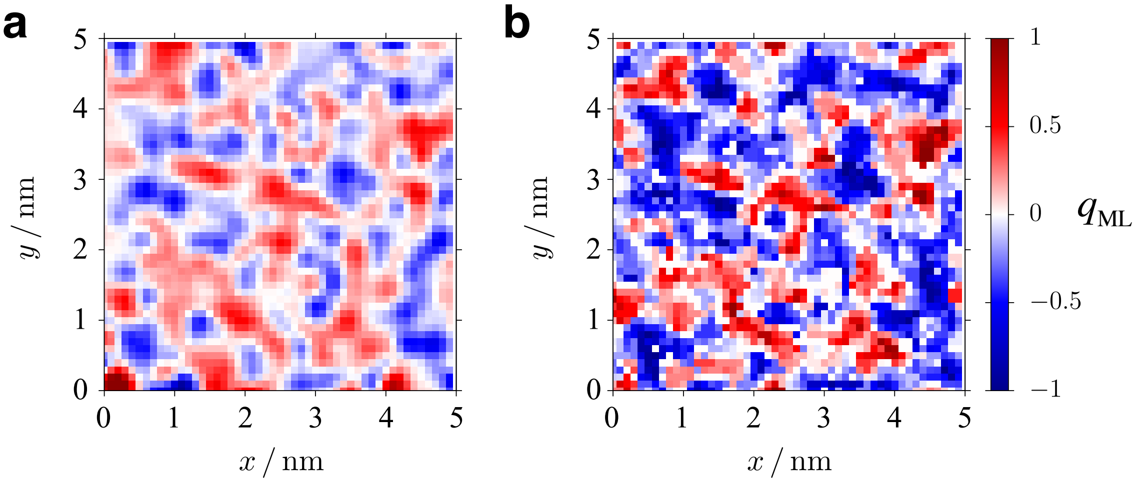

Figure 4.12 (a) Surface charge distribution smoothened from the point charges of the atoms in a model hydrophilic surface. (b) Charge distribution of the same surface computed from the maximum likelihood of water's interfacial molecular structure. Note that the color scale used in the panel (a) is not the same as that of the panel (b).

As an illustration, here we apply this method to the disordered hydrophilic surface generated from an immobilized slab of water (see Sec. 5.2.1 for the details). This model surface features the polar groups of random orientations such that the actual distribution of surface charge is heterogeneous as illustrated in Fig. 4.12(a). The surface charge distribution analyzed from water's interfacial molecular structure is plotted in Fig. 4.12(b), and it captures most of qualitative characteristics shown in Fig. 4.12(a). This result demonstrates that the interfacial water molecule encodes high-resolution details about the charge distribution of a chemically heterogeneous surface. We can also apply the scheme of Eqs. (4.4) and (4.6) to a protein surface along with the characterization methods described in the previous section. In that case, the resulting charge distribution, $q_{\mathrm{ML}}(\mathbf{r}_{\mathrm{surf}}, t)$, represents the effective local surface charge at given time which reflects the influence of protein's conformational fluctuations.

Chapter 5

Water's Interfacial Hydrogen Bonding Structure Reveals the Effective Strength of Surface–Water Interactions

The interactions of a hydrophilic surface with water can significantly influence the characteristics of the liquid water interface. In this chapter,[1] we explore this influence by studying the molecular structure of liquid water at a disordered surface with tunable surface-water interactions. We combine all-atom molecular dynamics simulations with a mean field model of interfacial hydrogen bonding to analyze the effect of surface-water interactions on the structural and energetic properties of the liquid water interface. We find that the molecular structure of water at a weakly interacting (*i.e.*, hydrophobic) surface is resistant to change unless the strength of surface-water interactions are above a certain threshold. We find that below this threshold water's interfacial structure is homogeneous and insensitive to the details of the disordered surface, however, above this threshold water's interfacial structure is heterogeneous. Despite this heterogeneity, we demonstrate that the equilibrium distribution of molecular orientations can be used to quantify the energetic component of the surface-water interactions that contribute specifically to modifying the interfacial hydrogen bonding network. We identify this specific energetic component as a new measure of hydrophilicity, which we refer to as the intrinsic hydropathy.

5.1 Introduction

In the vicinity of an extended hydrophilic surface, aqueous properties such as molecular mobility, solute solubility, and chemical reactivity can differ significantly from their bulk values [13, 27, 73, 112–116]. These differences reflect the characteristics of water's interfacial hydrogen bonding network and how these characteristics are influenced by the presence of surface-water interactions. The effect of these interactions

---

[1] This chapter borrows largely from arXiv:1801.10303 [cond-mat.soft].

are difficult to predict due to the collective structure of the aqueous interfacial hydrogen bonding network. Understanding the influence of surface-water interactions on this interfacial hydrogen bonding network is therefore fundamental to the study of hydrophilic solvation.

In this manuscript we investigate the response of the hydrogen bonding network to changes in the strength of surface-water interactions. We present the results of molecular dynamics simulations of the interface between liquid water and a model surface with tunable hydrophilicity. We utilize a rigid model surface that is molecularly disordered and includes polarized (*i.e.*, hydrogen bond-like) interactions that have heterogeneous orientations. We examine the structure of the interfacial hydrogen bonding network and how it varies when the strength of the surface-water interactions are changed. We find that hydrophilic surfaces, with surface-water interactions that are similar in strength to typical aqueous hydrogen bonds, give rise to interfacial molecular structure that is spatially heterogeneous. As we demonstrate, this heterogeneous structure includes some regions with interfacial molecular structure that is only weakly perturbed from that observed at an ideal hydrophobic surface. As we highlight, the persistence of this weakly perturbed, hydrophobic-like interfacial molecular structure may explain the ubiquity of hydrophobic effects in aqueous solvation.

The molecular structure of a liquid water interface is determined primarily by water's strong tendency to engage in tetrahedrally coordinated hydrogen bonding [117]. In the bulk liquid this tendency leads to the formation of a disordered tetrahedral hydrogen bonding network. The characteristics of this network determine many of water's physical properties, such as its density, heat capacity, and viscosity [29]. The individual hydrogen bonds that comprise this network are very energetically favorable, so any given bond within the bulk liquid is broken only fleetingly.[118] At an interface, however, geometric constraints make it impossible to simultaneously satisfy all available hydrogen bonds. Molecules at the interface thus reorganize to mitigate the loss of hydrogen bonds resulting in an interfacial hydrogen bonding network that is anisotropic and distorted relative to that of the bulk liquid [80]. Aqueous properties that depend on this network structure, such as small molecule solvation[119, 120] and proton transport[121, 122], thus vary in the vicinity of a liquid water interface.

Notably, the characteristics of water's interfacial molecular structure can be altered by the presence of external interactions, such as those that arise at a hydrophilic surface. Many previous studies have been aimed at revealing the microscopic properties of water at hydrophilic surfaces. Experimental efforts, such as those based on sum-frequency generation spectroscopy[60, 123, 124], terahertz absorption spectroscopy[95, 125], and dynamic nuclear polarization[96, 126], have uncovered important details about the microscopic structure and dynamics of the liquid water interface. These efforts have revealed that strong surface-water interactions can significantly reduce the mobility of interfacial water molecules and modify aqueous hydrogen bonding energetics [116, 127, 128]. Theoretical efforts, such as those based on first-principles calculations[129, 130], classical molecular dynamics (MD) simulations [94, 131], and continuum[46] or coarse-grained modeling[132] have provided fundamental physical insight into the role of hydrogen bonding in determining microscopic interfacial structure and have been vital to the interpretation of many experimental results.

Here we build upon these previous studies with a model system that is designed to allow for systematic variations in surface-water interactions. Our approach is unique because we use the collective structure of the interfacial hydrogen bonding network as an order parameter for quantifying water's interfacial molecular structure. We use this order parameter to resolve the spatial dependence of water's response to disordered but strongly interacting surfaces. We complement this approach by using a mean field model of interfacial hydrogen bonding to isolate the energetic component of these surface-water interactions that contribute specifically to reorganizing water's interfacial hydrogen bonding network. We then propose that this particular energetic component represents an intuitive measure of surface hydropathy.

Details about our model system and the methods we use to analyze and characterize water's interfacial molecular structure are described in the following section. Then, in Sec. 5.3, we present results and discuss how variations in surface-water interactions affect water's interfacial molecular structure. In Sec. 5.4, we describe a mean field model of interfacial hydrogen bonding and show how this model can be applied to quantify surface hydropathy.

5.2 Model and Methods

5.2.1 Disordered Model Surface with Tunable Hydrophilicity

Our model surface is constructed from an immobilized slab of bulk liquid water with variable partial charges that can be used to tune surface hydrophilicity. This model surface has been previously used to investigate the influence of surface-water interactions on interfacial density fluctuations.[51, 133] As illustrated in Fig. 5.1(a), our surface is constructed based on an equilibrium configuration of a slab of liquid water, spanning the periodic boundaries of the x-y plane. We define the surface as the set of water molecules whose oxygen atoms lie on one side of a plane perpendicular to the z-axis that cuts through the liquid water slab. The position of this plane is located with a value of z that is far enough from either interface as to characterize properties of the bulk liquid. Water molecules belonging to the surface are thus immobilized, fixed in a single configuration that is representative of the equilibrium bulk liquid.

Water molecules belonging to the model surface interact with a mobile population of ordinary water molecules via the standard water-water interaction potential. For the results presented below we utilize the SPC/E model of water,[35] however, this surface construction could be applied to any classical atomistic model of water. We tune the surface-water interactions by scaling the partial charges of the immobilized surface molecules by a factor of α, thereby scaling the polar hydrogen bonding interactions of surface molecules with those of the liquid. The charges on the surface oxygens and hydrogens are therefore given by $q_{\mathrm{O}}^{(\mathrm{surf})} = \alpha q_{\mathrm{O}}$ and $q_{\mathrm{H}}^{(\mathrm{surf})} = \alpha q_{\mathrm{H}}$, where q_{O} and q_{H} are the partial charges of the SPC/E model. Scaling the surface charges in this way preserves the charge neutrality of the surface.

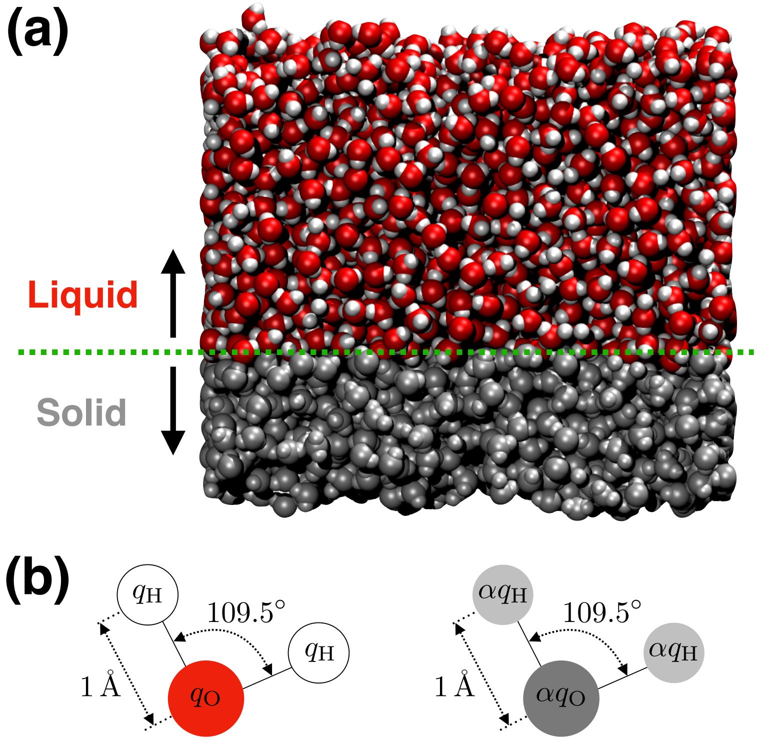

Figure 5.1 (a) A simulation snapshot of the model system. The disordered model surface is represented by grey-colored water molecules which are immobilized during the simulation. The liquid is represented by red and white-colored molecules. The green dotted line indicates the approximate location of the liquid-surface interface. (b) A schematic illustration highlighting the difference between standard SPC/E water molecules, which are described as three point charges arranged with a specific relative geometry and embedded within a Lennard-Jones potential, and the surface molecules, which are modeled identically except that the point charges are scaled by a factor of α.

To prepare the model surfaces that are used in the results described below we first equilibrated slab 3564 water molecules in a periodically replicated simulation cell with dimensions $5 \times 5 \times 12$ nm^3 at 298 K. The simulation cell is longer in the z-dimension so that the liquid water spontaneously forms a slab that is approximately 4.5 nm in thickness that contains two separated water-vapor interfaces. For a given configuration of the slab we defined the surface by drawing a horizontal plane through the liquid slab at a vertical position approximately 1.2 nm from the lower water-vapor interface. The resulting model surfaces are thus approximately 1.2 nm thick and contain about 1000 immobilized water molecules.

We used the above procedure to generate five different model surfaces based on independent equilibrium slab configurations. For each surface and each value of α, the dynamic population of non-surface (*i.e.*, liquid) water molecules were allowed to equilibrate in the presence of the surface for 0.1 ns at 298 K prior to gathering statistics. All simulations were performed in the NVT ensembles with the LAMMPS simulation package [37].

Details of simulation setup

Molecular geometries of the non-surface water molecules were constrained with the SHAKE algorithm. Particle Mesh Ewald was used to handle the long-range part of electrostatic interactions with the periodic boundary conditions in all directions. Cutoff distance for the long-range interaction was 10 Å. Propagation of dynamics was based on the standard velocity-Verlet integrator with a time step of 2 fs. The population of liquid water molecules were coupled to the Langevin thermal bath at $T = 298\,\mathrm{K}$ every 0.1 ps.

5.2.2 Method for Quantifying the Molecular Structure of a Liquid Water Interface

We characterize the molecular structure of the liquid water interface by analyzing the orientational statistics of interfacial water molecules. To do this we utilize a structural order parameter, $\delta\lambda_{\mathrm{phob}}$, that quantifies how these orientational statistics differ from those that arise at an ideal hydrophobic surface. As described in Ref. 134, this order parameter is capable of distinguishing hydrophobic and hydrophilic surfaces based only on the effect of these surfaces on aqueous interfacial molecular structure. Furthermore, $\delta\lambda_{\mathrm{phob}}$ can be formulated as a local order parameter to generate spatially resolved maps of water's interfacial molecular structure. We summarize the formulation of $\delta\lambda_{\mathrm{phob}}$ below. A more complete description of this order parameter can be found in Ref. 134.

To calculate $\delta\lambda_{\mathrm{phob}}$ we first sample the orientational configurations of interfacial water molecules. We denote the orientational configuration of a water molecule in terms of the three-dimensional vector, $\vec{\gamma} = (\cos\theta_1, \cos\theta_2, a)$, where θ_1 and θ_2 specify the angle made between each OH bond vector and the local surface normal and a specifies the distance of the water molecule from the nearest position of the instantaneous liquid water interface [34]. We define the position of the instantaneous liquid water interface following the procedure described in Sec. 2.1. For any given orientational configuration we can compute the quantity

$$f(\vec{\gamma}|\mathrm{phob}) = -\ln\left[\frac{P(\vec{\gamma}|\mathrm{phob})}{P(\vec{\gamma}|\mathrm{iso})}\right] , \tag{5.1}$$

where $P(\vec{\gamma}|\mathrm{phob})$ denotes the pre-tabulated probability to observe the specific molecular orientation, $\vec{\gamma}$, at an ideal hydrophobic interface and $P(\vec{\gamma}|\mathrm{iso})$ denote corresponding probability for the case when molecular orientations are distributed isotropically (*e.g.*, within the bulk liquid). For a given surface, the quantity $\delta\lambda_{\mathrm{phob}}$ simply reflects the average value of $f(\vec{\gamma}|\mathrm{phob})$ computed for water molecules at the interface.

Specifically, for a particular location, $\mathbf{r}_{\mathrm{surf}}$, along the plane of the liquid-surface interface,

$$\delta\lambda_{\mathrm{phob}}(\mathbf{r}_{\mathrm{surf}}) = \lambda_{\mathrm{phob}}(\mathbf{r}_{\mathrm{surf}}) - \langle\lambda_{\mathrm{phob}}\rangle_0, \tag{5.2}$$

where,

$$\lambda_{\mathrm{phob}}(\mathbf{r}_{\mathrm{surf}}) = \frac{1}{N_\tau}\sum_{t=0}^{\tau} f(\vec{\gamma}(\mathbf{r}_{\mathrm{surf}}, t)|\mathrm{phob}) , \tag{5.3}$$

and $\langle\lambda_{\text{phob}}\rangle_0$ represents the average value of λ_{phob} computed over an ideal hydrophobic surface. In Eq. 5.3, $\vec{\gamma}(\mathbf{r}_{\text{surf}}, t)$ specifies the orientational configuration of the water molecule that is nearest to the position $\mathbf{r}_{\text{surf}}$ at time t, the summation is taken over a discrete set of N_τ simulation snapshots sampled along the time interval τ. Here we sample simulation snapshots separated by 100 fs along a 1 ns trajectory (*i.e.*, $\tau = 1$ ns and $N_\tau = 10000$).

By definition, $\delta\lambda_{\text{phob}} \approx 0$ when water's interfacial molecular structure is similar to that of a hydrophobic surface. Surfaces that interact strongly with water molecules cause interfacial molecular structure to deviate from that of the hydrophobic reference system, which typically results in positive values for $\delta\lambda_{\text{phob}}$. By computing $\delta\lambda_{\text{phob}}(\mathbf{r}_{\text{surf}})$ locally, we can identify the spatial profile of interfacial distortions that arise due to water's interactions with a heterogeneous surface.

5.3 Effect of Surface Polarity on Water's Interfacial Molecular Structure

We evaluate the effect of surface-water interactions on water's interfacial molecular structure by analyzing simulations carried out using surfaces with different values of α. We consider values of α ranging from $\alpha = 0$, as an example of a disordered hydrophobic surface, to $\alpha = 1$, as an example of an ideal (*i.e.*, water-like) hydrophilic surface. For each value of α we have considered five independently generated surface configurations. For each surface configuration we have performed a 1 ns equilibrium simulation. We have analyzed each simulation by computing the value of $\delta\lambda_{\text{phob}}(\mathbf{r}_{\text{surf}})$ on a square lattice with lattice spacing equal to 0.5 Å along the plane of the liquid-surface interface. By definition, variations in $\delta\lambda_{\text{phob}}$ thus indicate changes in the molecular structure of the liquid water interface.

To establish an intuitive framework for interpreting variations in interfacial molecular structure we compare values of $\delta\lambda_{\text{phob}}(\mathbf{r}_{\text{surf}})$ to the quantity, $\Delta\mu_{\text{ex}}(\mathbf{r}_{\text{surf}})$, which denotes the change in excess chemical potential of a hard-sphere solute of radius 2.5 Å when the solute is brought from the bulk liquid to a position where it contacts the surface at $\mathbf{r}_{\text{surf}}$. $\Delta\mu_{\text{ex}}(\mathbf{r}_{\text{surf}})$ can be used to identify regions of a rigid hydrated surface that are either hydrophobic or hydrophilic[48, 50]. Here, we identify positions of the surface with $\Delta\mu_{\text{ex}} < -k_{\text{B}}T$ as being hydrophobic and those with $\Delta\mu_{\text{ex}} > k_{\text{B}}T$ as being hydrophilic. By comparing the statistics of $\delta\lambda_{\text{phob}}$ at hydrophobic and hydrophilic surface sites (see Sec. 5.3.2 for more details), we have thus identified the range of $\delta\lambda_{\text{phob}}$ that correspond to either hydrophobic or hydrophilic interfacial molecular structure. In particular, we have found that values of $-0.1 \le \delta\lambda_{\text{phob}} \le 0.1$ are indicative of typical hydrophobic molecular structure and values of $|\delta\lambda_{\text{phob}}| > 0.1$ are indicative of hydrophilic interfacial molecular structure.

5.3.1 Results and Discussions

To analyze our results, we first consider the effect of α on $\langle\delta\lambda_{\text{phob}}\rangle$, the value of our order parameter averaged over all surface positions and surface realizations. As

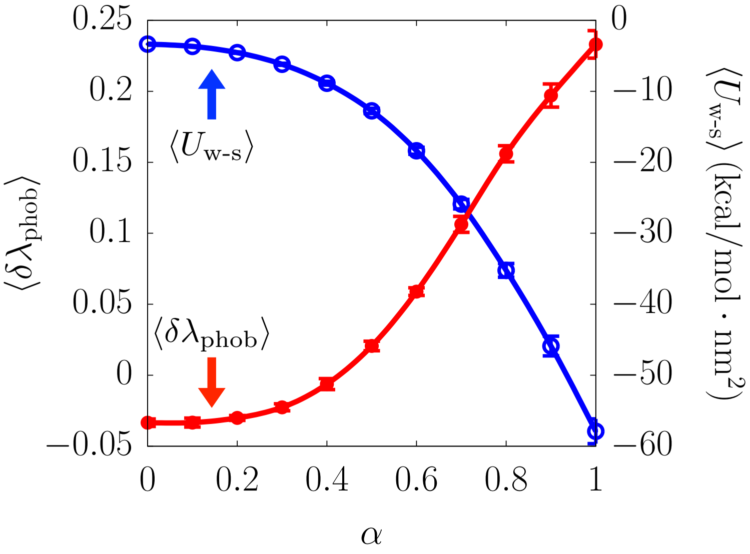

Figure 5.2 A plot of the α dependence of $\langle \delta\lambda_{\text{phob}} \rangle$ (red line plotted against the left vertical axis) and $\langle U_{\text{w-s}} \rangle$ (blue line plotted against the right vertical axis).

illustrated in Fig. 5.2, $\langle \delta\lambda_{\text{phob}} \rangle \approx 0$ for surfaces with $\alpha = 0$, indicating that apolar uncharged surfaces give rise to interfacial molecular structure that is characteristically hydrophobic. We observe that water's interfacial molecular structure depends weakly on α when $0 \leq \alpha \lesssim 0.4$, suggesting that there is a threshold in surface polarity that must be overcome in order to affect significant change in water's interfacial molecular structure. Beyond this threshold, $\langle \delta\lambda_{\text{phob}} \rangle$ increases steadily and takes on values associated with hydrophilic interfacial structure (*i.e.*, $\langle \delta\lambda_{\text{phob}} \rangle > 0.1$) when $\alpha \gtrsim 0.6$.

To better understand the effect of α on interfacial molecular structure we have computed the average surface-water interaction energy,

$$\langle U_{\text{w-s}} \rangle = \left\langle \sum_{i \in \text{surf}} \sum_{j \in \text{liq}} u_{ij} \right\rangle , \tag{5.4}$$

where the angle brackets represent an equilibrium average, the first summation is taken over all frozen surface molecules, the second summation is taken over all molecules in the liquid, and u_{ij} represents the pair potential for interactions between surface species and molecules within the liquid. We observe that the dependence of $\langle U_{\text{w-s}} \rangle$ on α is complementary to that of $\langle \delta\lambda_{\text{phob}} \rangle$. Specifically, $\langle U_{\text{w-s}} \rangle$ varies nonlinearly with α, slowly for $0 \leq \alpha \lesssim 0.4$ and more rapidly for $\alpha \gtrsim 0.4$. This complementarity shows that the changes in interfacial molecular structure that are indicated by increases in $\langle \delta\lambda_{\text{phob}} \rangle$ when $\alpha > 0.4$ are enabled by the formation of more favorable surface-water interactions. Moreover, the reluctance of $\langle \delta\lambda_{\text{phob}} \rangle$ to change when the value of α is small illustrates that water's interfacial hydrogen bonding network is determined by a competition between the strength of surface-water and water-water interactions. These results thus reveal the strength of favorable surface-water interactions (in terms of α) that are required to offset the free energy costs associated with the reorganization of interfacial hydrogen bonding.

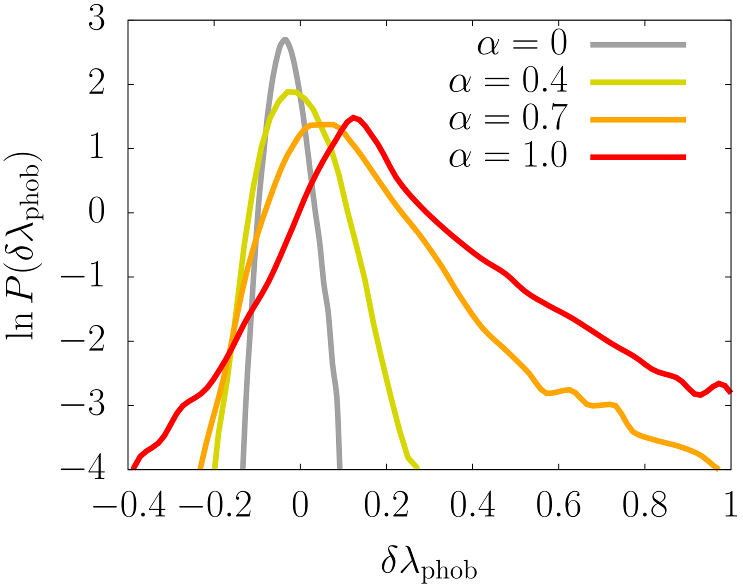

Figure 5.3 A plot of the probability distribution for $\delta\lambda_{\mathrm{phob}}$ computed for surfaces with different values of α. These distributions exhibit mean behavior that shifts systematically with α and the appearance of pronounced non-Gaussian tails at larger values of α.

The values of $\langle\delta\lambda_{\mathrm{phob}}\rangle$ that are plotted in Fig. 5.2 represent a spatial average over heterogeneous surfaces. To understand the effects of surface heterogeneity on local interfacial molecular structure we analyze the statistics of $\delta\lambda_{\mathrm{phob}}(\mathbf{r}_{\mathrm{surf}})$ computed locally at various positions along the liquid-surface interface. We characterize the statistics of this local interfacial molecular structure in terms of $P(\delta\lambda_{\mathrm{phob}})$, the probability to observe a given value of $\delta\lambda_{\mathrm{phob}}$ at a specfic point along the surface. Plots of $P(\delta\lambda_{\mathrm{phob}})$ computed for surfaces with different values of α are shown in Fig. 5.3. We observe that when $\alpha = 0$, $P(\delta\lambda_{\mathrm{phob}})$ is approximately Gaussian with a narrow width centered at $\delta\lambda_{\mathrm{phob}} \approx 0$. For larger values of α, however, $P(\delta\lambda_{\mathrm{phob}})$ has pronounced non-Gaussian tails at large values of $\delta\lambda_{\mathrm{phob}}$. Unlike the peak behavior of $P(\delta\lambda_{\mathrm{phob}})$, which exhibits a small shift with increasing α, the large-$\delta\lambda_{\mathrm{phob}}$ tails are extremely sensitive to changes in α. These tails indicate that when $\alpha \geq 0.4$, the probability to observe regions with highly distorted interfacial molecular structure is many orders of magnitude larger than would be expected based on Gaussian statistics.

The behavior of $P(\delta\lambda_{\mathrm{phob}})$ indicates that surfaces with $\alpha \geq 0.4$ give rise to aqueous interfacial molecular structure that is heterogeneous. To understand the spatial distribution of this heterogeneous interfacial molecular structure we plot $\delta\lambda_{\mathrm{phob}}(\mathbf{r}_{\mathrm{surf}})$ computed for a single fixed surface configuration with different values of α. The series of panels in Fig. 5.4 illustrate how α affects the spatial variations in water's interfacial molecular structure. When α is small, the structure of the aqueous interface is homogeneous with $\delta\lambda_{\mathrm{phob}} \approx 0$. The spatial distribution of $\delta\lambda_{\mathrm{phob}}$ is similar for surfaces with $0 \leq \alpha \leq 0.4$, consistent with the results presented in Figs. 5.2 and 5.3. When $\alpha > 0.4$, however, we observe the appearance of localized, approximately water-sized domains that have larger values of $\delta\lambda_{\mathrm{phob}}$. These domains correspond to the fat tails

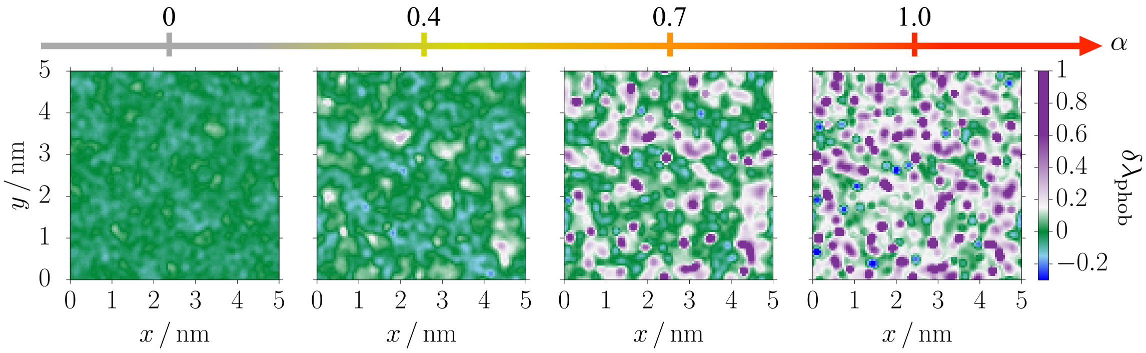

Figure 5.4 Spatial maps of $\delta\lambda_{\mathrm{phob}}$ computed for points distributed along the plane of the liquid-surface interface. For each value of α, the plotted values of $\delta\lambda_{\mathrm{phob}}$, as indicated by shading, have been averaged over a 1 ns trajectory. The molecular configuration of the surface is identical for each of the panels. The color bar is designed to distinguish between regions with interfacial molecular structure that is indicative of hydrophobic surfaces (green shaded regions) and hydrophilic surfaces (purple and blue shaded regions).

in $P(\delta\lambda_{\mathrm{phob}})$ that are plotted in Fig. 5.3.

Notably, even the most hydrophilic surface that we considered (*i.e.*, the $\alpha = 1$ surface) includes many regions with interfacial molecular structure that is hydrophobic-like. In fact, the signatures of this hydrophobic interfacial structure are evident in over 25% of the interfacial area of the $\alpha = 1$ surface. These regions are associated with the peak behavior of $P(\delta\lambda_{\mathrm{phob}})$, which as Fig. 5.3 illustrates, originates directly from a systematic α-induced shift in the $\alpha = 0$ distribution. This observation indicates that the specific molecular structure that is adopted by water at a hydrophobic interface resides in a basin of thermodynamic stability that is robust to moderate surface-induced perturbations. We attribute the stability of this hydrophobic interfacial molecular structure to the strong influence of the bulk liquid hydrogen bond network on the orientations of interfacial water molecules. A surface must overcome this influence in order to cause significant changes in water's interfacial molecular structure.

The tendency for liquid water to adopt hydrophobic-like interfacial molecular structure, even at hydrophilic surfaces, highlights the importance of this particular interfacial hydrogen bonding arrangement in aqueous solvation. For instance, this particular interfacial structure determines the thermodynamic driving forces that underlie the hydrophobic effect [135]. Thus, in order to mitigate hydrophobic effects a surface must include a high density of surface sites whose interactions with water molecules are sufficiently strong as to overcome the hydrogen bonding interactions imposed by the adjacent bulk liquid.

Unlike many hydrated surfaces and large solutes, the surfaces we have considered are completely rigid. Without this rigidity, the spatial heterogeneity exhibited in Fig. 5.4 would be absent. For dynamic surfaces we expect that heterogeneity in the distribution of $\delta\lambda_{\mathrm{phob}}$, such as indicated by the fat tails in Fig. 5.3, would still be evident. However, the presence of spatial heterogeneity, such as illustrated in Fig. 5.4, would be limited to timescales characteristic of surface dynamics. If the time scale for surface reorganization is similar to that of interfacial water molecules, then evidence of spatial heterogeneity would vanish. However, for most extended hydrated surfaces, such as those of proteins or other biological macromolecules, surface reorganization is coupled to conformational dynamics and is therefore slow relative to typical solvent dynamics.

5.3.2 Interfacial Molecular Structure vs. Excess Chemical Potential

In order to relate the aqueous interfacial molecular structure to the surface hydropathy, we compare values of $\delta\lambda_{\mathrm{phob}}$ to quantity, $\Delta\mu_{\mathrm{ex}} = \mu_{\mathrm{ex}}^{(\mathrm{int})} - \mu_{\mathrm{ex}}^{(\mathrm{bulk})}$, where $\mu_{\mathrm{ex}}^{(\mathrm{int})}$ and $\mu_{\mathrm{ex}}^{(\mathrm{bulk})}$ are the excess chemical potentials for inserting a hard-sphere solute near the interface and in the bulk water, respectively. For a given location over a hydrated surface, namely $\mathbf{r}_{\mathrm{surf}}$, the excess chemical potential near the interface can be specified as

$$\mu_{\mathrm{ex}}^{(\mathrm{int})}(\mathbf{r}_{\mathrm{surf}}) = -k_B T \ln P_v(0|\mathbf{r}_{\mathrm{surf}}) \ , \tag{5.5}$$

where $P_v(0|\mathbf{r}_{\mathrm{surf}})$ is the probability that no solvent molecule is observed within a spherical cavity of radius R centered at $\mathbf{r}_{\mathrm{surf}} + R\hat{z}$ (*i.e.*, the cavity contacts with the surface at $\mathbf{r}_{\mathrm{surf}}$). This probability is computed from the simulation as

$$P_v(0|\mathbf{r}_{\mathrm{surf}}) = \left\langle \delta\left(\sum_i H(R - |\mathbf{r}_i - \mathbf{r}_{\mathrm{surf}} - R\hat{z}|)\right)\right\rangle \ , \tag{5.6}$$

where the angle bracket denotes an equilibrium average, $\delta(x)$ is a Dirac-delta function, $H(x)$ is a Heaviside step function, and the summation is taken over all liquid water molecules for their positions, $\mathbf{r}_i$. For $\mathbf{r}_{\mathrm{surf}}$, the surface boundary was determined from a Willard-Chandler interface [34] constructed for the molecules belonging to the solid phase. Similarly, the probability of a cavitation was computed in the bulk, which gave $\mu_{\mathrm{ex}}^{(\mathrm{bulk})} = 4.0\, k_{\mathrm{B}}T$ for $R = 2.5$ Å.

Based on the values of $\delta\lambda_{\mathrm{phob}}(\mathbf{r}_{\mathrm{surf}})$ and $\Delta\mu_{\mathrm{ex}}(\mathbf{r}_{\mathrm{surf}})$ for all surface positions, we computed conditional probability distributions, $P(\delta\lambda_{\mathrm{phob}}|\Delta\mu_{\mathrm{ex}})$. Here, we identify the positions of the surface with $\Delta\mu_{\mathrm{ex}} < -k_{\mathrm{B}}T$ as being hydrophobic and those with $\Delta\mu_{\mathrm{ex}} > k_{\mathrm{B}}T$ as being hydrophilic. As illustrated in Fig. 5.5, $P(\delta\lambda_{\mathrm{phob}}|\Delta\mu_{\mathrm{ex}} < -k_{\mathrm{B}}T)$ is dominant over $P(\delta\lambda_{\mathrm{phob}}|\Delta\mu_{\mathrm{ex}} > k_{\mathrm{B}}T)$ in the range of $|\delta\lambda_{\mathrm{phob}}| \lesssim 0.1$, and thus we interpret the values of $-0.1 \leq \delta\lambda_{\mathrm{phob}} \leq 0.1$ as hydrophobic interfacial molecular structure and values of $|\delta\lambda_{\mathrm{phob}}| > 0.1$ as hydrophilic interfacial molecular structure.

5.4 Quantifying Surface Hydropathy from Water's Interfacial Molecular Structure

In this section we introduce the concept of intrinsic hydropathy (IH), which describes the extent to which a hydrated surface alters the intrinsic molecular structure of the liquid water interface. This quantity is determined by a competition between the

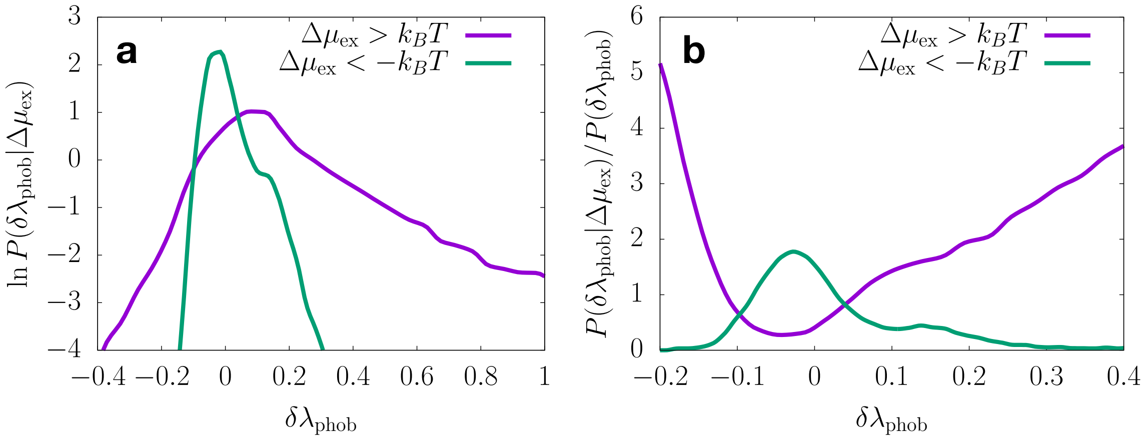

Figure 5.5 (a) Plots of conditional probability distributions of $\delta\lambda_{\text{phob}}$ given $\Delta\mu_{\text{ex}} > k_{\text{B}}T$ and $\Delta\mu_{\text{ex}} < -k_{\text{B}}T$. (b) Plots of the conditional probability distributions normalized by $P(\delta\lambda_{\text{phob}})$. Although the panel b shows that the righthand crossing point between the curves is $\delta\lambda_{\text{phob}} \approx 0.5$, we set the upper bound of hydrophobic interfacial molecular structure to be $\delta\lambda_{\text{phob}} = 1.0$ where $P(\delta\lambda_{\text{phob}}|\Delta\mu_{\text{ex}} > k_{\text{B}}T)$ reaches the maximum and $P(\delta\lambda_{\text{phob}}|\Delta\mu_{\text{ex}} < -k_{\text{B}}T)$ is featured with some shoulder as shown in panel a.

constraints imposed on interfacial water molecules by surface-water interactions and those imposed by the collective hydrogen bonding network of the surrounding liquid. The outcome of this competition depends specifically on the subset of surface-water interactions that affect the orientational preferences of interfacial water molecules. Unfortunately, it is not straightforward to separate these specific interactions from the total set of surface-water interactions, so quantifying their effective strength is challenging. Here we address this challenge by considering the statistical mechanics of interfacial hydrogen bonding.

We utilize a mean field model of aqueous interfacial hydrogen bonding at a uniform surface that interacts with water through hydrogen bond-like interactions of tunable strength. This model surface has a well-defined IH value, which is simply given by the energy of a surface-water hydrogen bond. By tuning this energy we can determine how water's interfacial molecular structure depends on the value of the IH. We then exploit this dependence to assign IH values to surfaces based solely on their influence on water's interfacial molecular structure.

In the following subsection we describe the mean field model of aqueous interfacial hydrogen bonding. Then, we present the application of this model to quantifying the IH of the disordered molecular surfaces described in the previous sections.

5.4.1 A Mean-Field Model of Interfacial Hydrogen Bonding at an Interacting Surface

Here we describe a theoretical model for computing the orientational distribution function of molecules at the interface between liquid water and an interacting surface. This model is an extension of a similar theoretical framework, introduced in

Ref. 117, for computing interfacial molecular structure at the liquid water-vapor interface. In Ref. 117, we show that this model framework can accurately reproduce the primary features of the molecular structure of the water-vapor interface, and here we apply it to describe the water-surface interface. We specify interfacial molecular structure in terms of the orientational distribution function for water molecules at various distances from the liquid water interface. Within this model framework, this distribution function is determined based on the orientational preferences of an individual probe molecule interacting with the average density field of the interfacial environment via an empirical hydrogen bonding potential.

As illustrated in Fig. 5.6, the model includes a single probe molecule located at distance a from the position of a planar liquid interface. The interfacial environment is described with a density field that is anisotropic in the direction perpendicular to the interface but uniform in the directions parallel to the interface. The interfacial density field is composed of two separate elements: a water density, $\rho_{\mathrm{w}}(a)$, that is computed form atomistic simulation and a surface density, $\rho_{\mathrm{s}}(a)$, that represents the distribution of interacting sites on the extended model surface. As depicted in Fig. 5.6, we approximate this distribution as being Gaussian with characteristics that reflect the molecular roughness of a given hydrated surface.

The probe molecule is described as a point particle with four tetrahedrally coordinated hydrogen bond vectors, denoted $\mathbf{b}_1$, $\mathbf{b}_2$, $\mathbf{b}_3$, and $\mathbf{b}_4$ (see Fig. 5.6). The length of these vectors corresponds to the average hydrogen bond distance, $d_{\mathrm{HB}} = 2.8$ Å [75], so that each vector points to the preferred position of a hydrogen bond partner. In addition, each bond vector is assigned a directionality, with $\mathbf{b}_{1,2}$ and $\mathbf{b}_{3,4}$ representing hydrogen bond donors and acceptors, respectively. The orientation of this probe particle is specified by the vector $\vec{\kappa} = (\cos\theta_1, \cos\theta_2)$, where θ_1 and θ_2 specify the angles made between the donor bond vectors and the surface normal pointing away from the bulk.

The interactions of the probe molecule with the elements of the interfacial density field are governed by an empirical hydrogen bonding potential that depends on the probe molecule's position, a, orientation, $\vec{\kappa}$, and hydrogen bonding configuration, as specified by a set of binary variables, $\{n_k^{(\nu)}\}$. This potential is given by,

$$E(\vec{\kappa}, a, \{n_k^{(\nu)}\}) = \sum_{i=1}^{4} \left[\epsilon_{\mathrm{w}} n_i^{(\mathrm{w})}(a, \mathbf{b}_i) + \epsilon_{\mathrm{s}} n_i^{(\mathrm{s})}(a, \mathbf{b}_i)\right] \ , \tag{5.7}$$

where ϵ_{w} denotes the effective energy of a water-water hydrogen bond, ϵ_{s} represents the effective energy of a surface-water hydrogen bond, and $n_i^{(\nu)}$ indicates the hydrogen bonding state of the ith bond vector to either water (*i.e.*, $\nu = \mathrm{w}$) or the surface (*i.e.*, $\nu = \mathrm{s}$). Specifically, $n_i^{(\nu)} = 1$ if the probe molecule has formed a hydrogen bond of type ν along $\mathbf{b}_i$ and $n_i^{(\nu)} = 0$ otherwise. Here we treat each $n_i^{(\nu)}$ as an independent random variable with statistics given by,

$$n_i^{(\nu)} = \begin{cases} 1, & \text{with probability } P_{\mathrm{HB}}^{(\nu)}(a_i) \ , \\ 0, & \text{with probability } 1 - P_{\mathrm{HB}}^{(\nu)}(a_i) \ , \end{cases} \tag{5.8}$$

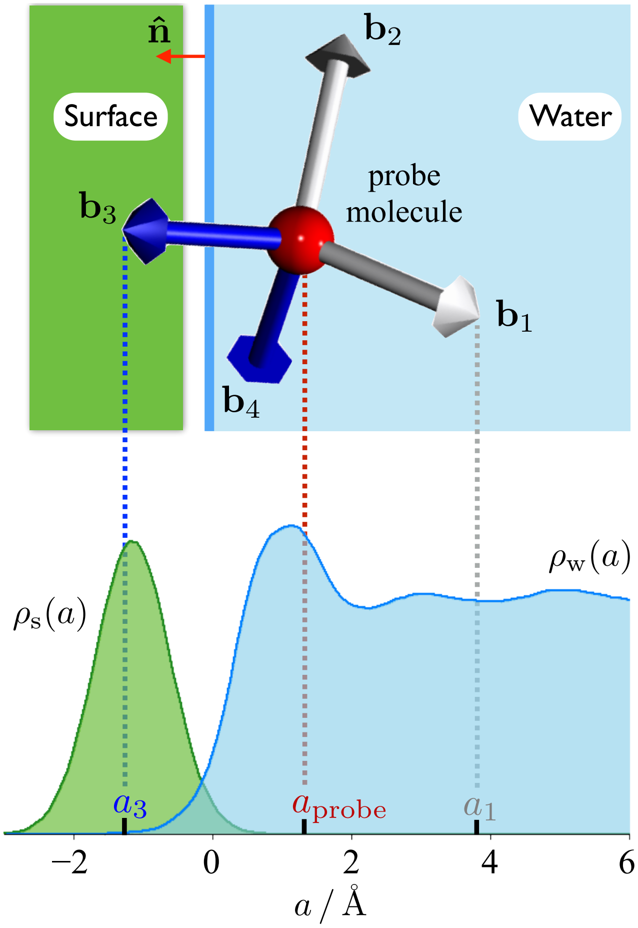

Figure 5.6 Schematic depiction of the mean-field model showing a probe molecule with tetrahedrally coordinated bond vectors (white for donor, blue for acceptor) at a distance a_{probe} from the position of the instantaneous interface (solid blue line). The probe molecule within the liquid phase (blue shaded region) can have hydrogen bonds to either neighboring solvent molecules or nearby solute (green shaded region) through the bond vectors. A plot of the interfacial density profile of liquid water, $\rho_{\mathrm{w}}(a)$, obtained from the MD simulation with SPC/E water, is shown along with that of an empirical solute density profile, $\rho_{\mathrm{s}}(a)$, where gray and blue dotted lines indicate the termination points of bond vectors $\mathbf{b}_1$ and $\mathbf{b}_3$ respectively.

where $a_i = a - \mathbf{b}_i \cdot \hat{\mathbf{n}}$ denotes the terminal position of the ith bond vector, $\hat{\mathbf{n}}$ is the unit vector normal to the plane of the interface, and $P_{\mathrm{HB}}^{(\nu)}(a_i)$ specifies the probability to form a hydrogen bond at position a_i with either water (*i.e.*, $\nu = \mathrm{w}$) or surface (*i.e.*, $\nu = \mathrm{s}$). We assume that this probability takes the simple form, $P_{\mathrm{HB}}^{(\nu)}(a_i) \propto \rho_\nu(a_i)$, where the proportionality constant is chosen to reproduce average number of hydrogen bonds in the bulk liquid. We also assume that these statistics are subject to a constraint that each bond vector can form only one bond (*i.e.*, $\mathbf{b}_i$ cannot simultaneously bond with water and surface).

The water-water hydrogen bond energy is fixed at a value of $\epsilon_{\mathrm{w}} = -1.77\,k_{\mathrm{B}}T$ at $T = 298\mathrm{K}$, based on our previous parameterization of this model for the liquid water-vapor interface of the SPC/E water (see Sec. 3.4.2). The surface-water hydrogen bond energy, ϵ_{s}, is thus a parameter that we vary in order to describe surfaces with different chemical characteristics. We define the properties of $\rho_{\mathrm{s}}(a)$ based on the analysis of simulation data. Specifically, for a given model surface we computed the density of surface molecules relative to the position of the intrinsic water interface. We then fit the leading edge of the resulting density profile to a Gaussian. This procedure yielded a range of means, a_{s}, and variances, σ_{s}^2, that ranged approximately from $a_{\mathrm{s}} = -2.1\,\text{Å}$ to $-1.1\,\text{Å}$ and $\sigma_{\mathrm{s}} = 0.4\,\text{Å}$ to $0.6\,\text{Å}$ for values of $\alpha = 0$ to 1, respectively. Specific parameters for each value of α are described in Sec. 5.4.3.

In the context of this model, the probability for a molecule at position a to adopt a given orientation, $\vec{\kappa}$, can thus be expressed as,

$$P_{\mathrm{MF}}(\vec{\kappa}|a) = \left\langle e^{-\beta E(\vec{\kappa},a,\{n_k^{(\nu)}\})} \right\rangle_{\mathrm{b}} / Z(a), \tag{5.9}$$

where $\langle \cdots \rangle_{\mathrm{b}}$ denotes an average over all possible hydrogen bonding states (*i.e.*, variations in the $n_i^{(\nu)}$'s), $\beta = 1/k_{\mathrm{B}}T$, and $Z(a) = \int d\vec{\kappa} \left\langle e^{-\beta E(\vec{\kappa},a,\{n_k^{(\nu)}\})} \right\rangle_{\mathrm{b}}$ is the orientational partition function for the probe molecule at position a. By evaluating the average explicitly based on the constrained statistics of $n_i^{(\nu)}$ as specified above, the numerator of Eq. (5.9) can be written as,

$$\left\langle e^{-\beta E(\vec{\kappa},a,\{n_k^{(\nu)}\})} \right\rangle_{\mathrm{b}} = \prod_{i=1}^{4} \left[1 + P_{\mathrm{HB}}^{(\mathrm{w})}(a_i)(e^{-\beta\epsilon_{\mathrm{w}}} - 1) + P_{\mathrm{HB}}^{(\mathrm{s})}(a_i)(e^{-\beta\epsilon_{\mathrm{s}}} - 1) \right]. \tag{5.10}$$

Together, Eqs. (5.9) and (5.10) can be used to compute the orientational molecular structure of the liquid water interface. To facilitate comparison of this mean field model to the results of atomistic simulation, we project the distribution $P_{\mathrm{MF}}(\vec{\kappa}|a)$ onto a reduced dimensional distribution,

$$P_{\mathrm{MF}}(\cos\theta_{\mathrm{OH}}|a) = \int d\vec{\kappa} P_{\mathrm{MF}}(\vec{\kappa}|a) \left[\frac{1}{2} \sum_{i=1}^{2} \delta(\cos\theta_i - \cos\theta_{\mathrm{OH}}) \right], \tag{5.11}$$

where the summation is taken over the two donor bond vectors, $\cos\theta_i = \mathbf{b}_i \cdot \hat{\mathbf{n}}/|\mathbf{b}_i|$, and $\delta(x)$ is the Dirac delta function.

5.4.2 Quantifying Intrinsic Hydropathy from Atomistic Simulation Data

The characteristics of $P_{\mathrm{MF}}(\cos\theta_{\mathrm{OH}}|a)$ depend on the value of the surface-water hydrogen bond energy, ϵ_{s}. Similarly, the characteristics of $P_{\mathrm{sim}}(\cos\theta_{\mathrm{OH}}|a)$ computed from simulations with the molecular surfaces described in the previous section (and depicted in Fig. 5.1 depend on the value of α. By comparing $P_{\mathrm{MF}}(\cos\theta_{\mathrm{OH}}|a)$ and $P_{\mathrm{sim}}(\cos\theta_{\mathrm{OH}}|a)$ we can relate values of α to associated values of ϵ_{s}. This relationship thus allows us to assign a value of IH to a given surface based on atomistic simulation data.

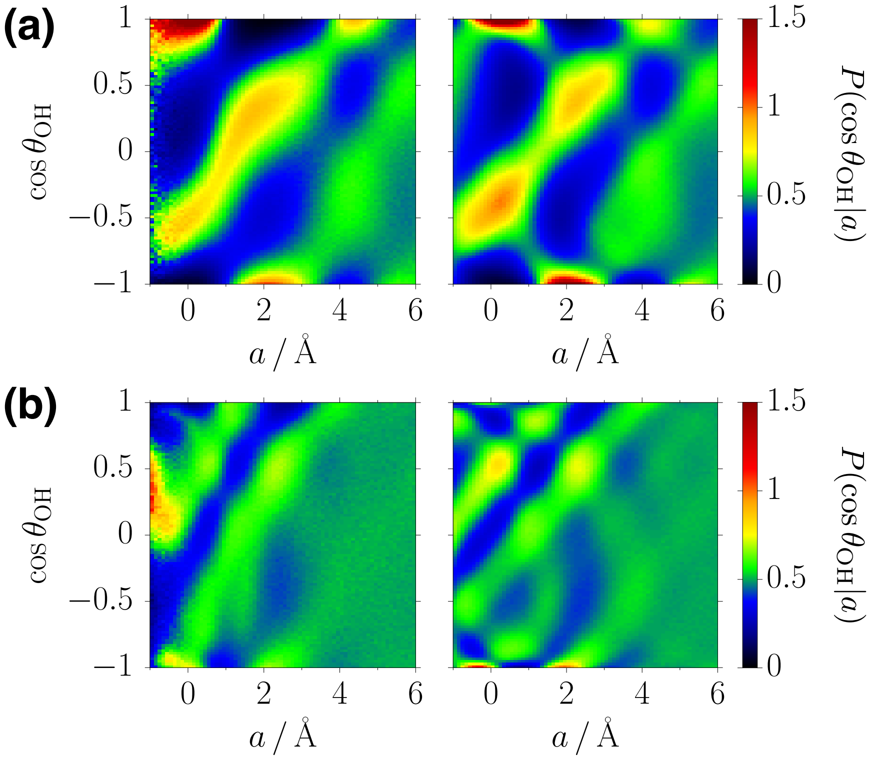

Figure 5.7 Plots of the reduced orientational distributions for a specific surface with different polarities, (a) $\alpha = 0$ and (b) $\alpha = 1$, where color shading indicates the value of probability density. Each panel compares the result from the MD simulation (left) to that from the mean-field model (right). Model parameters used for the above plots are $\epsilon_{\mathrm{s}}^{*} = 0\,k_B T$ and $\epsilon_{\mathrm{s}}^{*} = -1.55\,k_B T$ for $\alpha = 0$ and $\alpha = 1$, respectively.

To make a quantitative comparison between $P_{\mathrm{sim}}(\cos\theta_{\mathrm{OH}}|a)$ and $P_{\mathrm{MF}}(\cos\theta_{\mathrm{OH}}|a, \epsilon_{\mathrm{s}})$, where we now include the conditional dependence on ϵ_{s} for the mean field model, we compute a fitness function $\Gamma(\epsilon_{\mathrm{s}})$ based on the Kullback-Leibler divergence.[76] This fitness function is given by,

$$\Gamma(\epsilon_{\mathrm{s}}) = \int da \int d(\cos\theta_{\mathrm{OH}})\, P_{\mathrm{sim}}(\cos\theta_{\mathrm{OH}}|a) \ln\left[\frac{P_{\mathrm{sim}}(\cos\theta_{\mathrm{OH}}|a)}{P_{\mathrm{MF}}(\cos\theta_{\mathrm{OH}}|a, \epsilon_{\mathrm{s}})}\right], \tag{5.12}$$

which quantifies the similarity between the orientational molecular structure of a simulated system and that of our mean field model at a given value of ϵ_{s}. By minimizing $\Gamma(\epsilon_{\mathrm{s}})$ we can therefore identify the value of ϵ_{s} that most closely mimics the effective surface-water interactions of the simulated system. The value of ϵ_{s} that minimizes $\Gamma(\epsilon_{\mathrm{s}})$, denoted by $\epsilon_{\mathrm{s}}^{*}$, we thus take to represent the IH of the surface. Figure 5.7 shows a comparison between $P_{\mathrm{sim}}(\cos\theta_{\mathrm{OH}}|a)$ and $P_{\mathrm{MF}}(\cos\theta_{\mathrm{OH}}|a, \epsilon_{\mathrm{s}}^{*})$ for simulations with $\alpha = 0$ and $\alpha = 1$. This comparison reveals that our simple model is capable of capturing the sensitivity of interfacial molecular structure to changes in surface-water interactions.

In Fig. 5.8 we plot the dependence of $\epsilon_{\mathrm{s}}^{*}$ on α. For $\alpha < 0.4$ we observe that $\epsilon_{\mathrm{s}}^{*} \approx 0$, indicating that for these cases surface-water interactions exert a negligible influence

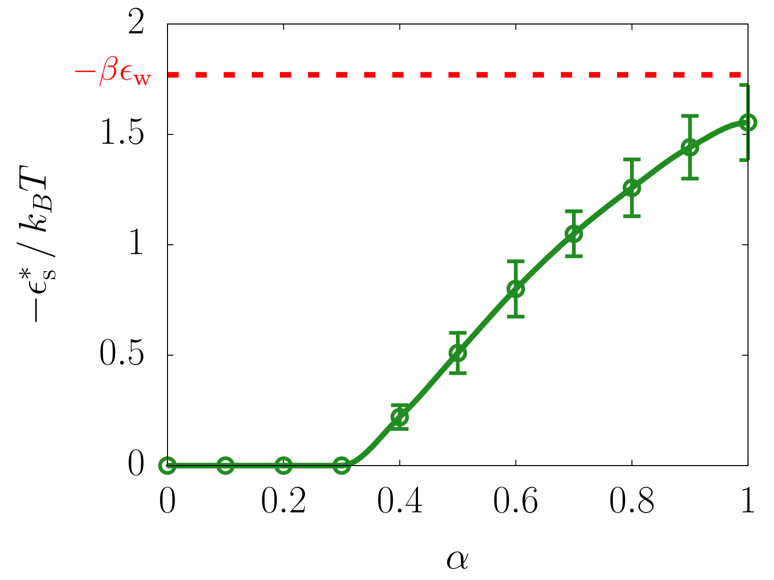

Figure 5.8 A plot of the optimized parameter for the effective surface-water interaction against the surface polarity shown with error bars, where the green solid line is a guide to the eye and the red dashed line indicates the optimal parameter for the interaction between the liquid water molecules, $\epsilon_w = -1.77\, k_B T$.

on the structure of water's interfacial hydrogen bonding network. For $\alpha \geq 0.4$, ϵ_s^* increases monotonically with α, reaching a value of nearly ϵ_w when $\alpha = 1$. The difference of ϵ_s^* from ϵ_w when $\alpha = 1$ may be surprising because the surface has a force field and structure that is identical to that of bulk liquid water. The difference between ϵ_s^* and ϵ_w arises because the surface is rigid, so the effective hydrogen bonding interactions between the surface and water lack the entropic stabilization associated with hydrogen bond network flexibility.

We observe that ϵ_s^* and $\langle \delta\lambda_{\text{phob}} \rangle$ exhibit a similar dependence on α, indicating the strong relationship between IH and variations in interfacial molecular structure. Notably, the behavior of ϵ_s^* reveals a clear threshold that is not apparent in $\langle U_{\text{w-s}} \rangle$, plotted in Fig. 5.2. Evidently, when α is small, changes in $\langle U_{\text{w-s}} \rangle$ with α do not contribute to changes in the structure of the interfacial hydrogen bonding network. Rather they contribute to changes in the spatial profile of the intrinsic water interface, such as the mean and variance of the interfacial heights. Thus, the properties that control aqueous interfacial solvation are determined by an interplay between the intrinsic properties of the interfacial liquid and the fluctuations in interfacial density that arise due to entropically-driven variations in the position of the intrinsic liquid interface.

By combining simulation tools for quantifying interfacial molecular structure with insight gained through a simple model of interfacial hydrogen bonding, we have highlighted that hydrophilic interfacial structure emerges through a competition between surface-water interactions and the collective water-water interactions of the bulk liquid. Using the mean field model, we evaluated the contribution of surface-water interactions to the emergence of hydrophilic interfacial structure in terms of the effective hydrogen bond energy, $\epsilon_{\mathrm{s}}^{*}$. This specific energetic component can be interpreted as a novel scale for the surface hydropathy; one that reports directly on the ability of the surface to modify water's preferred interfacial hydrogen bonding structure. With this measure, the influence of a hydrophilic surface on a water interface can be neatly separated into its structural and spatial (*e.g.* changes in capillary-wave behavior) components.

5.4.3 Density Profiles for Model Surfaces

As described in the main text, we computed the density profiles of the molecules in liquid and surface, namely $\rho_{\mathrm{w}}(a)$ and $\rho_{\mathrm{s}}^{(\mathrm{int})}(a)$, relative to the position of the intrinsic water interface, following the procedure described in Sec. 2.1. These density profiles change significantly as the surface polarity, α, increases from 0 to 1. As illustrated in Fig. 5.9, the density profile for the surface gets closer to that for the liquid water upon the increase in α, which indicates more adsorption of the solvent molecules to the surface of larger polarity. For the mean-field model, we use a Gaussian function as an effective surface density profile, which is fitted from the leading peak of $\rho_{\mathrm{s}}^{(\mathrm{int})}(a)$ (more specifically, the region of $a \geq \arg\max_a\{\rho_{\mathrm{s}}^{(\mathrm{int})}(a)\}$). The Gaussian-fitted density profile is parametrized as $\rho_{\mathrm{s}}(a)/\rho_{\mathrm{b}} = \rho_0 e^{-(a-a_{\mathrm{s}})^2/2\sigma_{\mathrm{s}}^2}$, where ρ_{b} is the bulk density of liquid water, such that the set of parameters, $(a_{\mathrm{s}}, \sigma_{\mathrm{s}}, \rho_0)$, well represents the mean characteristics of the first molecular layer of a given surface. Table 5.1 lists a set of parameters for a specific model surface of the polarity ranging from $\alpha = 0$ to 1. Note that the Gaussian mean and width, a_{s} and σ_{s}, show the trends of increasing along with α.

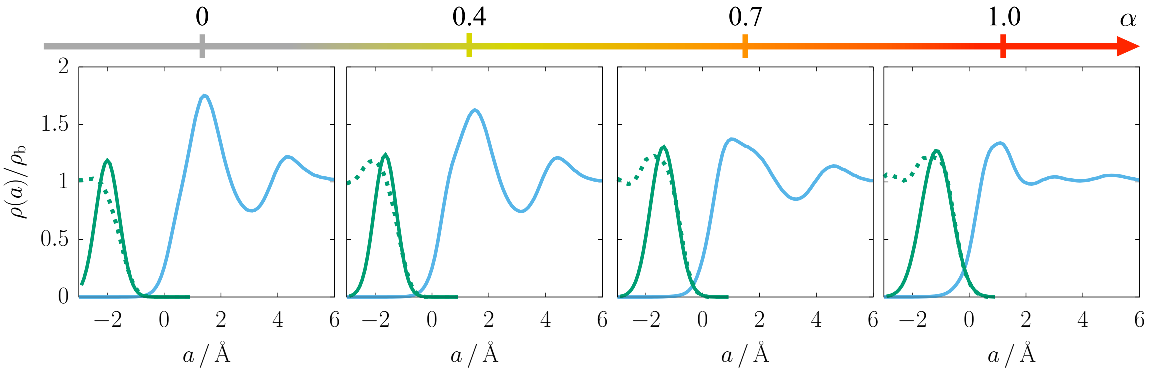

Figure 5.9 Plots of density profiles for different values of surface polarity. $\rho_{\mathrm{w}}(a)$ is rendered by blue line. $\rho_{\mathrm{s}}^{(\mathrm{int})}(a)$ and $\rho_{\mathrm{s}}(a)$ are rendered by green dotted and solid lines, respectively.

Table 5.1: Parameters for the Gaussian-fitted density profile, $\rho_{\mathrm{s}}(a)$, for a specific model surface with varied polarity.

α	a_{s} (Å)	σ_{s} (Å)	ρ_0
0	-1.99762	0.411275	1.18779
0.1	-2.07123	0.428661	1.47521
0.2	-1.94063	0.428272	1.2517
0.3	-1.82815	0.426502	1.2016
0.4	-1.64603	0.394326	1.23684
0.5	-1.56485	0.410636	1.28688
0.6	-1.52418	0.449296	1.36765
0.7	-1.38108	0.458931	1.30655
0.8	-1.34561	0.508773	1.33211
0.9	-1.24132	0.527848	1.282
1	-1.14727	0.539936	1.27362

Bibliography

[1] Phillip Ball. *Life's Matrix: A Biography of Water.* University of California Press, 2001.

[2] Kenneth B Eisenthal. Equilibrium and Dynamic Processes at Interfaces by Second Harmonic and Sum Frequency Generation. *Annual Review of Physical Chemistry*, 43(1):627–661, 1992.

[3] J Israelachvili and H Wennerström. Role of hydration and water structure in biological and colloidal interactions. *Nature*, 379(6562):219–225, 1996.

[4] Phillip L. Geissler, Christoph Dellago, and David Chandler. Kinetic Pathways of Ion Pair Dissociation in Water. *The Journal of Physical Chemistry B*, 103 (18):3706–3710, 1999.

[5] M. Tarek and D. J. Tobias. Role of Protein-Water Hydrogen Bond Dynamics in the Protein Dynamical Transition. *Physical Review Letters*, 88(13):138101, 2002.

[6] Pavel Jungwirth, Barbara J. Finlayson-Pitts, and Douglas J. Tobias. Introduction: Structure and Chemistry at Aqueous Interfaces. *Chemical Reviews*, 106 (4):1137–1139, 2006.

[7] Yaakov Levy and José N. Onuchic. Water Mediation in Protein Folding and Molecular Recognition. *Annual Review of Biophysics and Biomolecular Structure*, 35(1):389–415, 2006.

[8] Mary Griffin Krone, Lan Hua, Patricia Soto, Ruhong Zhou, B. J. Berne, and Joan-Emma Shea. Role of Water in Mediating the Assembly of Alzheimer Amyloid-β Aβ16$-$22 Protofilaments. *Journal of the American Chemical Society*, 130(33):11066–11072, 2008.

[9] Adam P Willard and David Chandler. The role of solvent fluctuations in hydrophobic assembly. *The Journal of Physical Chemistry B*, 112(19):6187–6192, 2008.

[10] Bhushan N Zope, David D Hibbitts, Matthew Neurock, and Robert J Davis. Reactivity of the Gold/Water Interface During Selective Oxidation Catalysis. *Science*, 330(6000):74–78, 2010.

[11] Mazen Ahmad, Wei Gu, Tihamér Geyer, and Volkhard Helms. Adhesive water networks facilitate binding of protein interfaces. *Nature Communications*, 2: 261, 2011.

[12] Vasudevan Venkateshwaran, Srivathsan Vembanur, and Shekhar Garde. Water-mediated ion-ion interactions are enhanced at the water vapor-liquid interface. *Proceedings of the National Academy of Sciences of the United States of America*, 111(24):8729–34, 2014.

[13] Olle Björneholm, Martin H. Hansen, Andrew Hodgson, Li Min Liu, David T. Limmer, Angelos Michaelides, Philipp Pedevilla, Jan Rossmeisl, Huaze Shen, Gabriele Tocci, Eric Tyrode, Marie Madeleine Walz, Josephina Werner, and Hendrik Bluhm. Water at Interfaces. *Chemical Reviews*, 116(13):7698–7726, 2016.

[14] David Eisenberg and Walter Kauzmann. *The Structure and Properties of Water*. Clarendon Press, Oxford, 2005.

[15] Felix Franks. *Water: A Matrix of Life*. Royal Society of Chemistry, Cambridge, UK, 2nd ed. edition, 2000.

[16] Shelley L. Shostak, William L. Ebenstein, and J. S. Muenter. The dipole moment of water. I. Dipole moments and hyperfine properties of H2O and HDO in the ground and excited vibrational states. *The Journal of Chemical Physics*, 94(9):5875–5882, 1991.

[17] Alex Shank, Yimin Wang, Alexey Kaledin, Bastiaan J. Braams, and Joel M. Bowman. Accurate ab initio and "hybrid" potential energy surfaces, intramolecular vibrational energies, and classical ir spectrum of the water dimer. *Journal of Chemical Physics*, 130(14):144314, 2009.

[18] W. F. Giauque and J. O. Clayton. The Heat Capacity and Entropy of Nitrogen. Heat of Vaporization. Vapor Pressures of Solid and Liquid. The Reaction 1/2 N_2+ 1/2 O_2 = NO from Spectroscopic Data. *Journal of the American Chemical Society*, 55(12):4875–4889, 1933.

[19] A. H. Narten and H. A. Levy. Liquid Water: Molecular Correlation Functions from X-Ray Diffraction. *The Journal of Chemical Physics*, 55(5):2263–2269, 1971.

[20] A. H. Narten, C. G. Venkatesh, and S. A. Rice. Diffraction Pattern and Structure of Amorphous Solid Water at 10 and 77 °K. *The Journal of Chemical Physics*, 64(3):1106–1121, 1976.

[21] David Chandler. From Fifty Years Ago, the Birth of Modern Liquid-state Science. *Annual Review of Physical Chemistry*, 68:19–38, 2017.

[22] J Errington and P Debenedetti. Relationship between structural order and the anomalies of liquid water. *Nature*, 409(6818):318–321, 2001.

[23] Damien Laage and James T Hynes. A Molecular Jump Mechanism of Water Reorientation. *Science*, 311(5762):832–835, 2006.

[24] J. L. Abascal and C. Vega. A General Purpose Model for the Condensed Phases of Water: TIP4P/2005. *The Journal of Chemical Physics*, 123(23):234505, 2005.

[25] Pavel Jungwirth and Douglas J Tobias. Specific Ion Effects at the Air/Water Interface. *Chemical Reviews*, 106:1259–1281, 2006.

[26] Douglas J Tobias, Abraham C Stern, Marcel D Baer, Yan Levin, and Christopher J Mundy. Simulation and theory of ions at atmospherically relevant aqueous liquid-air interfaces. *Annual Review of Physical Chemistry*, 64:339–59, 2013.

[27] K. B. Eisenthal. Liquid Interfaces Probed by Second-Harmonic and Sum-Frequency Spectroscopy. *Chemical Reviews*, 96(4):1343–1360, 1996.

[28] A. Verdaguer, G. M. Sacha, H. Bluhm, and M. Salmeron. Molecular Structure of Water at Interfaces: Wetting at the Nanometer Scale. *Chemical Reviews*, 106(4):1478–1510, 2006.

[29] Frank H Stillinger. Water Revisited. *Science*, 209(4455):451–457, 1980.

[30] Teresa Head-Gordon and Frank H Stillinger. An orientational perturbation theory for pure liquid water. *The Journal of Chemical Physics*, 98(4):3313–3327, 1993.

[31] A. K. Soper. Orientational correlation function for molecular liquids: The case of liquid water. *The Journal of Chemical Physics*, 101(8):6888–6901, 1994.

[32] T Lazaridis and M Karplus. Orientational correlations and entropy in liquid water. *The Journal of Chemical Physics*, 105(2):4294–4316, 1996.

[33] Flaviu S. Cipcigan, Vlad P. Sokhan, Andrew P. Jones, Jason Crain, and Glenn J. Martyna. Hydrogen bonding and molecular orientation at the liquid–vapour interface of water. *Physical Chemistry Chemical Physics*, 17(14):8660–8669, 2015.

[34] Adam P Willard and David Chandler. Instantaneous liquid interfaces. *Journal of Physical Chemistry B*, 114(5):1954–1958, 2010.

[35] H J C Berendsen, J R Grigera, and T P Straatsma. The Missing Term in Effective Pair Potentials. *Journal of Physical Chemistry*, 91(24):6269–6271, 1987.

[36] Michael W. Mahoney and William L. Jorgensen. A five-site model for liquid water and the reproduction of the density anomaly by rigid, nonpolarizable potential functions. *Journal of Chemical Physics*, 112:8910, 2000.

[37] Steve Plimpton. Fast Parallel Algorithms for Short-Range Molecular Dynamics. *Journal of Computational Physics*, 117(1):1–19, 1995.

[38] Sander Pronk, Szilárd Páll, Roland Schulz, Per Larsson, Pär Bjelkmar, Rossen Apostolov, Michael R. Shirts, Jeremy C. Smith, Peter M. Kasson, David Van Der Spoel, Berk Hess, and Erik Lindahl. GROMACS 4.5: A high-throughput and highly parallel open source molecular simulation toolkit. *Bioinformatics*, 29(7):845–854, 2013.

[39] Jan Kessler, Hossam Elgabarty, Thomas Spura, Kristof Karhan, Pouya Partovi-Azar, Ali A Hassanali, and Thomas D Kuhne. Structure and Dynamics of the Instantaneous Water/Vapor Interface Revisited by Path-Integral and Ab-Initio Molecular Dynamics Simulations. *The Journal of Physical Chemistry. B*, 119 (31):10079–10086, 2015.

[40] Richard J. Saykally. Air/water interface: Two sides of the acid–base story. *Nature Chemistry*, 5(2):82–84, 2013.

[41] Robert Vácha, Ondrej Marsalek, Adam P Willard, Douwe Jan Bonthuis, Roland R Netz, and Pavel Jungwirth. Charge Transfer between Water Molecules As the Possible Origin of the Observed Charging at the Surface of Pure Water. *Journal of Physical Chemistry Letters*, 3(1):107–111, 2012.

[42] Katarzyna Ciunel, Marc Armélin, Gerhard H. Findenegg, and Regine Von Klitzing. Evidence of surface charge at the air/water interface from thin-film studies on polyelectrolyte-coated substrates. *Langmuir*, 21(11):4790–4793, 2005.

[43] Otto Stern. Zur theorie der elektrolytischen doppelschicht. *Zeitschrift für Elektrochemie und angewandte physikalische Chemie*, 30:508–516, 1924.

[44] Sanjib Senapati and Amalendu Chandra. Dielectric constant of water confined in a nanocavity. *Journal of Physical Chemistry B*, 105(22):5106–5109, 2001.

[45] O. Teschke, G. Ceotto, and E. F. de Souza. Interfacial water dielectric-permittivity-profile measurements using atomic force microscopy. *Physical Review E*, 64(1):011605, 2001.

[46] Alexander Schlaich, Ernst W. Knapp, and Roland R. Netz. Water Dielectric Effects in Planar Confinement. *Physical Review Letters*, 117(4):048001, 2016.

[47] P. G. de Gennes. Wetting: statics and dynamics. *Reviews of Modern Physics*, 57(3):827–863, 1985.

[48] Rahul Godawat, Sumanth N Jamadagni, and Shekhar Garde. Characterizing hydrophobicity of interfaces by using cavity formation, solute binding, and water correlations. *Proceedings of the National Academy of Sciences*, 106(36): 15119–15124, 2009.

[49] Sumanth N Jamadagni, Rahul Godawat, and Shekhar Garde. Hydrophobicity of proteins and interfaces: insights from density fluctuations. *Annual Review of Chemical and Biomolecular Engineering*, 2:147–171, 2011.

[50] Amish J. Patel and Shekhar Garde. Efficient method to characterize the context-dependent hydrophobicity of proteins. *Journal of Physical Chemistry B*, 118(6):1564–1573, 2014.

[51] Adam P Willard and David Chandler. The molecular structure of the interface between water and a hydrophobic substrate is liquid-vapor like. *The Journal of Chemical Physics*, 141(18):18C519, 2014.

[52] John G. Kirkwood. The Dielectric Polarization of Polar Liquids. *The Journal of Chemical Physics*, 7(10):911–919, 1939.

[53] Herbert Fröhlich. *Theory of dielectrics: dielectric constant and dielectric loss*. Clarendon Press, 1958.

[54] Philippe A. Bopp, Alexei A. Kornyshev, and Godehard Sutmann. Static Nonlocal Dielectric Function of Liquid Water. *Physical Review Letters*, 76(8):1280–1283, 1996.

[55] Florin Despa, Ariel Fernández, and R. Stephen Berry. Dielectric Modulation of Biological Water. *Physical Review Letters*, 93(22):228104, 2004.

[56] Douwe Jan Bonthuis, Stephan Gekle, and Roland R. Netz. Dielectric Profile of Interfacial Water and its Effect on Double-Layer Capacitance. *Physical Review Letters*, 107(16):166102, 2011.

[57] Yan Levin, Alexandre P. dos Santos, and Alexandre Diehl. Ions at the Air-Water Interface: An End to a Hundred-Year-Old Mystery? *Physical Review Letters*, 103(25):257802, 2009.

[58] Lei Zhao and Zhiqun Lin. Self-assembly of non-linear polymers at the air/water interface: the effect of molecular architecture. *Soft Matter*, 7(22):10520, 2011.

[59] N Ji, V Ostroverkhov, C S Tian, and Y R Shen. Characterization of Vibrational Resonances of Water-Vapor Interfaces by Phase-Sensitive Sum-Frequency Spectroscopy. *Physical Review Letters*, 100(9):096102, 2008.

[60] Yuen Ron Shen and Victor Ostroverkhov. Sum-Frequency Vibrational Spectroscopy on Water Interfaces: Polar Orientation of Water Molecules at Interfaces. *Chemical Reviews*, 106(4):1140–1154, 2006.

[61] E A Raymond, T L Tarbuck, and G L Richmond. Isotopic Dilution Studies of the Vapor/Water Interface as Investigated by Vibrational Sum-Frequency Spectroscopy. *The Journal of Physical Chemistry B*, 106(11):2817–2820, 2002.

[62] Elizabeth A Raymond, Teresa L Tarbuck, Mac G Brown, and Geraldine L Richmond. Hydrogen-Bonding Interactions at the Vapor/Water Interface Investigated by Vibrational Sum-Frequency Spectroscopy of HOD/H_2O/D_2O Mixtures and Molecular Dynamics Simulations. *The Journal of Physical Chemistry B*, 107(2):546–556, 2003.

[63] Michael A Wilson, Andrew Pohorille, and Lawrence R. Pratt. Molecular dynamics of the water liquid-vapor interface. *Journal of Physical Chemistry*, 91: 4873–4878, 1987.

[64] Mitsuhiro Matsumoto and Yosuke Kataoka. Study on liquid–vapor interface of water. I. Simulational results of thermodynamic properties and orientational structure Study on liquid-vapor interface of water. I. Simulational results of thermodynamic properties and orientational structure. *J. Chem. Phys*, 88(5): 3233–3245, 1988.

[65] Yubo Fan, Xin Chen, Lijiang Yang, Paul Cremer, and Yi Qin Gao. On the Structure of Water at the Aqueous / Air Interface. *Journal of Physical Chemistry B*, 113(34):11672–11679, 2009.

[66] Piotr A. Pieniazek, Craig J. Tainter, and James L. Skinner. Surface of Liquid Water: Three-Body Interactions and Vibrational Sum-Frequency Spectroscopy. *Journal of the American Chemical Society*, 133(27):10360–10363, 2011.

[67] Satoshi Nihonyanagi, Tatsuya Ishiyama, Touk-kwan Lee, Shoichi Yamaguchi, Mischa Bonn, Akihiro Morita, and Tahei Tahara. Unified Molecular View of the Air/Water Interface Based on Experimental and Theoretical $\chi^{(2)}$ Spectra of an Isotopically Diluted Water Surface. *Journal of the American Chemical Society*, 133(42):16875–16880, 2011.

[68] Ahmed E. Ismail, Gary S. Grest, and Mark J. Stevens. Capillary waves at the liquid-vapor interface and the surface tension of water. *The Journal of Chemical Physics*, 125(1):014702, 2006.

[69] Felix Sedlmeier, Dominik Horinek, and Roland R. Netz. Nanoroughness, Intrinsic Density Profile, and Rigidity of the Air-Water Interface. *Physical Review Letters*, 103(13):136102, 2009.

[70] F. P. Buff, R. A. Lovett, and F. H. Stillinger. Interfacial Density Profile for Fluids in the Critical Region. *Physical Review Letters*, 15(15):621–623, 1965.

[71] K R Mecke and S Dietrich. Effective Hamiltonian for liquid-vapor interfaces. *Physical Review E*, 59(6):6766–6784, 1999.

[72] J. S. Rowlinson and B. Widom. *Molecular Theory of Capillarity*. Courier Corporation, 2002.

[73] A. J. Patel, P. Varilly, S. N. Jamadagni, H. Acharya, S. Garde, and D. Chandler. Extended surfaces modulate hydrophobic interactions of neighboring solutes. *Proceedings of the National Academy of Sciences*, 108(43):17678–17683, 2011.

[74] Jessica Hughes, Eric J. Krebs, and David Roundy. A classical density-functional theory for describing water interfaces. *The Journal of Chemical Physics*, 138 (2):024509, 2013.

[75] William L. Jorgensen, Jayaraman Chandrasekhar, Jeffry D. Madura, Roger W. Impey, and Michael L. Klein. Comparison of simple potential functions for simulating liquid water. *The Journal of Chemical Physics*, 79(2):926, 1983.

[76] S. Kullback and R. A. Leibler. On Information and Sufficiency. *The Annals of Mathematical Statistics*, 22(1):79–86, 1951.

[77] S. J. Suresh and V. M. Naik. Hydrogen bond thermodynamic properties of water from dielectric constant data. *The Journal of Chemical Physics*, 113(21): 9727, 2000.

[78] Jared D Smith, Christopher D Cappa, Kevin R Wilson, Benjamin M Messer, Ronald C Cohen, and Richard J Saykally. Energetics of hydrogen bond network rearrangements in liquid water. *Science*, 306(5697):851–3, 2004.

[79] Jared D Smith, Christopher D Cappa, Kevin R Wilson, Ronald C Cohen, Phillip L Geissler, and Richard J Saykally. Unified description of temperature-dependent hydrogen-bond rearrangements in liquid water. *Proceedings of the National Academy of Sciences*, 102(40):14171–14174, 2005.

[80] Phillip L Geissler. Water Interfaces, Solvation, and Spectroscopy. *Annual Review of Physical Chemistry*, 64(1):317–337, 2013.

[81] Frank H. Stillinger. Structure in Aqueous Solutions of Nonpolar Molecules from the Standpoint of Scaled-Particle Theory. *Journal of Solution Chemistry*, 2:141, 1973.

[82] Sotiris S Xantheas. Cooperativity and hydrogen bonding network in water clusters. *Chemical Physics*, 258(2-3):225–231, 2000.

[83] R Kumar and J L Skinner. Water Simulation Model with Explicit Three-Molecule Interactions. *The Journal of Physical Chemistry B*, 112(28):8311–8318, 2008.

[84] Gregory R Medders and Francesco Paesani. Dissecting the Molecular Structure of the Air/Water Interface from Quantum Simulations of the Sum-Frequency Generation Spectrum. *Journal of the American Chemical Society*, 138(11): 3912–3919, 2016.

[85] Frank N. Keutsch, Jeffery D. Cruzan, and Richard J. Saykally. The water trimer. *Chemical Reviews*, 103(7):2533–2577, 2003.

[86] Alenka Luzar and David Chandler. Effect of Environment on Hydrogen Bond Dynamics in Liquid Water. *Physical Review Letters*, 76(6):928–931, 1996.

[87] Richard C Remsing, Marcel D Baer, Gregory K Schenter, Christopher J Mundy, and John D Weeks. The Role of Broken Symmetry in Solvation of a Spherical Cavity in Classical and Quantum Water Models. *The Journal of Physical Chemistry Letters*, 5(16):2767–2774, 2014.

[88] David Quéré. Wetting and Roughness. *Annual Review of Materials Research*, 38(1):71–99, 2008.

[89] Q. Du, R. Superfine, E. Freysz, and Y. R. Shen. Vibrational spectroscopy of water at the vapor/water interface. *Physical Review Letters*, 70(15):2313–2316, 1993.

[90] Michael Schleeger, Yuki Nagata, and Mischa Bonn. Quantifying surfactant alkyl chain orientation and conformational order from sum frequency generation spectra of CH modes at the surfactant-water interface. *Journal of Physical Chemistry Letters*, 5(21):3737–3741, 2014.

[91] Prashant Chandra Singh, Satoshi Nihonyanagi, Shoichi Yamaguchi, and Tahei Tahara. Ultrafast vibrational dynamics of water at a charged interface revealed by two-dimensional heterodyne-detected vibrational sum frequency generation. *Journal of Chemical Physics*, 137(9):094706, 2012.

[92] Mary Jane Shultz, Steve Baldelli, Cheryl Schnitzer, and Danielle Simonelli. Aqueous solution/air interfaces probed with sum frequency generation spectroscopy. *Journal of Physical Chemistry B*, 106(21):5313–5324, 2002.

[93] D. E. Gragson, B. M. McCarty, and G. L. Richmond. Ordering of interfacial water molecules at the charged air/water interface observed by vibrational sum frequency generation. *Journal of the American Chemical Society*, 119(26):6144–6152, 1997.

[94] Valeria Conti Nibali and Martina Havenith. New insights into the role of water in biological function: Terahertz absorption spectroscopy and molecular dynamics simulations studies of the solvation dynamics of biomolecules. *Journal of the American Chemical Society*, 136:12800–12807, 2014.

[95] Simon Ebbinghaus, Seung Joong Kim, Matthias Heyden, Xin Yu, Udo Heugen, Martin Gruebele, David M Leitner, and Martina Havenith. An extended dynamical hydration shell around proteins. *Proceedings of the National Academy of Sciences of the United States of America*, 104(52):20749–20752, 2007.

[96] B. D. Armstrong and S. Han. Overhauser dynamic nuclear polarization to study local water dynamics. *Journal of the American Chemical Society*, 131 (13):4641–4647, 2009.

[97] Gottfried Otting and Kurt Wüthrich. Studies of Protein Hydration in Aqueous Solution by Direct NMR Observation of Individual Protein-Bound Water Molecules. *Journal of the American Chemical Society*, 111(5):1871–1875, 1989.

[98] G Otting, E Liepinsh, and K Wuthrich. Protein hydration in aqueous solution. *Science*, 254(5034):974–980, 1991.

[99] D I Svergun, S Richard, M H Koch, Z Sayers, S Kuprin, and G Zaccai. Protein hydration in solution: Experimental observation by x-ray and neutron scattering. *Proceedings of the National Academy of Sciences of the United States of America*, 95(5):2267–2272, 1998.

[100] Fabio Bruni, Maria Antonietta Ricci, and Alan K. Soper. Water confined in Vycor glass. I. a neutron diffraction study. *Journal of Chemical Physics*, 109 (4):1478–1485, 1998.

[101] Guangming Luo, Sarka Malkova, Jaesung Yoon, David G. Schultz, Binhua Lin, Mati Meron, Ilan Benjamin, Petr Vanýsek, and Mark L. Schlossman. Ion Distributions near a Liquid-Liquid Interface. *Science*, 311(5758):216–218, 2006.

[102] J Kyte and R F Doolittle. A simple method for displaying the hydropathic character of a protein. *Journal of Molecular Biology*, 157(1):105–132, 1982.

[103] Lauren H. Kapcha and Peter J. Rossky. A simple atomic-level hydrophobicity scale reveals protein interfacial structure. *Journal of Molecular Biology*, 426(2): 484–498, 2014.

[104] David T. Limmer and Adam P. Willard. Nanoscale heterogeneity at the aqueous electrolyte–electrode interface. *Chemical Physics Letters*, 620:144–150, 2015.

[105] Amish J. Patel, Patrick Varilly, David Chandler, and Shekhar Garde. Quantifying Density Fluctuations in Volumes of All Shapes and Sizes Using Indirect Umbrella Sampling. *Journal of Statistical Physics*, 145(2):265–275, 2011.

[106] Tom Young, Robert Abel, Byungchan Kim, Bruce J. Berne, and Richard A. Friesner. Motifs for molecular recognition exploiting hydrophobic enclosure in protein–ligand binding. *Proceedings of the National Academy of Sciences*, 104 (3):808–813, 2007.

[107] Richard C Remsing and John D Weeks. Hydrophobicity Scaling of Aqueous Interfaces by an Electrostatic Mapping. *Journal of Physical Chemistry B*, 119 (29):9268–9277, 2015.

[108] Nicolas Giovambattista, Pablo G. Debenedetti, and Peter J. Rossky. Hydration behavior under confinement by nanoscale surfaces with patterned hydrophobicity and hydrophilicity. *Journal of Physical Chemistry C*, 111(3):1323–1332, 2007.

[109] Miljan Simonovic and Karl Volz. A Distinct Meta-active Conformation in the 1.1-Å Resolution Structure of Wild-type ApoCheY. *Journal of Biological Chemistry*, 276(31):28637–28640, 2001.

[110] William Humphrey, Andrew Dalke, and Klaus Schulten. VMD: Visual molecular dynamics. *Journal of Molecular Graphics*, 14(1):33–38, 1996.

[111] A. D. MacKerell, D. Bashford, M. Bellott, R. L. Dunbrack, J. D. Evanseck, M. J. Field, S. Fischer, J. Gao, H. Guo, S. Ha, D. Joseph-McCarthy, L. Kuchnir, K. Kuczera, F. T. K. Lau, C. Mattos, S. Michnick, T. Ngo, D. T. Nguyen, B. Prodhom, W. E. Reiher, B. Roux, M. Schlenkrich, J. C. Smith, R. Stote, J. Straub, M. Watanabe, J. Wiórkiewicz-Kuczera, D. Yin, and M. Karplus. All-Atom Empirical Potential for Molecular Modeling and Dynamics Studies of Proteins. *The Journal of Physical Chemistry B*, 102(18):3586–3616, 1998.

[112] Ilan Benjamin. Chemical Reactions and Solvation at Liquid Interfaces : A Microscopic Perspective. *Chemical Reviews*, 96(4):1449–1476, 1996.

[113] Zhenbin Ge, David G. Cahill, and Paul V. Braun. Thermal conductance of hydrophilic and hydrophobic interfaces. *Physical Review Letters*, 96(18):1–4, 2006.

[114] Michael R. Brindza and Robert A. Walker. Differentiating solvation mechanisms at polar solid/liquid interfaces. *Journal of the American Chemical Society*, 131 (17):6207–6214, 2009.

[115] Pierre Adrien Mante, Chien Cheng Chen, Yu Chieh Wen, Hui Yuan Chen, Szu Chi Yang, Yu Ru Huang, I. J. Chen, Yun Wen Chen, Vitalyi Gusev, Miin Jang Chen, Jer Lai Kuo, Jinn Kong Sheu, and Chi Kuang Sun. Probing hydrophilic interface of solid/liquid-water by nanoultrasonics. *Scientific Reports*, 4(1):6249, 2014.

[116] Yu-Chieh Wen, Shuai Zha, Xing Liu, Shanshan Yang, Pan Guo, Guosheng Shi, Haiping Fang, Y Ron Shen, and Chuanshan Tian. Unveiling Microscopic Structures of Charged Water Interfaces by Surface-Specific Vibrational Spectroscopy. *Physical Review Letters*, 116(1):016101, 2016.

[117] Sucheol Shin and Adam P. Willard. Three-Body Hydrogen Bond Defects Contribute Significantly to the Dielectric Properties of the Liquid Water-Vapor Interface. *Journal of Physical Chemistry Letters*, 9(7):1649–1654, 2018.

[118] J D Eaves, J J Loparo, C J Fecko, S T Roberts, A Tokmakoff, and P L Geissler. Hydrogen bonds in liquid water are broken only fleetingly. *Proceedings of the National Academy of Sciences of the United States of America*, 102(37):13019–13022, 2005.

[119] J. Turner and A. K. Soper. The effect of apolar solutes on water structure: Alcohols and tetraalkylammonium ions. *The Journal of Chemical Physics*, 101 (7):6116–6125, 1994.

[120] Francesco Vanzi, Bhupinder Madan, and Kim Sharp. Effect of the protein denaturants urea and guanidinium on water structure: A structural and thermodynamic study. *Journal of the American Chemical Society*, 120(41):10748–10753, 1998.

[121] P. L. Geissler, Christoph Dellago, David Chandler, Jurg Hutter, and Michele Parrinello. Autoionization in Liquid Water. *Science*, 291(5511):2121–2124, 2001.

[122] John A. Kattirtzi, David T. Limmer, and Adam P. Willard. Microscopic dynamics of charge separation at the aqueous electrochemical interface. *Proceedings of the National Academy of Sciences*, 114(51):13374–13379, 2017.

[123] M. J. Shultz, C. Schnitzer, D. Simonelli, and S. Baldelli. Sum frequency generation spectroscopy of the aqueous interface: Ionic and soluble molecular solutions. *International Reviews in Physical Chemistry*, 19(1):123–153, 2000.

[124] G. L. Richmond. Molecular bonding and interactions at aqueous surfaces as probed by vibrational sum frequency spectroscopy. *Chemical Reviews*, 102(8): 2693–2724, 2002.

[125] M Heyden, E Brundermann, U Heugen, G Niehues, D M Leitner, and M Havenith. Long-range influence of carbohydrates on the solvation dynamics of water-answers from terahertz absorption measurements and molecular modeling simulations. *Journal of the American Chemical Society*, 130(17):5773–5779, 2008.

[126] Evan R McCarney, Brandon D Armstrong, Ravinath Kausik, and Songi Han. Dynamic nuclear polarization enhanced nuclear magnetic resonance and electron spin resonance studies of hydration and local water dynamics in micelle and vesicle assemblies. *Langmuir*, 24(18):10062–10072, 2008.

[127] U Heugen, G Schwaab, E Bründermann, M Heyden, X Yu, D M Leitner, M Havenith, U Heugen, G Schwaab, E Bru, E Bründermann, M Heyden, X Yu, D M Leitner, and M Havenith. Solute-induced retardation of water dynamics probed directly by terahertz spectroscopy. *Proceedings of the National Academy of Sciences of the United States of America*, 103(33):12301–6, 2006.

[128] Brandon D. Armstrong, Jennifer Choi, Carlos López, Darryl A. Wesener, Wayne Hubbell, Silvia Cavagnero, and Songi Han. Site-specific hydration dynamics in the nonpolar core of a molten globule by dynamic nuclear polarization of water. *Journal of the American Chemical Society*, 133(15):5987–5995, 2011.

[129] Matthias Heyden, Jian Sun, Stefan Funkner, Gerald Mathias, Harald Forbert, Martina Havenith, and Dominik Marx. Dissecting the THz spectrum of liquid water from first principles via correlations in time and space. *Proceedings of the National Academy of Sciences of the United States of America*, 107(27): 12068–12073, 2010.

[130] Marie-Pierre Gaigeot, Michiel Sprik, and Marialore Sulpizi. Oxide/water interfaces: how the surface chemistry modifies interfacial water properties. *Journal of Physics: Condensed Matter*, 24(12):124106, 2012.

[131] Nicolas Giovambattista, Pablo G. Debenedetti, and Peter J. Rossky. Effect of surface polarity on water contact angle and interfacial hydration structure. *Journal of Physical Chemistry B*, 111(32):9581–9587, 2007.

[132] Siewert J. Marrink, H. Jelger Risselada, Serge Yefimov, D. Peter Tieleman, and Alex H. De Vries. The MARTINI force field: Coarse grained model for biomolecular simulations. *Journal of Physical Chemistry B*, 111(27):7812–7824, 2007.

[133] Amish J. Patel, Patrick Varilly, and David Chandler. Fluctuations of water near extended hydrophobic and hydrophilic surfaces. *Journal of Physical Chemistry B*, 114(4):1632–1637, 2010.

[134] Sucheol Shin and Adam P. Willard. Characterizing Hydration Properties Based on the Orientational Structure of Interfacial Water Molecules. *Journal of Chemical Theory and Computation*, 14(2):461–465, 2018.

[135] David Chandler. Interfaces and the driving force of hydrophobic assembly. *Nature*, 437(7059):640–647, 2005.